Pulling Through:
A Biomechanical Analysis of Normal and Aberrant Embryogenesis in *Drosophila*

By

Winston Tyler McCleery

Dissertation

Submitted to the Faculty of the

Graduate School of Vanderbilt University

in partial fulfillment of the requirements

for the degree of

DOCTOR OF PHILOSOPHY

in

Physics

May 2016

Nashville, Tennessee

Approved:

M. Shane Hutson, Ph.D.

Kirill Bolotin, Ph.D.

Andrea Page-McCaw, Ph.D.

Erin Rericha, Ph.D.

John P. Wikswo, Ph.D.

To my grandfather, Tarldon Neese

who captivated my imagination with bugs and a microscope

Deo gratias!

ACKNOWLEDGEMENTS

This work would not have been possible without the financial support of the National Science Foundation Graduate Research Fellowship Program, and the National Institutes of Health. I would like to thank the fly community for the sharing of resources. I am especially grateful for the mentoring of my Ph.D. advisor, Dr. Shane Hutson, who was kind enough to reply to a prospective student's e-mail and to continue with guidance in research and teaching throughout my graduate career.

I am grateful to all of those with whom I have had the pleasure to work during these projects. Each of my Dissertation Committee members has provided me advice in my research endeavors and professional goals. My colleagues in the Hutson lab have also been a great source of support and inspiration as we have worked together through countless hours and challenges in the lab. I am especially grateful to Dr. Sarah Crews and soon-to-be Dr. Monica Lacy for their collaboration and comradery. I also appreciate the effort and encouragement of our collaborators from the University of Waterloo, Dr. Wayne Brodland and Dr. Jim Veldhuis.

No one has been more important to me in my academic studies than the members of my family. I would like to thank my parents, who have always encouraged me to study hard and pursue my dreams. Although I do not say it as often as I should, I am also very grateful to my grandmothers who have inspired me in so many ways beyond academics. Most importantly, I wish to thank my loving and encouraging wife, Rachel, for all of the selfless support she has given me in my pursuit of science.

TABLE OF CONTENTS

Page

DEDICATION……iii

ACKNOWLEDGEMENTS……iv

LIST OF TABLES……...viii

LIST OF FIGURES……ix

Chapter

1. WHAT CAN BE LEARNED BY STUDYING BIOMECHANICS IN THE FLY EMBRYO? …… 1

1.1 Pushing the Field of Soft Matter Physics……..1

1.2 Mechanical Analysis Improving Biological Understanding……2

1.3 Cellular Biomechanical Studies beyond Physics and Biology…… 2

1.4 Why *Drosophila*? ……3

1.5 Overview……...5

2. MODELING EMBRYOGENESIS…… 7

2.1 "Active" versus "Passive" Roles for Cells in Ventral Furrow Invagination…….8

2.2 Mechanical Robustness in Dorsal Closure……..12

2.3 Small Cell-Level Changes Produce Embryo-Wide Deformations in Germband Extension……15

2.4 Mechanical Coupling in Ventral Furrow Invagination……... 18

3. SELECTING A MODEL FOR GERMBAND RETRACTION……... 21

3.1 Four Modeling Formalisms for Embryogenesis…… 24

3.1.1 Geometric Rate Equation Models……24

3.1.2 Deformation Gradient Decomposition Models……26

3.1.3 Cellular Potts Models…….. 29

3.1.4 Vertex Models…… 31

3.2 Important Aspects of Germband Retraction to be Captured in the Model……. 34

3.3 A Modeling Formalism for Germband Retraction…… 36

3.3.1 Building a 2.5-Dimensional Model of Epithelial Dynamics……... 38

3.3.2 Constructing the Initial Mesh…….. 39

3.3.3 Exploring Germband Retraction with the Model…… 41

4. CELL GEOMETRY PROVIDES MECHANICAL ROBUSTNESS: A 2.5-D MODEL OF GERMBAND RETRACTION……. 42

4.1 Introduction……42
4.2 Results……44
4.2.1 Construction of 2.5D cellular finite element model…… 44
4.2.2 Base model approximates in vivo germband retraction……...46
4.2.3 Germband retraction is robust to variation in cell-cell interfacial tension…….. 49
4.2.4 Ramped amnioserosa-amnioserosa interfacial tension is required to match in vivo kinematics……..51
4.2.5 Germband retraction is dependent on cellular topology……..54
4.3 Discussion……... 56

5. PATHWAY TO A PHENOCOPY: HEAT STRESS EFFECTS IN EARLY EMBRYOGENESIS……. 59

Abstract…… 59
5.1 Introduction…… 60
5.2 Results……63
5.2.1 Do amnioserosa holes cause subsequent development defects? …… 68
5.2.2 Why do the holes expand so far? ……71
5.2.3 How do heat-shock-induced holes initiate? ……75
5.3 Discussion ……..79
5.4 Materials and Methods …….. 85

6. HOLES IN NORMAL AND ABERRANT TISSUE ARE A MECHANICAL FAILURE 86

6.1 Germband retraction requires a coherent epithelial sheet ……..86
6.2 Discussion ……..89

7. CONCLUSIONS AND FUTURE DIRECTIONS ……...91

7.1 Conclusions ……91
7.2 Future Directions ……... 93
7.2.1 Hypothesis 1: The amnioserosa alone is sufficient to drive germband retraction...93
7.2.2 Hypothesis 2: Germband retraction is independent of the ellipsoidal geometry of the embryo. ……... 94
7.2.3 Hypothesis 3: Germband extension is driven by active cell intercalation that results from anisotropic stress in germband cells. ……94

7.2.4 Hypothesis 4: Mutants that do not fail germband retraction take different "trajectories" through morphogenesis. 95

7.2.5 Hypothesis 5: Stochastic amnioserosa cell apoptosis during dorsal closure is regulated by mechanical coupling to caspase signaling pathways. 95

Appendix

A. A PRIMER ON BRODLAND'S CELLULAR FINITE ELEMENT MODEL 98

B. TABLE OF CELL-CELL INTERFACIAL TENSIONS 114

C. MATERIALS AND METHODS FOR CHAPTER 4 AND CHAPTER 6 115

D. EXPERIMENTAL PROCEDURES FOR CHAPTER 5 118

REFERENCES 122

LIST OF TABLES

Table Page

5-1: Prevalence of developmental defects observed after gastrulation-stage heat shocks. 67

LIST OF FIGURES

Figure Page

2.1: Timeline of embryonic development in *Drosophila*. 9

2.2: Ventral furrow invagination (VFI). 10

2.3: Dorsal closure. 13

2.4: Cephalic furrow formation and germband extension. 15

3.1: Kelvin-Voigt Element. 23

3.2: Geometric Rate Equation Model. 24

3.3: Deformation Gradient Decomposition Method. 28

3.4: Cellular Potts Model. 29

3.5: Vertex Model. 32

3.6: Germband Retraction (GBR). 35

3.7: Biological Significance of the Cellular Finite Element Model. 37

3.8: 2.5-Dimension Model of Germband Retraction. 40

4.1: Base model replicates *in vivo* germband retraction. 47

4.2: Germband retraction is robust to variation in cell-cell interfacial tension although kinematics vary. 50

4.3: Ramped amnioserosa tension replicates *in vivo* kinematics but polarized tissue stress and increased cell density do not. 53

4.4: Initial cell geometry determines extent of germband retraction. 55

5.1: Heat-shock-induced holes in the amnioserosa. 65

5.2: Dynamics of morphogenesis after heat shock. 69

5.3: Heat-shock-induced holes are statistically correlated with specific developmental defects. 71

5.4: Stage, location, and heat-shock dependence of amnioserosa tissue mechanics. 72

5.5: Heat-shock-induced holes do not trigger a wound healing response. 74

5.6: Holes initiate at failed cell-cell edges and after delamination events. 76

5.7: Junctional E-cadherin levels increase in the amnioserosa after heat shock. 77

5.8: Heat-shock-induced holes are anuclear and surrounded by cells with fragmented nuclei. ... 78

6.1: Model can replicate mutant and partial rescue *in vivo* phenotypes. 88

A.1: Single Cellular Finite Element. 100

A.2: Transformation of Coordinates. 107

CHAPTER 1

WHAT CAN BE LEARNED BY STUDYING BIOMECHANICS IN THE FLY EMBRYO?

Development of the embryo is intrinsically mechanical. Within epithelial cells, cytoskeletal structures generate force and withstand compression. In response, these cells deform and stretch, causing stresses and strains throughout the tissue. The result is a highly organized, heterogeneous, active material far from equilibrium. Studying the biomechanics of the active, living tissues of fly embryos has an impact on soft matter physics, entomology, developmental biology, and perhaps even medicine.

1.1 Pushing the Field of Soft Matter Physics

Cell-level biomechanics is the study of active soft matter. Unlike other forms of soft matter such as polymers, foams, or colloidal mixtures, active soft matter is composed of autonomous, living cells. This distinction is significant because active soft matter is capable of adapting to its environment. By sensing their surroundings, cells can change their behavior by altering the material properties of the tissue. Given this versatility, one may wonder to what degree classical principles of mechanics are valid for describing and predicting tissue morphology. Surely biology must obey the laws of physics, but does physics currently have valid models for cellular biomechanics? Is it valid to approximate a tissue as a foam or even a network of coupled springs, i.e. a finite element model? What considerations must be taken when the material is active?

1.2 Mechanical Analysis Improving Biological Understanding

In recent decades, biologists have heavily emphasized the role of genetics in development. Although genetics describes cell lineage and patterning genes, an embryo's final form is in no small part due to mechanics. Cells use gene products as mechanical machinery to produce forces and maintain or change morphology (Taber, Lin, & Clark, 1995; Wyczalkowski, Chen, Filas, Varner, & Taber, 2012). Cell morphological change then drives tissue shape and deformation during development, which is constrained by physical limitations of the embryo (Wyczalkowski et al., 2012). This mechanical view of the formation of the embryo, i.e., embryogenesis, provides fodder for questions that can inform biological understanding. For instance, are there predictable final configurations or phenotypes based on cellular topology and mechanical energy minima? Can mechanical analysis explain or even predict mutant phenotypes? If so, how broadly can these mechanical principles be applied to other insect species or even other phyla?

1.3 Cellular Biomechanical Studies beyond Physics and Biology

If a mechanical model can be built that accurately describes cellular interaction and even predicts phenotype, then this model can provide insight into how physical processes guide development. From a medical perspective, such insight could elucidate congenital diseases that are not genetically induced. Birth defects such as cleft palate and fetal alcohol syndrome are phenotypes that can arise without genetic mutation under adverse environmental and/or mechanical conditions in and around the developing embryo (Clarke & Gibbard, 2003; Delpisheh, Topping, Reyad, Tang, & Brabin, 2008; Ornoy & Ergaz, 2010; Ray & Niswander, 2012). A mechanical model of normal and aberrant tissue development is the first step in

understanding what goes awry in the embryo to cause such disease. Although this dissertation does not set out to solve or elucidate any medical condition, it does take an important step towards building a mechanical intuition of developing tissue.

1.4 Why *Drosophila*?

The fruit fly, *Drosophila melanogaster*, provides an excellent example of how mechanics plays a role in embryogenesis. Through the course of development, the embryo's tissues will deform and fold to transform the single-celled egg into a multi-organ larva. Many of these shape-deforming or morphogenetic changes occur in a single epithelium, where cells are tightly adherent to one another (Schöck & Perrimon, 2002). As cells autonomously deform, they induce forces on their neighbors that are transmitted across the entire epithelium (Allena, Mouronval, & Aubry, 2010; Allena, Munoz, & Aubry, 2013). In this way, a patch of only a few cells can play a major role in the morphogenesis of several thousand. Although these aspects of embryogenesis are not unique to *Drosophila*, there are a few features of *Drosophila* development that make it suitable for mechanical analysis.

First, *Drosophila* embryogenesis provides an ideal structure to study cell-level biomechanics. Early to mid-embryonic development occurs in the epidermal tissues, which are composed of a single, coherent epithelium (Schöck & Perrimon, 2002). Since this epithelium is a coherent layer of cells, one cell layer thick, morphogenesis may be studied as the interactions between cells and their immediate neighbors. The adhesion between cells facilitates large-scale tissue deformation through individual cell deformation (Pope & Harris, 2008). Indeed, all of the early to mid-embryonic stages of development can be studied in one epithelial layer, providing a consistent set of tissues that undergo morphological change.

Second, the embryo is a closed system. Specifically, the embryo is encased in an eggshell, which does not grow. The eggshell provides a boundary for embryonic development, which has two notable effects on the embryo: One, the embryo maintains a coherent epithelial tissue layer that surrounds the yolk and lies beneath the eggshell and vitelline membrane (Hartenstein & Hartenstein, 1993). The morphogenetic changes that occur within the epithelium are constrained apically and basally. Although it is possible for the epithelium to deform the yolk (Allena et al., 2010; Conte, Munoz, & Miodownik, 2008), these constraints tend to ensure the epithelium maintains a constant volume (Polyakov et al., 2014). Two, as the epithelium deforms, the energy that is used in the form of cell-cell interfacial tension is directed along the plane of the epithelium (Allena et al., 2010; G. Brodland, Chen, & Veldhuis, 2006). Since the epithelium is a continuous layer of cells, it is possible that one cell's deformation will cause a reactive deformation by any or all other cells in the epithelium. Thus, mechanical action may be transmitted throughout the epithelium in a conserved manner.

Third, there is a long history of mechanical models exploring *Drosophila* embryogenesis (Wyczalkowski et al., 2012). The majority of these models have focused on the particular stage of development known as ventral furrow invagination (VFI), which is the first major event after cellularization of the embryo. Indeed, this is the most studied event in several species including echinoderms, frogs, and zebrafish (Odell, Oster, Alberch, & Burnside, 1981). Beyond VFI, *Drosophila* mechanical models have included stages such as germband extension, germband retraction, and dorsal closure (Allena et al., 2010; Allena et al., 2013; Almeida, Bagnerini, Habbal, Noselli, & Serman, 2011; M. S. Hutson et al., 2003; Layton et al., 2009; Holley E. Lynch, Veldhuis, Brodland, & Hutson, 2014; Saias et al., 2015; Solon, Kaya-Copur, Colombelli, & Brunner, 2009; Zajac, Jones, & Glazier, 2000). The next chapter will take an in-depth look at

the history of these models, and the model addressed in Chapters 4 and 6 will explore the mechanics of germband retraction.

Finally, the developmental biology community has established an extensive set of experimental tools to study embryogenesis. These tools include genetic mutants of embryos that present intriguing phenotypes that can be used to validate a mechanical model. Additionally, the field uses markers such as fluorescent proteins tagged to cellular structures of interest in living tissue as well as immunofluorescence stains to mark features of fixed cells. Such markers pinpoint the cellular features that provide mechanical properties to the cell, such as adhesion junctions and actomyosin motors (K. A. Edwards, Demsky, Montague, Weymouth, & Kiehart, 1997; Oda & Tsukita, 2001). Chapter 5 explores experimental work on aberrant development of the embryo that takes full advantage of the genetic tools and markers available in the *Drosophila* system.

In summary, embryogenesis in *Drosophila* is an ideal system for biomechanical analysis for several reasons, such as the structure of the embryo and the benefits of working with a well-studied experimental system. Moreover, *Drosophila* provides a model for embryogenesis in other phyla. As noted above, there is a similarity between VFI in *Drosophila* and other animals; but also processes such as dorsal closure mimic wound healing in mammals. Even more generally, biomechanical analysis of tissue morphogenesis in normal and aberrant conditions may eventually have consequences in medicine.

1.5 Overview

Here, I present a collection of work that explores the stress fields of normal and aberrant tissues *in vivo* and *in silico*. A review of biomechanical models in Chapter 2 explores epithelial

stresses and strains evident in various stages of *Drosophila* embryogenesis. Trends of mechanical robustness and three-dimensional effects on these tissues are discussed, suggesting there exists a mechanical trade-off between cell-type dependent tensions and embryo-imposed constraints on cells. The modeling formalisms used in this chapter are analyzed in Chapter 3. One formalism, a cellular finite element model, is selected for modeling in subsequent chapters, and a primer on this formalism is developed in Appendix A. Using this formalism, a 2.5-D cellular finite element model is built in Chapter 4 and used to analyze the mechanics of one stage of development, germband retraction. This analysis finds that germband retraction is robust to cell-type dependent tensions, but contingent on the initial cell geometry. This result is experimentally tested in Chapter 5 with an investigation of the embryo's mechanical robustness to environmental perturbation. A non-specific heat shock stress is applied early in embryogenesis, resulting in delayed development and the formation of holes in the epithelium. These holes disrupt the mechanical integrity of the tissue and prevent further development, specifically during germband retraction. The model is expanded in Chapter 6 to explain why germband retraction fails when discontinuities are present in the epithelial tissues, thus providing a mechanical explanation for failure due to holes in heat-shocked embryos. Chapter 7 proposes future directions for this work. This dissertation provides a biomechanical explanation for normal and aberrant embryo development in *Drosophila*.

CHAPTER 2

MODELING EMBRYOGENESIS

Embryogenesis is an exciting time in the fly's life-cycle. Stages of development are marked by cell migration events, which transform the single-celled egg into a multi-organ larva. These morphogenetic milestones require extensive coordination between autonomous cells. Despite the need to coordinate more than 3000 cells in the epithelial tissues alone, embryos consistently develop into recognizable phenotypes. Certainly there is an argument that this developmental consistency is due to genetics, but I propose there is also a role for mechanics.

Mechanical modeling of *Drosophila* embryogenesis has historically focused on four main stages of development: ventral furrow invagination, germband extension, germband retraction, and dorsal closure. As shown in the timeline in Figure 2.1, these stages are sequential, comprising a continuity from one stage to the next. Not only do they occur continuously through time, but also morphogenetic events occurring in all four stages can be described by cells in a single, coherent epithelium. Despite their progression and common epithelium, models of embryogenesis have focused on each stage independently as isolated events. In particular, the stages of ventral furrow invagination and dorsal closure have received the greatest attention. In this chapter, I review what these models reveal about the mechanics of each stage, as well as synthesize these isolated models to illuminate trends across multiples stages of embryogenesis. The goal is to tackle the question: *How do the mechanical contributions of individual cells translate into epithelial morphogenesis?*

Significant effort has been made to answer this question using biomechanical modeling. Previous embryogenesis modeling efforts worked under the assumption that some select group of

cells in the embryo actively change their shape, while others passively deform. The resulting morphogenesis is thought to be due to active cells "driving" tissue-level deformation. Models support this assumption by identifying which select set of active cells are sufficient to produce tissue deformation. The pursuit to identify a set of active cells is exemplified best in the extensive modeling of ventral furrow invagination.

2.1 "Active" versus "Passive" Roles for Cells in Ventral Furrow Invagination

Ventral furrow invagination (VFI) has captured the interest of modelers for many decades. This interest is due to the commonality of epithelial invagination in animal development beyond *Drosophila*, including frogs, fish, sea urchins, mammals, and humans. (Odell et al., 1981). In *Drosophila*, VFI occurs during gastrulation in Bownes stage 6, roughly 3 hours after fertilization, involving two tissues, the ectoderm and mesoderm (Brody, 1999). These tissues form a coherent epithelium surrounding the yolk and enclosed by the vitelline membrane, which lies directly beneath the eggshell (Figure 2.2A). As development proceeds, the mesoderm buckles towards the yolk into the interior of the embryo, while the ectoderm pinches together to seal up the invagination, forming a continuous ventral surface (Figure 2.2B, (Leptin, 1999)). Figure 2.2 depicts the specific sequence of four cell shape changes that accompany VFI *in vivo*: (1) apical constriction of the mesoderm during ventral furrow formation, (2) mesodermal apical-basal (radial) elongation within the invaginating furrow, (3) mesodermal apical-basal (radial) shortening while maintaining apical constriction to close the furrow, and (4) ectodermal apical-basal (radial) elongation occurring simultaneously with the previous steps (Polyakov et al., 2014). To date, there are no experimental measurements of the forces associated with these

cellular deformations. The question that models address is, *Which of these cells, and specifically which cell shape changes, are actively driving VFI?*

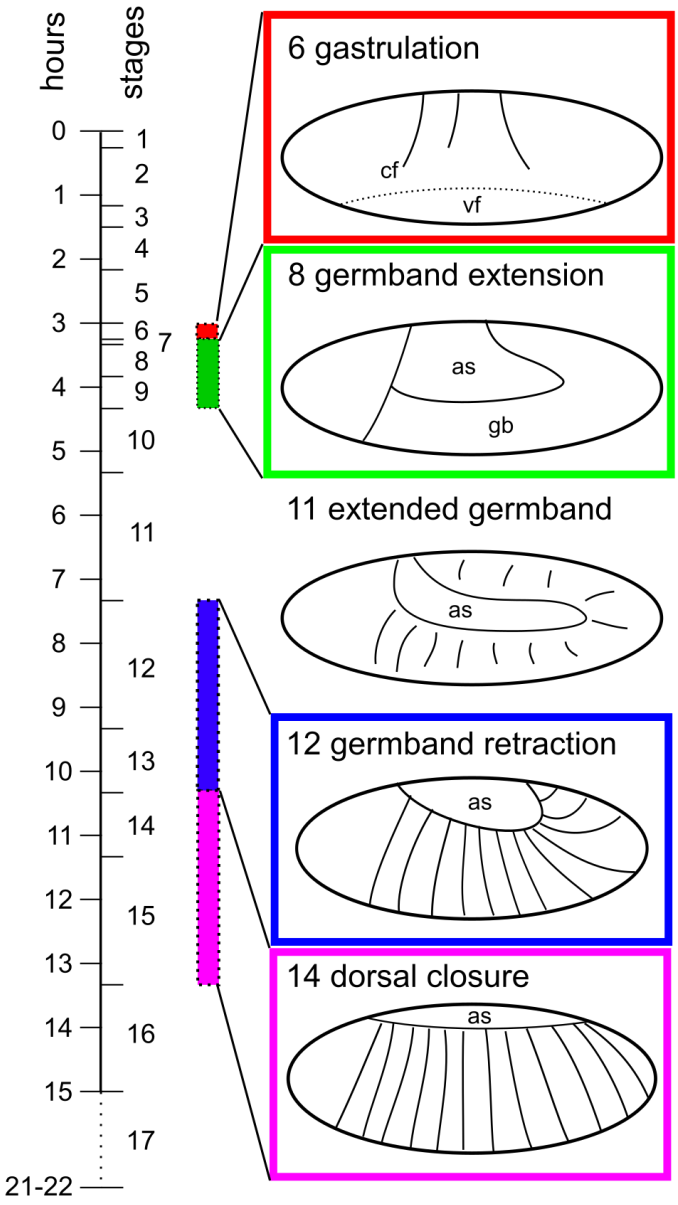

Figure 2.1: **Timeline of embryonic development in *Drosophila*.** Bownes stages of development are presented for an embryo developing at 25°C. Four stages of development are highlighted: gastrulation, germband extension, germband retraction, and dorsal closure. The images depict a snapshot of epithelial morphology during each stage. There is a pause in epithelial morphogenesis during stages 10-11, where the epithelium remains stationary. Approximately one-third of development has been modeled. Significant stages that remain to be studied include cellularization (5), the transition from germband extension to germband retraction (11), head involution (16), and internal organ development (throughout). cf, cephalic furrow; vf, ventral furrow; as, amnioserosa; gb, germband. Data for image obtained from Brody (1999); Hartenstein and Hartenstein (1993).

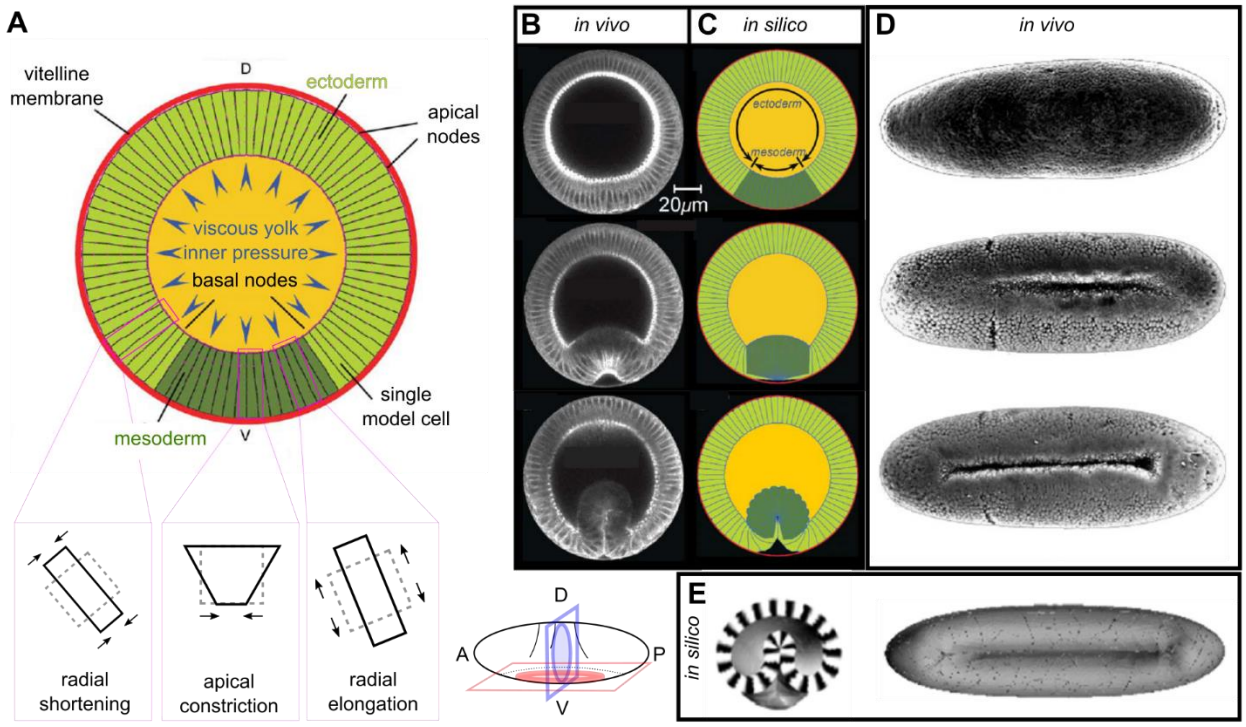

Figure 2.2: Ventral furrow invagination (VFI). The embryo compass (bottom, center) describes two planes of interest to study VFI: transverse cross-section (blue) and the ventral plane (red). In this and following figures, the compass directions are anterior, A; posterior, P; dorsal, D; ventral, V. (**A**) The transverse cross-section of the embryo shows two epithelial tissues that coordinate in VFI, the mesoderm and ectoderm. The cells in these tissues undergo deformations corresponding to the boxes below. (**B**) *in vivo* and (**C**) *in silico* (2D) time points of VFI as viewed from the transverse cross-section. (**D**) *in vivo* time points and (**E**) *in silico* (3D) final configuration of VFI as viewed from the ventral plane. The 3D cross-section view in (**E**) is marked with a smoothing Heavyside function to represent the active deformations (white) and passive deformations (black) resulting from the Deformation Gradient Decomposition method. These images are modified from the following: (**A-C**) (Conte et al., 2012), (**D**) (Grumbling & Strelets, 2006), (**E**) (Allena et al., 2010).

All of the models agree that mesoderm apical constriction is essential for VFI, but there is disagreement on whether or not the ectoderm plays an active role. Some models suggest that the ectoderm actively pushes the mesoderm to invaginate (Conte, Munoz, Baum, & Miodownik, 2009; Conte et al., 2008; Jose J. Munoz, Barrett, & Miodownik, 2007). Others maintain that mesodermal apical constriction alone is sufficient to drive VFI (Allena et al., 2010; Hocevar Brezavscek, Rauzi, Leptin, & Ziherl, 2012; Odell et al., 1981). One may suspect that the

discrepancy between these models is a result of different modeling formalisms – in other words, the conflicting solutions are due to a difference in the modeling methodology. Certainly, there are significant differences in the types of models used to study VFI (see Chapter 3), but I believe the distinction is more general. Upon examining these models, it becomes apparent that those that find apical constriction alone is capable of producing VFI include a cellular volume constraint (Hocevar Brezavscek et al., 2012; Odell et al., 1981). All other models requiring ectoderm radial shortening allow cell volumes to vary (Conte et al., 2009; Conte et al., 2008; Conte et al., 2012; Jose J. Munoz et al., 2007; J. J. Munoz, Conte, & Miodownik, 2010). Thus, the distinction between models lies in an assumption: the model either does or does not conserve cell volume. There are two interesting observations that can be made in light of this distinction.

First, this discrepancy in the models points out how easy it can be to overlook or misunderstand the importance of underlying assumptions. In the models that did not conserve volume, cell volume was not explicitly assigned to be a variable. Jose J. Munoz et al. (2007) and the follow-up papers did not even define cells in their models. They used a finite element method that considered deformations to local regions of tissue, so cell volume does not have meaning in their model. Conte et al. (2012) defined a surface area constraint on their cells rather than a volume constraint. Without experimental evidence to justify any other choice of parameters, this assumption is not any more or less reasonable. Polyakov et al. (2014) show experimental data that provides evidence that cell volume is conserved, so it appears that active ectodermal forces are not necessary. Nevertheless, both modeling results remain valuable, which we will discuss later.

Second, models cannot determine how biology functions. They merely illuminate plausible mechanisms and rule out implausible ones. In this case, two plausible mechanisms of

VFI were found: with or without active ectodermal forces. The experimental data suggests that since cell volume is conserved, ectodermal forces are not necessary. However, the experimental data does not show whether or not ectodermal forces exist. Indeed, other possible scenarios were considered by the models that were capable of producing VFI. Conte et al. (2012) successfully applied forces to the mesoderm lateral and apical sides, as well as the ectodermal lateral edges, and considered the system "overdetermined," meaning that these forces are redundant. Although the models have narrowed down the critical forces that are sufficient to drive VFI, it does not rule out the possibility that the mechanical contributions of cells are redundant. If multiple cells are capable of contributing to a morphogenetic event, perhaps the question of whether cells are "active" or "passive" is not informative. Rather, it might prove more useful to determine whether or not cell contributions are redundant, suggesting the stage of development is robust. This idea of mechanical robustness is apparent in a different stage of *Drosophila* embryogenesis, dorsal closure.

2.2 Mechanical Robustness in Dorsal Closure

Dorsal closure is a process involving four groups of cells working in tandem, which has prompted several models to explain the contribution of each. As shown in Figure 2.3A, after the germband has fully retracted, the extraembryonic amnioserosa tissue lies on the dorsal surface in a pinched ellipse flanked by two lateral edges of the germband. The four components of dorsal closure are as follows: First, the two leading edges of the germband move towards one another to close over the amnioserosa forming a coherent ectoderm. Second, individual cells in the amnioserosa exhibit stochastic pulsatory contractions and apoptotic activity to reduce their apical surface area. Third, a supra-cellular actin cable forms on the boundary of the amnioserosa and

the leading edge called a "purse string," contracting with a tensile stress. Fourth, the two lateral edges of the amnioserosa extend active protrusions of lamellipodia, which connect to "zip" the pinched corners together. All four of these events act simultaneously to close the dorsal surface such that segment boundaries on opposite leading edges align with their corresponding counterpart.

The contributions of each of these components of dorsal closure are investigated with an analytical geometric rate model proposed by M. S. Hutson et al. (2003) (Figure 2.3A, described in detail in Chapter 3). This model considers the rate of closure for the damped system. Using a simple derivation of Newton's Second Law, they consider the balance of forces at the apex of the

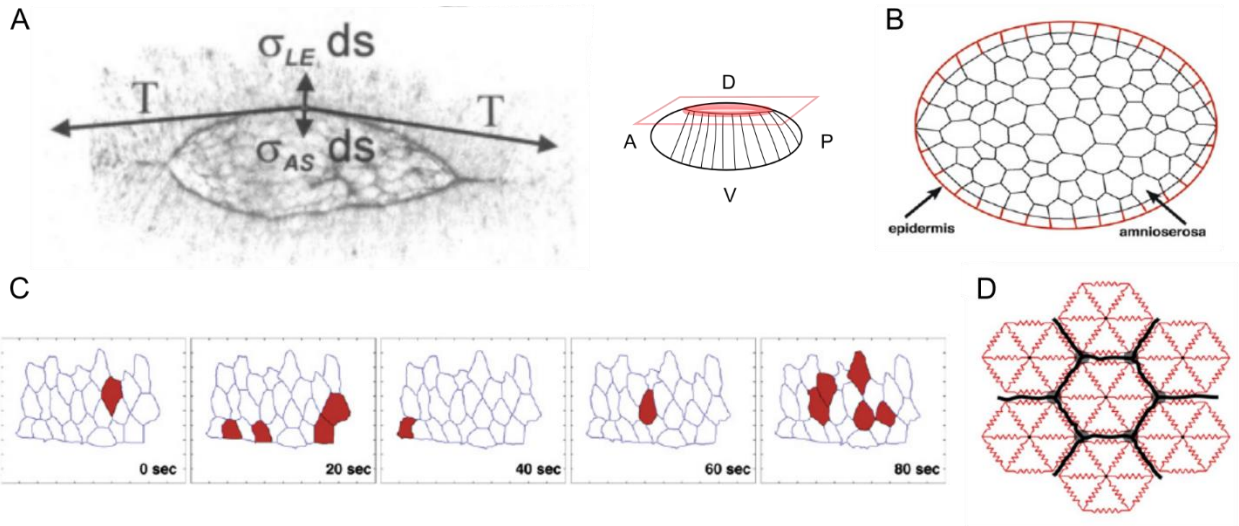

Figure 2.3: Dorsal closure. (**A**) The balance of forces during dorsal closure is used to describe the geometric rate equation derived by M. S. Hutson et al. (2003). Forces provided by internal amnioserosa stress ($\sigma_{AS}ds$) and the tension along the purse string (T) are balanced by the resistance of the leading edge of the germband ($\sigma_{LE}ds$). (**B**) Model of a ratchet-like mechanism in which amnioserosa cell oscillations reduce the tissue area and the surrounding actin purse string maintains the rate of closure. (**C**) Oscillations in amnioserosa cell areas on the apical surface are stochastically triggered. Cells initiating a contraction phase are highlighted in red. (**D**) Viscoelastic elements along spokes and edges of the cells drive the oscillations in this model. The viewing plane is on the dorsal side. Images are modified from (**A**) M. S. Hutson et al. (2003) (**B-D**) (Solon et al., 2009).

curved border between the amnioserosa and leading edge,

$$b\frac{dh}{dt} = \sigma_{LE} - \sigma_{AS} - T\kappa, \qquad \text{Eq. 2-1}$$

where $b\frac{dh}{dt}$ is a viscous damping term dependent on the velocity of closure, $\frac{dh}{dt}$; σ_{LE} is the force per unit length of the leading edge; σ_{AS} is the force per unit length of the amnioserosa; T is the tension along the purse string; and κ is the curvature of the purse string. They note that although the zipping force is not directly reflected in Eq. 2-1, it does anchor T, and κ depends on the rate of zipping (not shown here). The velocity of closure, $\frac{dh}{dt}$, is found to be constant even in perturbed tissue. Using laser microsurgery, they systematically remove the contribution from each of the four force components and use the model to derive a ratio of force contributions. Together, the amnioserosa and the actin purse string account for two-thirds of the active force pulling the leading edges together. The remaining one-third of the force is accounted for by zipping at the canthi, and is shown to only contribute significantly towards the end of dorsal closure. The leading edges only provide a passive viscoelastic resistance to dorsal closure (M. S. Hutson et al., 2003). Thus, dorsal closure is the result of three active cellular forces coordinating to close the dorsal surface against a resistive leading edge.

The key feature of dorsal closure is the redundancy of the forces that drive the process. When M. S. Hutson et al. (2003) perform the laser microsurgery experiments to remove the contribution of one of the forces, dorsal closure still proceeds. Several models have investigated how each tissue is able to produce their respective forces; however, similar to VFI models, these models fail to highlight that dorsal closure is robust to the distribution of forces across tissue. If an embryo is robust and cellular contributions are redundant, how much of an impact can a small

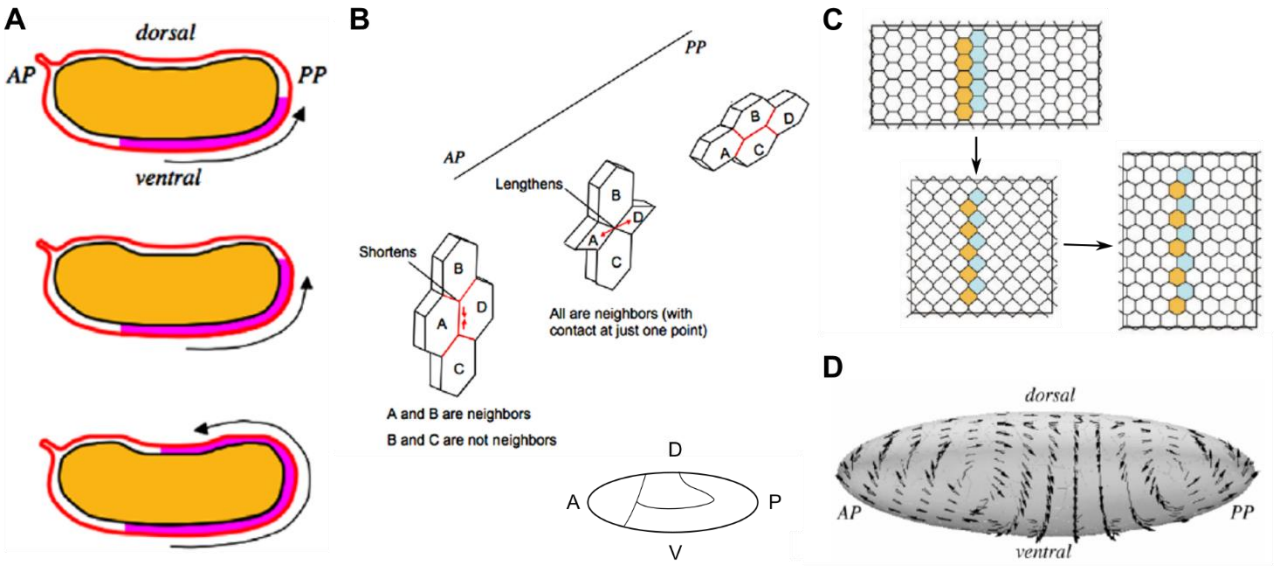

Figure 2.4: Cephalic furrow formation and germband extension. (**A**) Germband extension immediately follows gastrulation. The germband (pink) initiates on the ventral surface and extends through convergent extension around the posterior pole (PP) onto the dorsal surface toward the anterior pole (AP). (**B**) Cell intercalation has been shown to play a role in convergent extension during germband retraction. Intercalation involves T1-transitions between neighboring cells, which occur as the tissue elongates toward the posterior. (**C**) Cell intercalation leads to convergent extension of a tissue. (**D**) Embryo-wide cell flow produced by convergent extension of a small ventral patch of germband cells. Images modified from (**A**, **B**, **D**) (Allena et al., 2010), (**C**) (Honda, Nagai, & Tanemura, 2008).

patch of cells make on the whole embryo? To answer this question we turn to models of germband extension.

2.3 Small Cell-Level Changes Produce Embryo-Wide Deformations in Germband Extension

Immediately following VFI, ectoderm cells on the ventral and lateral sides of the embryo form the germband. These cells undergo convergent extension, which pushes the ventral germband around the posterior pole of the embryo toward the dorsal side (Figure 2.4A). During germband extension, germband cells initiating on the posterior pole of the embryo translate 75% of the embryo length along the dorsal side (Allena et al., 2010). Irvine and Wieschaus (1994)

reported that the process of convergent extension was characterized by cell intercalation events within the germband (shown in Figure 2.4B). This observation raises the question: Are cell intercalation events sufficient to drive germband extension? There have been two modeling approaches taken to address this question: First, a cell-level description is used to determine if intercalation is capable of producing convergent extension. Second, a tissue-level description of continuous deformation investigates the net effect of convergent extension on germband translation.

Modeling at the cell level has illuminated several mechanisms for convergent extension. Theories such as the Differential Adhesion Hypothesis (Steinberg, 1963) and the alternative Differential Interfacial Tension Hypothesis (G. W. Brodland, 2002) have shaped our understanding of how protein-level interactions between adhesion junctions and actomyosin networks, respectively, can coordinate cellular migration within an epithelial tissue (for a review of these two hypotheses, refer to (Mehes & Vicsek, 2014)). According to Zajac et al. (2000), cell elongation, cell alignment, and tissue elongation can all be achieved by assigning a specific adhesion energy anisotropy between cells. This differential adhesion is sufficient to reshape the tissue, and can potentially cause cell intercalation events. Thus, they propose convergent extension is a result of an anisotropic distribution of adhesion junctions within cells. Honda et al. (2008) make a similar assumption about the distribution of myosin II within cells, proposing convergent extension is driven by differential tension rather than differential adhesion. Using a vertex model to assign cell-cell interfacial tension anisotropically, they show that polarized myosin II accumulation within cells can account for cell intercalation through a series of T1-transitions, shown in Figure 2.4B. Cell-cell interfaces carrying a greater tension contract, reducing the interface length, which in turn contracts the cell perpendicular to the axis of tissue

elongation. When the cell edge is sufficiently short, the two adjacent cells lose contact allowing two previously separated cells to become neighbors. Honda et al. (2008) found that contraction of only one cell-cell edge per cell is sufficient to elongate the tissue to a maximum 2.5-fold elongation (Figure 2.4C), which matches the extent of germband extension (Allena et al., 2013). These two methods, using anisotropic adhesion energy or anisotropic tension along cell-cell interfaces, present plausible mechanisms for convergent extension involving cell intercalation in a homogeneous tissue.

Considering the embryo as a continuous tissue, Allena et al. (2010) investigate the bulk tissue deformation necessary to produce the convergent extension process of germband extension. They find that simply shortening tissue along the dorsal-ventral axis and elongating tissue along the anterior-posterior axis in a small patch (equal to roughly 200 cells in area) is not only sufficient for translation of germband cells to the dorsal side, but it also replicates cell flow (Figure 2.4D). Referencing cell velocity fields experimentally analyzed with a particle tracking tool (Supatto et al., 2005), Allena et al. (2010) report their model reproduces *in vivo* cellular acceleration toward the pole and whirlpool swirling patterns at the dorsal-lateral position. These cell trajectories describe significant migration along the entire embryonic epithelial tissue. Thus, germband extension can be replicated on a tissue level by applying active deformation akin to convergent extension.

Taken together, these two models hint at a subtle feature of embryogenesis: epithelial cells are well connected. This inherent property of epithelial tissue has significant ramifications. The cumulative effect of small topological rearrangements occurring at the cell level in the model presented by Honda et al. (2008) is capable of elongating the germband 2.5 fold. On the tissue level, this deformation causes cell flow throughout the epithelium (Allena et al., 2010).

Perhaps, a well-connected epithelium is able to shed light on how forces generated by different groups of cells are all able to produce embryo-wide deformation. To see the full impact of this mechanical coupling, I return to VFI.

2.4 Mechanical Coupling in Ventral Furrow Invagination

Models of ventral furrow invagination (VFI) diverge in their conclusion on whether or not an ectodermal force is necessary, which seems to be dependent on conservation of cell volume. There is a reason that cell volume makes such a profound difference on the results of the models. Working under the assumption that cell volume is conserved, Polyakov et al. (2014) present a mechanical description of how apical constriction of the mesoderm can transmit forces through the embryo to produce VFI. As a mesoderm cell constricts its apex, positive isotropic pressure is produced in the cell due to the volume constraint. Since the cell is bound by a rigid vitelline on the apical surface and by neighboring cells on its lateral sides, the cell elongates radially into the yolk. At this point, they suggest the rigidity of the lateral cell surface results in a spring-like restoring force that pulls the apical surface away from the vitelline causing invagination. One may consider an alternative explanation as well: rather than invagination being the result of lateral edge stiffness, invagination is the result of mechanical coupling with the yolk and ectodermal cells. When the mesoderm apically constricts and radially elongates as they described above, it pulls on the neighboring ectoderm, tending to elongate the ectoderm cells in the circumferential direction. Now, a negative pressure is induced in ectoderm cells as they maintain constant volume, which serves to shorten the ectoderm radially, pulling on the yolk. The constant volume constraint of the yolk produces a similar negative isotropic pressure as its surface area expands to maintain contact with the thinning ectoderm. By a similar argument, the

yolk pulls the mesoderm internally, resulting in invagination. Without cell volume conservation, forces cannot be transmitted as cell pressures, and so an additional ectodermal force is necessary for VFI.

We are beginning to form an idea of what drives embryogenesis. The central idea is that morphogenetic events are mechanically redundant, meaning the forces from multiple groups of cells are independently sufficient to deform the tissue. If the stage of development exhibits mechanical redundancy, then robustness to force allocation within the embryo is the result of mechanical coupling. This coupling is the consequence of a well-connected epithelium. Under these conditions, multiple cells are capable of contributing to morphogenesis within a single stage of development. Embryogenesis, though, occurs through multiple stages. The answer to "*how do individual cells affect epithelial morphogenesis?*" must address the coordination of cells across stages. Is it possible that mechanical information is not only transmitted through space, but also through time? Are the stages mechanically isolated, with cells producing force *de novo* for each morphogenetic event, or is there a persistence to the mechanics?

This dissertation addresses these questions by investigating a stage of development that serves a transitional role in embryogenesis, germband retraction. Germband retraction is set up to reverse the process of germband extension. In many ways it is a link, being a process that moves the extended cells of the germband and the amnioserosa into position for dorsal closure. In the next chapter, I review and select the best modeling framework for this stage of development. Care is taken to ensure appropriate assumptions are made in this model. In Chapter 4, a 2.5-dimensional model of germband retraction is presented. Within a single model, germband retraction is shown to be mechanically robust to the distribution of tensions among cells. This model then investigates how initial cell geometry plays a role in determining the extent of

retraction. The results of this analysis provide insight into how cell geometry is able to preserve mechanical information between stages. Chapter 5 experimentally explores how an environmental perturbation early in embryogenesis affects developmental mechanics, causing a failure in germband retraction. These *in vivo* studies test the necessity of a well-connected epithelium by inducing a hole in the amnioserosa. Chapter 6 models the results of the experimental data to test when germband retraction fails. The model is able to replicate several mutant and surgically-manipulated phenotypes, characterizing the resilience of germband retraction to mechanical perturbations. Finally, in Chapter 7, a brief summary of the work is presented along with suggestions for future directions.

CHAPTER 3

SELECTING A MODEL FOR GERMBAND RETRACTION

Previous models of *Drosophila* embryogenesis have prompted us to explore the mechanics of germband retraction. In order to model this dynamic process, several modeling formalisms have been developed. In this chapter, I will discuss four modeling formalisms that have been used to model embryogenesis in *Drosophila*, comparing each in their ability to describe and elucidate various aspects of development. As each formalism is described, consider three aspects of developmental mechanics that each model must address: observables, constraints, and mechanisms.

First, many of the observables that are included in models of development come from microscopy. Microscopy provides measurable information on cell shape, area, and aspect ratio. Tracking cells through time then extends these data to inform how cells deform, oscillate, maintain and exchange neighbors, and flow around the embryo. These observables are implemented into models in various ways, to greater or lesser accuracy depending on the models intended focus. Comparisons of these observables *in vivo* and *in silico* are then used as metrics to judge the quality of the model.

Second, epithelial cells *in vivo* are part of an embryo, and a model must account for the constraints that cells experience from its embryonic surroundings. Such constraints include the three dimensional structure of the embryo and the boundary conditions inherent to that structure. For instance, epithelial tissues are bound by an overlying vitelline membrane and egg-shell as well as an underlying yolk. Another constraint may include volume conservation of the cells or

the yolk. As we have seen in the previous chapter, the assumptions that are made in the model regarding these constraints may have a significant impact on the validity of the model.

Third, the mechanisms that the model employs to drive morphogenesis provide insight into development. Some modeling formalisms simply choose mechanisms that help elucidate which cells are active or passive. Others investigate the properties of the cells that are necessary for embryogenesis to proceed. Two of these properties, cellular viscosity and cellular force production, are worth further explanation here.

Cells are viscous. In fact, to a first order approximation, cells can be considered to be a viscous fluid. Of course, they have quite a bit of structure and they are active, living entities; but, nevertheless, on reasonably long time scales (~ hours) they behave like a fluid. The importance of viscous effects on cells can be described succinctly by Reynolds number, which is a ratio of inertial forces ($F = \text{mass} \times \text{acceleration}$) to viscous forces ($F = \text{coefficient of viscosity} \times \text{velocity}$). An object's size determines both its coefficient of viscosity, which typically scales as one length dimension, as well as its mass, which scales as the cube of length dimensions. For objects the size of the cell or smaller, such as molecules and proteins, the mass is orders of magnitude smaller than the coefficient. Thus, the inertial forces that they experience are negligible, while the viscous forces are significant. Processes within the embryo occur in low Reynolds conditions (Re ~ 10-4), where motion is dominated by viscous resistance (Purcell, 1977). In order for cells to deform, constant force must be applied since inertial motion is negligible. Although exact values of cellular forces are not known due to difficulties in measuring viscosity, quantitative analysis of strains and computational mechanical modeling can still provide insight into the stress fields in embryonic tissues.

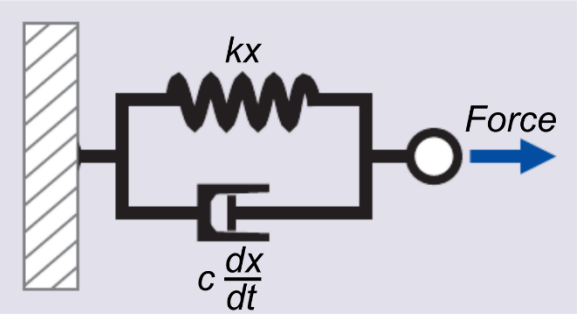

Figure 3.1: Kelvin-Voigt Element. Element consists of a spring and dashpot in parallel. The spring force is proportional to displacement; whereas, the force of the dashpot is proportional to velocity. Modified from (Dunn & Price, 2015).

Cellular forces may be modeled along cell-cell interfaces as viscoelastic Kelvin-Voigt elements, which consist of a spring and dashpot in parallel as shown in Figure 3.1 (Dunn & Price, 2015). A dashpot is a mechanical element that experiences viscous resistance as it is displaced, an effect equivalent to a plunger moving through a cylinder filled with a viscous medium. In parallel, these elements behave like solids on time scales of seconds, and flow and deform on scales of minutes and hours (Dunn & Price, 2015). Although exact values of tensions along cell-cell interfaces have not be measured *in vivo*, models can investigate ratios of tensions between homotypic and heterotypic cell-cell interfaces. Through this analysis it is possible to determine either if certain cells are actively driving specific developmental events, or if these events are mechanically constrained in a way that they are robust to cell-type dependent tensions.

In order to capture the mechanical features of embryogenesis, several modeling formalisms have been developed. Each formalism is unique, chosen specifically for the aspect of embryogenesis that the modeler intends to study. In this chapter, I will compare four of these modeling formalisms, highlighting advantages and disadvantages of each in the context of modeling embryogenesis. I will then point out aspects of germband retraction that we wish to model, and select the appropriate formalism, which is describe in detail in Appendix A.

3.1 Four Modeling Formalisms for Embryogenesis

3.1.1 Geometric Rate Equation Models

The Geometric Rate Equation model uses simple geometric shapes and a straight-forward rate equation to describe tissue-level deformation. The equation is a statement of Newton's Second Law, reducing the mechanics of the epithelium to an analysis of balanced forces. For example, recall from Chapter 2 that we considered the model of dorsal closure (M. S. Hutson et al., 2003). Figure 3.2A shows the force diagram created for the geometric rate equation superimposed on the tissues. The force contribution of each tissue was determined by laser ablation as described previously. In order to define the parameters of these forces, the amnioserosa was approximated as the intersecting arcs of two circles, as shown in Figure 3.2B. Using these geometric shapes, ratios of distances are used to describe the tissue. In general,

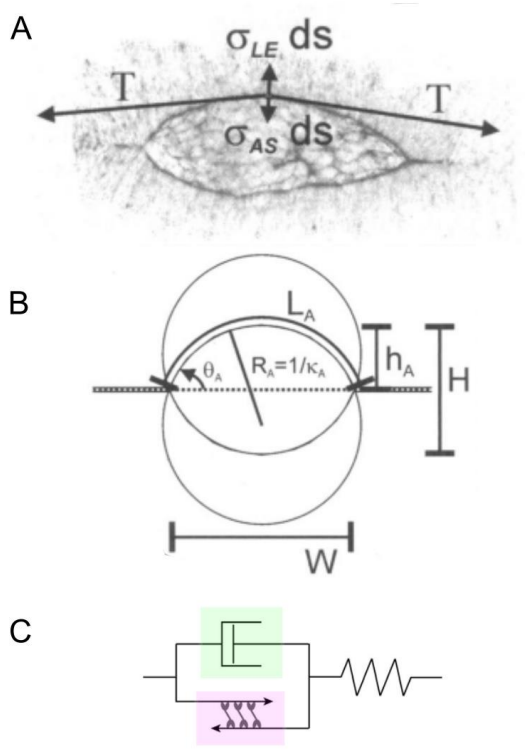

Figure 3.2: Geometric Rate Equation Model. (**A**) The balance of forces during dorsal closure is used to describe the geometric rate equation derived by M. S. Hutson et al. (2003). Forces provided by internal amnioserosa stress ($\sigma_{AS}ds$) and the tension along the purse string (T) are balanced by the resistance of the leading edge of the germband ($\sigma_{LE}ds$). (**B**) Simplified geometry of dorsal closure corresponds to (**A**). The image is from M. S. Hutson et al. (2003). (**C**) A viscoelastic element from Layton et al. (2009) is added to this model. The element contains a dashpot (green) and a force-generating actomyosin element (magenta) in parallel, coupled to a spring in series.

geometric rate equation models are not computer simulations, but rather mathematical formulations that, in some cases, are analytically evaluated.

This modeling formalism has several advantages for mechanical analysis. The biggest advantage is its simplicity, as a restatement of Newton's Second Law. This direct application of theory allows such a model to be solved analytically, yielding intuitive and unambiguous results. Second, it is typically developed alongside experiments for explanatory purposes. The validity of the model is ensured by directly tying the formalism's mechanism to experimental observables. With the capacity to directly implement measurements of displacement and velocity from *in vivo* experiments, a geometric rate equation can provide analysis of the force distribution across multiple tissues. In the M. S. Hutson et al. (2003) example, the exact proportions of force contribution were determined for each of the tissues; i.e., two-thirds of the active force originated from amnioserosa and actin purse string, and one-third from the zipping force at the canthi. Third, this modeling formalism can be adapted to provide insight into how each type of force is generated by these tissues. For example, the force from the actin purse string is modified by Layton et al. (2009) by including a biological force-producing element along the amnioserosa-leading edge border. As shown in Figure 3.2C, this element is very similar to a Kelvin-Voigt viscoelastic element (Figure 3.1), replacing the spring component with an active actomyosin network. This active actomyosin network produces constant tension such that the element tends to contract. Using this modification, they simulate microsurgery experiments, analyzing how the tissue reacts to perturbation through mechanical feedback. As a different example of modifying the model, Almeida et al. (2011) generalize the M. S. Hutson et al. (2003) model to a set of PDEs allowing more complex nuances of mutant development to be modeled. Simplicity and direct

implementation of experimental measurements can make this modeling formalism appealing, but it is limited.

The disadvantages of this modeling formalism are mostly the limitations of its capability. For example, the model assumes that tissues can be approximated as simple geometric shapes. Such approximations give a very coarse description of embryogenesis. Cell-level resolution would be difficult to implement for tissues containing numerous or irregularly shaped cells with geometric rate equation modeling. Without cell resolution, the model cannot test force-producing elements at the cell level, limiting the models usefulness to identifying tissue-level mechanics. Moreover, this formalism approximates tissues as flat, two-dimensional projections of the embryo, which limits the scope of the model to a narrow window of the embryo's epithelium. The models require imposed boundary conditions to approximate a continuous epithelium. Although this modeling formalism does provide intuitive, analytical insight into experimental data, it is poorly suited for testing cell-level stress or strain or properties inherent to a continuous epithelium.

3.1.2 Deformation Gradient Decomposition Models

Deformation Gradient Decomposition models provide a means to address which epithelial tissues are active and which are passive. Active tissues are deformed by geometric deformation gradients rather than active forces. Passive tissues are deformed by hyperelastic constraints that are imposed to maintain a continuous mesh. In this way, the active regions of deforming tissues can be determined by applying deformation gradients that correspond to *in vivo* measurements of cell shape change.

This method examines embryo-wide tissue morphogenesis by simulating localized deformations. Rather than explicitly modeling cells, the epithelium is divided into a mesh of

finite elements. As described in Figure 3.3, localized regions of this mesh are mapped from a coordinate space into a parameter space that redefines the region into a convenient regular shape. In parameter space, an active deformation gradient is applied, which corresponds to an observed cell shape change *in vivo*. The deformed parameterized mesh is then mapped back into coordinate space where a passive hyperelastic constraint is applied to preserve continuity between the deformed region and the surrounding mesh.

Deformation Gradient Decomposition is a practical method for biomechanical analysis that relies on morphological data. One advantage to this method is that input parameters are directly measured or observed, grounding the model with experimental evidence. A finite element mesh is used for the embryo's structure, so it is possible to create AutoCAD renderings of confocal microscopy images to build the model. Additionally, material properties can be directly input into the model. Indeed, Jose J. Munoz et al. (2007) specify material properties, such as Young's Modulus, $E = 1000$ Pa, and Poisson's Ratio, $\nu = 0.3$, based on measurements from sea urchins. Although, the accuracy of using sea urchin measurements for *Drosophila* models is unknown. This formalism tests the hypothesis that certain cell shape changes are actively responsible for morphogenesis while others are passively deformed. The model then returns bulk tissue movement and can even map cell and yolk flow (Allena et al., 2010). This result is useful for determining how constraints imposed by the embryo are mechanically involved in morphogenesis, but the method does not provide a complete mechanical picture.

Although this modeling formalism does distinguish between active and passive regions of the embryo, it fails to elucidate certain mechanical features of embryogenesis. Notably, this model assumes that tissues can be treated as a continuum with no cell-level discretization. This assumption makes it difficult to quantify material properties of individual cells, i.e. cell volume.

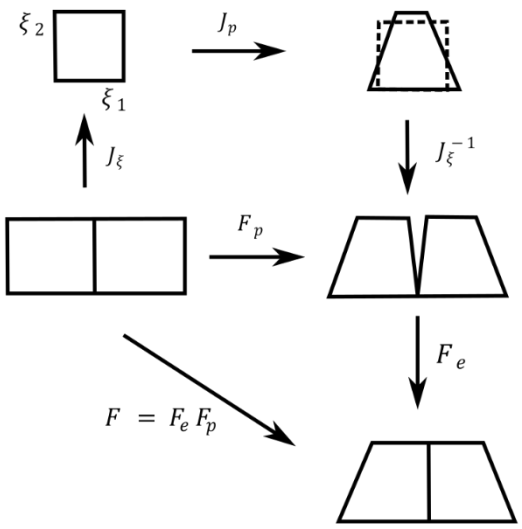

Figure 3.3: Deformation Gradient Decomposition Method. Starting at the center left, tissue-level deformations are described by a deformation gradient tensor, $\boldsymbol{F}$, acting on a continuum of finite elements. This tensor is decomposed into an active and a passive component. Active deformation field, $\boldsymbol{F_p}$, is imposed on individual finite elements by mapping the finite element to parametrized coordinates, $(\boldsymbol{\xi_1}, \boldsymbol{\xi_2})$, with a transformation matrix, $\boldsymbol{J_\xi}$. The parametrized active deformation, $\boldsymbol{J_p}$, such as "apical constriction," is then applied and the element is mapped back into the original coordinate system by the inverse transformation matrix, $\boldsymbol{J_\xi^{-1}}$. Thus, the active deformation gradient may be expressed, $\boldsymbol{F_p = J_\xi J_p J_\xi^{-1}}$. The actively deformed finite element mesh now contains discontinuities, and a passive hyperelastic deformation field must be applied, $\boldsymbol{F_e}$. The total deformation gradient is equivalent to the multiplicative decomposition, $\boldsymbol{F = F_e F_p}$. Image modified from Jose J. Munoz et al. (2007).

Further, deformation to tissue is the result of geometric transformations to finite elements rather than application of forces. This lack of forces is by design, allowing the model to work without knowledge of experimentally observed force, which is difficult to measure *in vivo*. Nevertheless, without explicit force dependence, the model is unable to test cellular or subcellular force-producing elements. Thus, cell movement by differential adhesion, cell intercalation, active acto-myosin contraction, and any other force-producing cellular action is indistinguishable.

3.1.3 Cellular Potts Models

Cellular Potts models simulate cell-level deformation by using a lattice-based architecture and energy minimization. As described by Merks and Glazier (2005), a Cellular Potts model defines a cell as a patch of lattice sites, $\vec{x}$, with identical indices, $\sigma(\vec{x})$, or "labels" selected on a grid lattice. (See Figure 3.4A) The cell-cell interface is a pixelated border between adjacent sites with indices assigned to neighboring cells. Cell deformation occurs at the level of single lattice sites where a site can switch index from one cell to its neighbor. These index reassignments are governed by a Hamiltonian function that accounts for cell properties, i.e. cell area and cell-cell adhesion. The flexibility of this modeling formalism lies in the ability to intuitively insert constraints on the system by adding energy terms. For example, a Hamiltonian will be of the following form:

$$H = \lambda \sum_{\sigma} (a_\sigma - A_\sigma)^2 \qquad \text{Eq. 3-1}$$

where λ is a pressure-based coefficient that resists compression, A_σ is a target area for the cell of

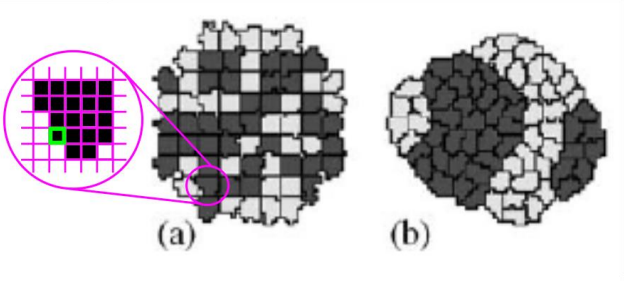

Figure 3.4: **Cellular Potts Model.** (**A**) A simulation of 69 cells are run for a few Monte Carlo steps. The inset shows a single black cell occupying 19 lattice sites. The green-highlighted site (previously white) has been randomly chosen to change it's index, σ, and become part of the black cell. If the state change is accepted by the Hamiltonian energy calculation, it will remain black; otherwise, it will return to the white cell. (**B**) Many Monte Carlo steps later, enough state changes have occurred for the cells to migrate and exchange neighbors. The cells have maintained area, but remain pixelated. Image modified from Merks and Glazier (2005).

index, σ, and a_σ is the current cell area. Hamiltonians typically contain energy terms that preserve a cell's area (corresponding to internal cell pressure) and surface energy (corresponding to cell-interfacial tension). They must also contain an adhesion energy term to ensure the cells remain contiguous. By adjusting the Hamiltonian, cell material properties can be easily tuned. The Hamiltonian is then used to determine when a cell will deform. As explained in Figure 3.4A, at each time step of a Monte Carlo-based algorithm, a border lattice site is chosen stochastically to switch index. If the new cell configuration is energetically favorable (less energy in the whole system), the index reassignment is accepted. If it is not energetically favorable, the reassignment is accepted with a small probability calculated by a Boltzmann weighting function, which allows for noise in the system. Thus, cell-cell interfaces are constantly fluctuating in Cellular Potts Models even after an energy minimum has been obtained.

The energy-based nature of these models gives them a high level of configurability. These models are particularly suitable for modeling cell interaction involving differential adhesion, such as cell intercalation. Additionally, Cellular Potts Models are capable of implementing reaction-diffusion based signaling directly on top of the cell-cell interfacial dynamics (Merks & Glazier, 2005). This capability allows these models to simulate patterning events that are regulated by signaling pathways. From a mechanical perspective, however, the lattice-based architecture is undesirable.

The Cellular Potts Model has a couple disadvantages that limit its use as a modeling formalism for biomechanical analysis. First, it assumes that cell dynamics occur at the cell-cell interface. Without superimposing subcellular structures into cells, it is difficult to find stable energy configurations for certain cellular morphologies, i.e., elongated cells with high aspect ratios (data not shown). Also, the pixelated cell-cell interfaces make it difficult to directly

determine forces that are being experienced by each cell (G. W. Brodland, 2004). Second, this formalism does not explicitly use cell viscosity. The lack of a viscosity parameter prevents models from accurately describing time dynamics of mechanical stress and strain (G. W. Brodland, 2004). Third, adhesion energies must be carefully chosen to ensure that cells do not stochastically move apart (G. W. Brodland, 2004). Although an epithelial tissue could plausibly develop holes between non-adherent cells under some circumstances (a case of which we will investigate in Chapter 5), holes are unlikely to occur in wild-type tissue.

3.1.4 Vertex Models

Vertex models simulate embryogenesis through cell-level deformations. Cells are defined as polygons with edges that intersect at triple-point vertices called nodes. There are two kinds of vertex models, energy-based and force-based, and they differ in the manner in which nodes are displaced. (See Figure 3.5.) Similar to the Cellular Potts Model, energy-based vertex models displace nodes by minimizing a Hamiltonian energy function akin to Eq. 3-1; whereas, force-based vertex models displace nodes using cell-level forces. These forces are composed of active force components that are typically applied along cell-cell interfaces. Within the cell, nodal displacement is dampened by passive viscoelastic forces. Net forces are localized at the nodes to determine the nodal displacement at each time step, which is solved using a standard system of equations for finite element models:

$$\boldsymbol{K} \cdot \boldsymbol{u} = \boldsymbol{f} \qquad \text{Eq. 3-2}$$

where $\boldsymbol{K}$ is the stiffness matrix, $\boldsymbol{u}$ is the unknown nodal displacement vector, and $\boldsymbol{f}$ is the vector of applied forces. Both energy- and force-based vertex models tend to be deterministic in describing cellular deformation compared to the stochastic Cellular Potts Model. When considering either of these models, it should be noted that they make a few assumptions.

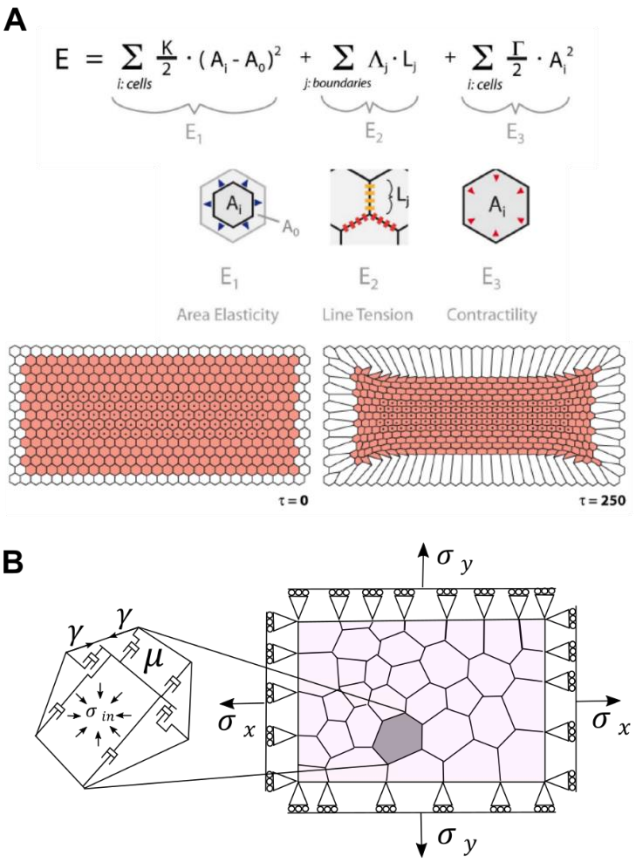

Figure 3.5: Vertex Model. (**A**) Energy-based vertex models are formalized by Hamiltonian energy terms. A visual discription of each term shows how vertices or nodes are diplaced. The collection of nodal displacements in each cell causes tissue-level deformation. A model of ventral furrow initiation shows how contraction of a select group of cells (marked with dots) will cause tissue-level contraction. Images modified from Spahn and Reuter (2013). (**B**) Force-based vertex models apply a net force at each node, causing cell and ultimately tissue-level deformation. In this example, constant tension, γ, is applied along cell-cell interfaces. Nodal displacement is resisted by damping forces, μ, through a network of dashpots, and an internal pressure, σ_{in}, provided by a cell area constraint. Far-field stress on the tissue is approximated by external aniosotropic stress, σ_x and σ_y. Image is modified from M. S. Hutson et al. (2003).

First, cell shape is polygonal. When cell-level descriptions of embryo mechanics are important, the ability to define individual cells is clearly an advantage over modeling techniques such as Geometric Rate Equations and Deformation Gradient Decompositions. For many epithelial tissues that undergo morphogenetic changes, this polygonal approximation in two-dimensions is adequate. One force-based vertex model of germband cells was able to analyze their elongated polygonal structure to determine the source of stress during germband retraction (Holley E. Lynch et al., 2014). There are, however, certain cell morphologies that exhibit curvilinear edges. One example of particular interest here is the highly elongated amnioserosa cells during germband retraction. In this case, a vertex model representation of these cells requires extra vertices along cell-cell interfaces to allow for cell concavity.

Second, cell deformation occurs at the vertices, while maintaining straight cell-cell interfacial edges. Although there are cases like the amnioserosa cells where this assumption may not be ideal, this vertex-displacement method is advantageous over the pixelated, stochastic edge displacement of Cellular Potts Models. Energy-based vertex models have been used to model intricate temporal and spatial dynamics, i.e. stochastic pulsing patterns in epithelial tissues during ventral furrow initiation and dorsal closure (Solon et al., 2009; Spahn & Reuter, 2013). On the other hand, since energy landscapes can contain local minima, it is possible for a local minimum energy configuration to halt a deterministic system. In this case, it may be necessary to add "jiggling" to the system with random noise applied to node displacement. In this way the system must hop out of local minima in order to settle into a true energy minimum. This is a disadvantage when compared to the Cellular Potts Model, which is unlikely to stay in a local, shallow energy minimum due to its stochastic Monte Carlo updating scheme.

Third, energy-based and force-based vertex models use two different methods of defining material properties. Energy-based models add terms to the Hamiltonian to define material properties to the whole cell. Similar to Cellular Potts Models, the Hamiltonian function is readily configurable, allowing easy inclusion of properties like cell-cell adhesion and area conservation; however, these properties are typically applied to the whole cell. It would be difficult, for example, to describe polarization within a cell causing it to contract one side and become wedge-like. The advantage of force-based vertex models is the ability to define sub-cellular forces. Since active and passive forces are explicitly defined within each cell, it is possible to test the role of individual cells. For example, models of ventral furrow invagination that define cell-level forces show mesoderm radial shortening is unnecessary; however, mesoderm apical constriction is required for invagination (Conte et al., 2012). This result is similar to what was found using

the Deformation Gradient Decomposition method, but it has the advantage of resolving the forces necessary to drive invagination (Conte et al., 2012). Since forces are the direct input into the system, mechanical properties of the cell are straight-forward to determine. Although the force-based vertex model is based on finite element principles that may be difficult to implement, it provides extensive capability.

3.2 Important Aspects of Germband Retraction to be Captured in the Model

Germband retraction is a highly active stage of embryogenesis occurring between germband extension and dorsal closure. Germband retraction involves the coordinated movement of two tissues: the extraembryonic amnioserosa, which forms during germband extension, and the germband. These two tissues maintain tight adherence between two interlocking U-shapes (Figure 3.6A). As germband retraction proceeds, the amnioserosa contracts onto the dorsal side to form an ellipse as it prepares for the subsequent stage of dorsal closure. The germband establishes well-divided segments and retracts back around the posterior pole to cover the ventro-lateral sides of the embryo. Unlike the previous stage of germband extension, it has been shown that no cell intercalation events happen during germband retraction (Schöck & Perrimon, 2002). In the absence of cell intercalation, several experimental studies have tried to determine the interaction of these two tissues in driving germband retraction (Frank & Rushlow, 1996; Lamka & Lipshitz, 1999; H. E. Lynch et al., 2013). One laser microsurgery experiment suggests that the amnioserosa mechanically assists in pulling the germband around the posterior end of the embryo. Another experiment shows that intracellular anisotropic stress can be produced in response to the amnioserosa, which may induce polarized contraction within the germband (Figure 3.6B). The idea is that this polarized contraction will shorten germband cells along the

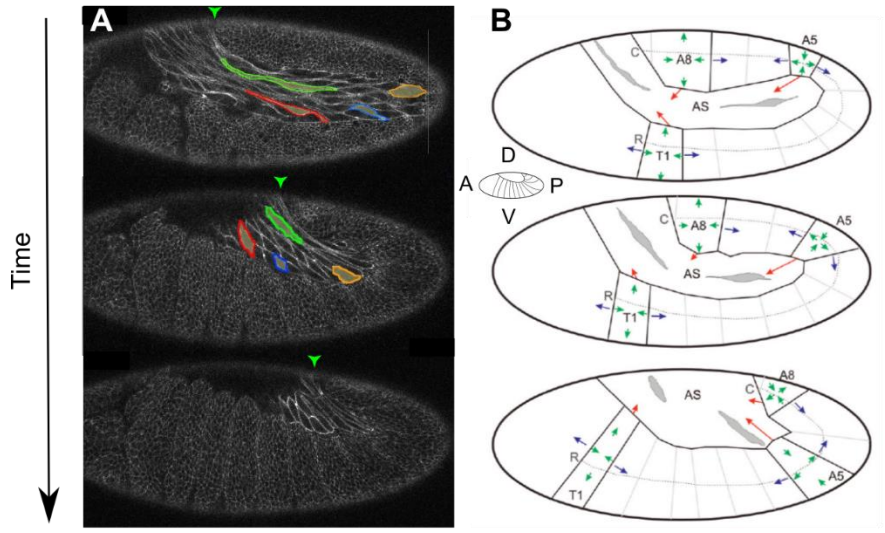

Figure 3.6: Germband Retraction (GBR). (**A**) The germband and amnioserosa form two interlocking "U" shapes. As the germband retracts around the posterior pole, the amnioserosa contracts onto the dorsal surface. Highlighted amnioserosa cells track strain through time. Green arrowhead marks the progress of GBR. (**B**) Anisotropic stress drives GBR. Arrows show stress applied to germband segments from: red, amnioserosa; blue, other segments; green, internal. Image from H. E. Lynch et al. (2013). Compass: D, dorsal; V, ventral; A, anterior; P, posterior.

axis of retraction, pulling the tissue around the posterior. In order to test this idea, we require a model of the entire epithelial surface that is capable of showing how localized, cell-based tensions affect global tissue deformations.

The model we require will need to approximate the mechanical properties of the germband and amnioserosa tissues. As shown in Figure 3.6A, these tissues are composed of a monolayer of tightly adherent cells, which undergo tremendous local strains while maintaining a coherent envelope around the yolk. This process occurs over the course of two hours (Brody, 1999; Hartenstein & Hartenstein, 1993). Despite the tremendous strain experienced by amnioserosa cells, in particular, we assume this time scale is too large for intracellular machinery to retain elastic energy – an assumption made previously by Chen and Brodland (2000). Moreover, embryonic cells do not lie on an extracellular matrix. Thus, the elastic properties of more fully developed tissues are not yet a part of embryonic epithelia (G. Brodland et al., 2006).

In other words, the cell shape changes that occur are not driven by elastic or inertial forces, but rather are driven by constant tensions produced by energy-consuming motors within the cell. These forces are resisted by viscous damping of the cytoskeleton, which must reorganize as the cell deforms. A model of germband retraction should include viscous damping and active tension, but not necessarily elastic forces. Additionally, the model should describe cell-level deformation, since changes in cell aspect ratio are dramatic. Based on the laser ablation experiments, it is also worthwhile to use a modeling formalism that is capable of assigning anisotropic stress to individual cells.

3.3 A Modeling Formalism for Germband Retraction

As reviewed above, mechanical modeling of *Drosophila melanogaster* embryogenesis has taken many forms. Embryos have been modeled in whole or in part as 3D finite element meshes or 2D cross-sections or projections of select cells from epithelial tissues (Conte et al., 2009; Conte et al., 2008; H. E. Lynch et al., 2013; Wyczalkowski et al., 2012). Although each of these has advantages, there is no model known to the authors that creates a mechanical surface of cell-shaped elements wrapped around an egg-shaped (ellipsoidal) last. Considering the aspects of germband retraction that we intend to model, we propose that a force-based vertex model is best suited for this application. The benefits of this type of modeling formalism include the ability to describe tissue deformation on a cell level. Forces are directly applied to individual cells with biologically relevant model components. It is also possible with this formalism to design a mesh of cells that lie in a sheet conforming to an ellipsoidal egg shape, which is essential to describe the global effects of localized interactions between cells. Specifically, we choose a Cellular Finite Element modeling formalism designed by Wayne Brodland and his lab (G. Brodland et al.,

2006; G. W. Brodland & Veldhuis, 2012; G. W. Brodland, Viens, & Veldhuis, 2007; Chen & Brodland, 2000). A detailed primer of this formalism is provided in Appendix A.

Importantly, the Cellular Finite Element model defines material properties of the cells in a biologically significant manner. Figure 3.7 shows how mechanically relevant biological structures are described in this formalism. Forces generated within cells are applied in the model by constant, active tension along cell-cell interfaces. These tensions represent the combined stress of microfilament bundles as well as the tangential component of adhesion from adhesion

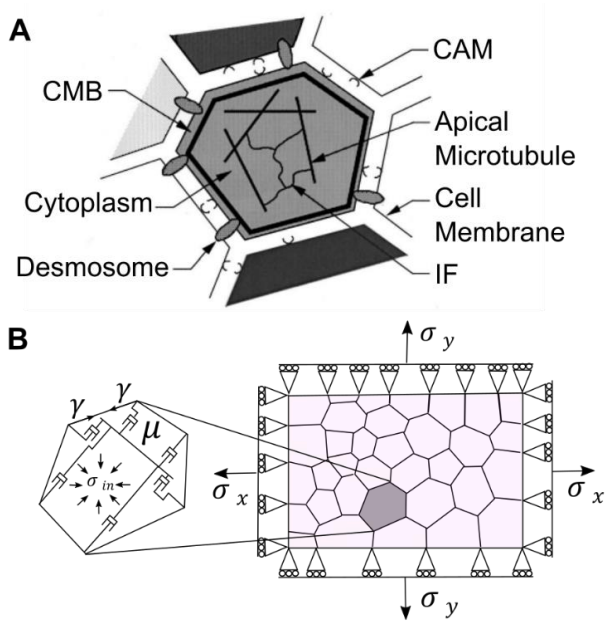

Figure 3.7: Biological Significance of the Cellular Finite Element Model. (**A**) Cells consist of many organelles and proteins that are mechanically significant. Cortical microtubule bundles (CMB), cellular adhesion molecules (CAM), and desmosomes exert forces along the cell membrane. The viscous cytoplasm and cytoskeletal network resist cell deformation. The cytoskeleton, specifically apical microtubules and intermediate filaments (IF), add in-plane stress to the apical surface that helps conserve apical area. Image from Chen 2000. (**B**) Cellular Finite Element model, depicted in Figure 3.5 is repeated here for convenience. Constant tension, γ, is applied along cell-cell interfaces. Nodal displacement is resisted by viscous damping forces, μ, through a network of dashpots, and an internal pressure, σ_{in}, provided by a cell area constraint. Far-field stress on the tissue is approximated by external anisotropic stress, σ_x and σ_y. Image is modified from M. Shane Hutson et al. (2009).

junctions (G. W. Brodland, 2002). Cell deformation is represented by nodal displacements, which resists motion by viscous damping (G. Brodland et al., 2006). This resistance accounts for the viscous cytoplasm and the cytoskeletal network. Cell area is also conserved by an effective internal pressure, which accounts for the incompressibility of the cytoplasm and the in-plane isotropic internal stress of the cortical cytoskeleton (M. Shane Hutson et al., 2009).

3.3.1 Building a 2.5-Dimensional Model of Epithelial Dynamics

In order to model epithelial dynamics, we assume that germband retraction occurs simply through the interaction of germband and amnioserosa tissues in mechanical isolation from the interior tissues. During stage 12, interior tissues such as the midgut epithelium, central nervous system precursor cells, and the mesoderm are still mesenchymal, having not yet formed a cohesive cell sheet through which forces could be propagated [(Schöck & Perrimon, 2002) and others cited therein]. Thus, these interior tissues are unlikely to make significant contributions to the mechanics of germband retraction as described here.

With this assumption, we construct a 2.5-dimensional last to model the epithelium. Each cell is defined as the simple polygon formed by a set of nodes constrained to lie on the surface of a prolate ellipsoidal last (1:1:2.5). The cell edges, which are linear stress elements, connect two nodes such that each node forms a triple junction of three polygonal cells. Each node is subjected to forces deriving from cell-cell interfacial tension, the corresponding elements of the viscous dashpot network, and the cell area constraint as described in the text. These cellular parameters are accounted for by the finite element solver's governing equation,

$$\frac{1}{\Delta t}\mathbf{C} \cdot \Delta\mathbf{u} = \mathbf{f} \qquad \text{Eq. 3-3}$$

where Δt is a simulation time step, $\mathbf{C}$ represents the damping matrix and contains information on the current geometry of the mesh, $\Delta\mathbf{u}$ is a displacement vector for each node, and $\mathbf{f}$ represents all non-viscous forces applied to each node, i.e., the constant cell-edge tensions. At each time step, this system of equations is augmented by applicable constraints assigned to each cell, e.g., constant area. These constraints are applied at each time step by Lagrange multipliers. (See Appendix A for further details.)

3.3.2 Constructing the Initial Mesh

One key feature of the early stage 12 embryo is the characteristically U-shaped amnioserosa tissue composed of highly-elongated cells (median aspect ratio ($\widetilde{AR}$) = 7.7). To create this mesh, a 2D ellipse (4:3) is filled with 120 randomly distributed seeds spaced by Monte Carlo distance minimization, which are then Voronoi tessellated. This tessellated ellipse is stretched to an aspect ratio of 12, giving the amnioserosa cells a median aspect ratio of 9.5, and is bent in the middle such that the stretched ellipse forms a U-shape with an arch radius that is 26% of the embryo length. Each triple junction node of this U-shaped 2D tessellated cell sheet is then mapped onto a 3D prolate ellipsoid, maintaining cell topology. The amnioserosa cells appear in yellow in Figure 3.8. Separately, the germband is created by seeding, spacing, and tessellating an ellipsoidal last using an ellipsoidal distance function,

$$\text{Distance along Ellipsoidal Surface} = \sqrt{\frac{(x_2-x_1)^2}{a^2}+\frac{(y_2-y_1)^2}{b^2}+\frac{(z_2-z_1)^2}{c^2}} \qquad \text{Eq. 3-4}$$

where a=1, b=1, and c =2.5 represent the semi-minor and major radii corresponding to the x, y, and z-axes. The germband cell mesh is then superimposed over the amnioserosa mesh on the same last. Triple junction nodes of the germband that lie within the amnioserosa tissue border are

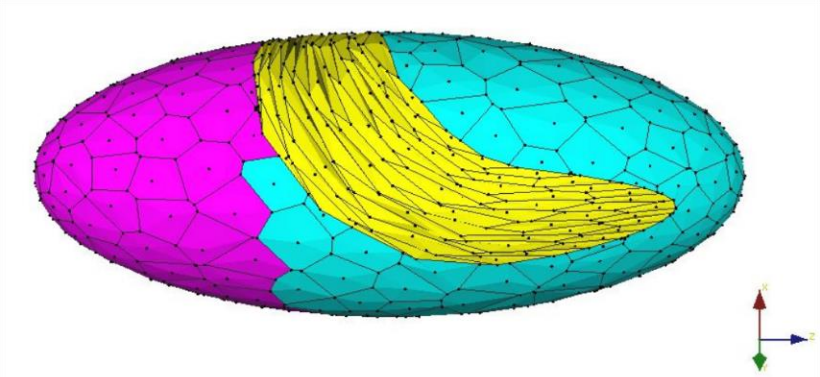

Figure 3.8: 2.5-Dimension Model of Germband Retraction. Each cell is formed as a polygon lying on the surface of an ellipsoidal last. Cells: magenta, head; yellow, amnioserosa; cyan, germband.

removed and new triple junctions are added where adjacent germband and amnioserosa cell edges intersect. This forms a continuous 2D mesh of connected triple junctions constrained to lie on the surface of a 3D ellipsoid. Germband cells are colored cyan in Figure 3.8. The head cells are chosen from germband cells whose centroids lie above a threshold on the z-axis that coincides with the anterior-most position of the amnioserosa. Head cells are colored magenta in Figure 3.8. *In vivo* data shows embryos typically contain roughly 120 amnioserosa cells and 3000 germband cells (data not shown). This study uses three meshes created as described with 120 amnioserosa cells and approximately 300 germband and head cells. Additionally, a fourth mesh constructed of 3100 amnioserosa and germband cells mesh is used. Simulations of the reduced cell mesh (1 modeled germband cell approximates 10 *in vivo* germband cells) complete 300 time steps in approximately 20 minutes, while the 3100-cell mesh completes in approximately 4 hours.

3.3.3 Exploring Germband Retraction with the Model

Using the 2.5-dimensional mesh and the Cellular Finite Element method, we proceed to investigate the mechanical contributions of epithelial cells towards germband retraction. Germband retraction occurs midway through *Drosophila* embryogenesis, involving substantial deformation to two tissues. Within these two highly connected tissues, cells proceed through deformation while maintaining a coherent, contiguous epithelium that conforms to the eggshell. Additionally, these cells do not intercalate, but rather migrate over distances spanning the embryo through cell shape change. This collective cell migration presents an intriguing example of cellular coordination within the context of imposed embryonic constraints that can be studied mechanically. Our model specifically addresses two questions: First, is germband retraction mechanically redundant, meaning, are multiple groups of cells sufficient to drive the process? Second, if so, what aspects of germband retraction ensure these various cells coordinate?

CHAPTER 4

CELL GEOMETRY PROVIDES MECHANICAL ROBUSTNESS: A 2.5-D MODEL OF GERMBAND RETRACTION

Authors of Manuscript in Preparation
W. Tyler McCleery, Jim Veldhuis, G. Wayne Brodland, M. Shane Hutson

4.1 Introduction

Embryogenesis is a dynamic process involving the coordination of cells spanning the organism. Epithelial cells, in particular, must coordinate movement in order to form the tissues that define the organism whilst maintaining tight adherence with their neighbors. The *Drosophila melanogaster* embryo provides an interesting model system to explore the mechanical conditions under which this collective cell migration occurs. Here, two epithelial tissues - the germband and the amnioserosa - undergo substantial morphological changes during a process midway through embryogenesis (Bownes stage 12), germband retraction (Schöck & Perrimon, 2002). From a mechanical perspective, cells migrating within these two tissues are constrained in three ways: they enclose the embryo, forming a coherent, contiguous epithelial cell monolayer; they conform to the vitelline membrane, maintaining an eggshell shape throughout retraction; and they do not intercalate, migrating only through cell shape change (Blanchard et al., 2009; Schöck & Perrimon, 2002). Given these three constraints during germband retraction, we investigate the mechanical coordination between cells that gives rise to collective cell migration.

Several features of germband retraction have been proposed to contribute to this collective cell migration, including active and passive roles for both the amnioserosa and the germband (Schöck & Perrimon, 2002). Together, these two tissues initially form interlocking

"U-shapes." As the germband retracts around the posterior end of the embryo to cover the ventral and lateral sides, the amnioserosa contracts to a final ellipse shape on the dorsal surface – preparing the embryo for dorsal closure (See Figure 4.1A and C). Several studies have found the amnioserosa plays a necessary role in germband retraction, offering mechanical assistance by pulling on the crook of the germband (Frank & Rushlow, 1996; H. E. Lynch et al., 2013). There is also evidence that the germband actively contributes to retraction by producing intracellular anisotropic stress along the axis of retraction (Holley E. Lynch et al., 2014). This stress anisotropy is thought to coordinate cell migration, suggesting that germband retraction is dependent on the specific allocation of stress among cells. Although the experimental evidence strongly points to the presence of anisotropic stresses in the two tissues (Lamka & Lipshitz, 1999; Holley E. Lynch et al., 2014), it remains unclear that germband retraction requires cell-autonomous creation of these stress fields. Holley E. Lynch et al. (2014) investigated these stress anisotropies using isolated patches of cells in a two-dimensional mechanical model. Their model approximates the effective mechanical stress from surrounding tissues with homogeneous boundary conditions along the patch edge, providing some insight into local stress anisotropies; however, they are unable to analyze the global interaction between the two tissues. Models of an earlier developmental event, ventral furrow formation, show that the egg's shape does influence cell migration (Allena et al., 2010; Allena et al., 2013; Conte et al., 2008). Here we introduce a novel two-and-a-half-dimensional (2.5D) cellular finite element model to probe the two-dimensional surface interactions between cells wrapped around a three-dimensional, ellipsoidal egg. This approach allows us to study the entire epithelium to test our hypothesis: During germband retraction, collective cell migration is robust to variations in the exact tensions along each type of cell-cell interface.

We test this hypothesis by varying the stress field and initial cellular geometry to determine how each play a role in germband retraction. First, we vary the distribution of tensile stress between cells in the amnioserosa and the germband. Germband retraction is found to proceed independent of these variations. Next, we vary the initial aspect ratio of amnioserosa cells. The extent of the germband's progress is contingent on the amnioserosa's initial cell geometry. With these findings, we present compelling evidence that cellular geometry controls the pathway to a germband retraction phenotype, predicting robustness to genetic and environmental perturbations.

4.2 Results

4.2.1 Construction of 2.5D cellular finite element model

To model the mechanical framework of germband retraction, we built a two-dimensional cellular finite element mesh wrapped onto a three-dimensional ellipsoidal last. The cell-level features of this 2.5D model are briefly outlined here. For more details, refer to the Online Methods and references: (G. W. Brodland, 2002; G. W. Brodland & Veldhuis, 2012; G. W. Brodland et al., 2007; H. E. Lynch et al., 2013). Each finite element represents a cell, with each vertex given a sliding constraint to the surface of the ellipsoidal last. Cell-cell interfacial edges carry a constant active tension. This tension represents the combined stress of microfilament bundles as well as the tangential equivalent of adhesion from adhesion junctions (G. Brodland et al., 2006; G. W. Brodland, 2002). *In vivo*, the actin cytoskeleton is localized cortically in both the amnioserosa and germband cells, providing a rationale for modeling tension along interfacial edges. (Schöck and Perrimon (2002) and the present study, data not shown). Assuming low Reynolds number conditions (Purcell, 1977), viscosity is implemented within each cell as two

orthogonal networks of dashpots. This dashpot network provides each cell with in-plane viscous damping in both directions as it shifts around the last, accounting for the viscous cytoplasm and the cytoskeletal network (G. Brodland et al., 2006; G. W. Brodland & Veldhuis, 2012). Cell area is also constrained, representing the incompressibility of the cytoplasm and the in-plane isotropic internal stress of the cortical cytoskeleton (G. Brodland et al., 2006). These constraints exert forces on each cell in the mesh. The finite element engine incrementally displaces each vertex according to the local imbalance of forces according to Eq. 3-3. The set of these vertex displacements result in cell deformation.

Alternatively, each time step taken by the finite element solver can be considered an energy minimization step. Surface energy may be defined along each cell-cell edge as the product of the edge tension ($\gamma_{c_1 c_2}$), determined by the two adjacent cell types $c_1$and c_2, and the length of the edge (L),

$$E = \sum_{All\ Edges} \gamma_{c_1 c_2} L \qquad \text{Eq. 4-1}$$

The finite element engine runs a simulation, maintaining a constant active tension on each cell-cell edge, until the mesh reaches a minimum energy configuration. This minimum energy is defined to occur when the relative change in energy between successive unit time steps, (1/E)(dE/dt), is first less than 0.1% . Considering the minimization of surface energy, we are provided two parameters that we can use to adjust the kinematics of our model: the edge tension defined by its two adjacent cell types, and the initial geometry of the mesh.

4.2.2 Base model approximates in vivo germband retraction

The mesh is composed of three cell types as shown in Figure 4.1C: germband (GB, cyan), amnioserosa (AS, yellow), and head (Hd, magenta) cells. The initial geometry of the cells are chosen to match the *in vivo* metrics described below, and they are deformed by constant, active tensions. These three cell types provide six cell-cell edge types for which we define the edge tensions, $\gamma_{c_1 c_2}$, of the model. The values of these tensions are detailed in Figure 4.2A and Appendix B. Three of these edge tension types are of particular interest to our study: γ_{GBGB}, γ_{GBAS}, and γ_{ASAS}. For our base model, we choose the heterotypic edge tension, γ_{GBAS}, to be assigned double the tension of the two homotypic cell-cell edges. The main reason for this choice is that *in vivo* imaging shows that the germband-amnioserosa boundary remains taut (Schöck and Perrimon (2002) and present study), and doubling this tension will maintain a smooth border. Additionally, head tensions γ_{HdHd} and γ_{HdAS} are increased to maintain a stiff head that resists movement around the anterior pole, which is consistent with *in vivo* imaging data (see Appendix B). The result of this first simulation is shown in Figure 4.1C. Surprisingly, without significant consideration of the particular choice of parameters, the model creates a reasonable approximation of germband retraction morphology (compare to Figure 4.1A). We use three metrics to quantitatively compare our base model to *in vivo* dynamics:

First, progression of germband retraction is traced by the position of the telson, which is the dorsal-most point of attachment between the dorsal bridge of the U-shaped amnioserosa and the tail end of the germband. The telson is marked by the green arrowhead in Figure 4.1A, and translates posteriorly as germband retraction proceeds. Additionally, the position of the archicephalon is marked by a magenta arrowhead, denoting where the head and amnioserosa meet on the dorsal surface. The telson progresses posteriorly as it moves away from the

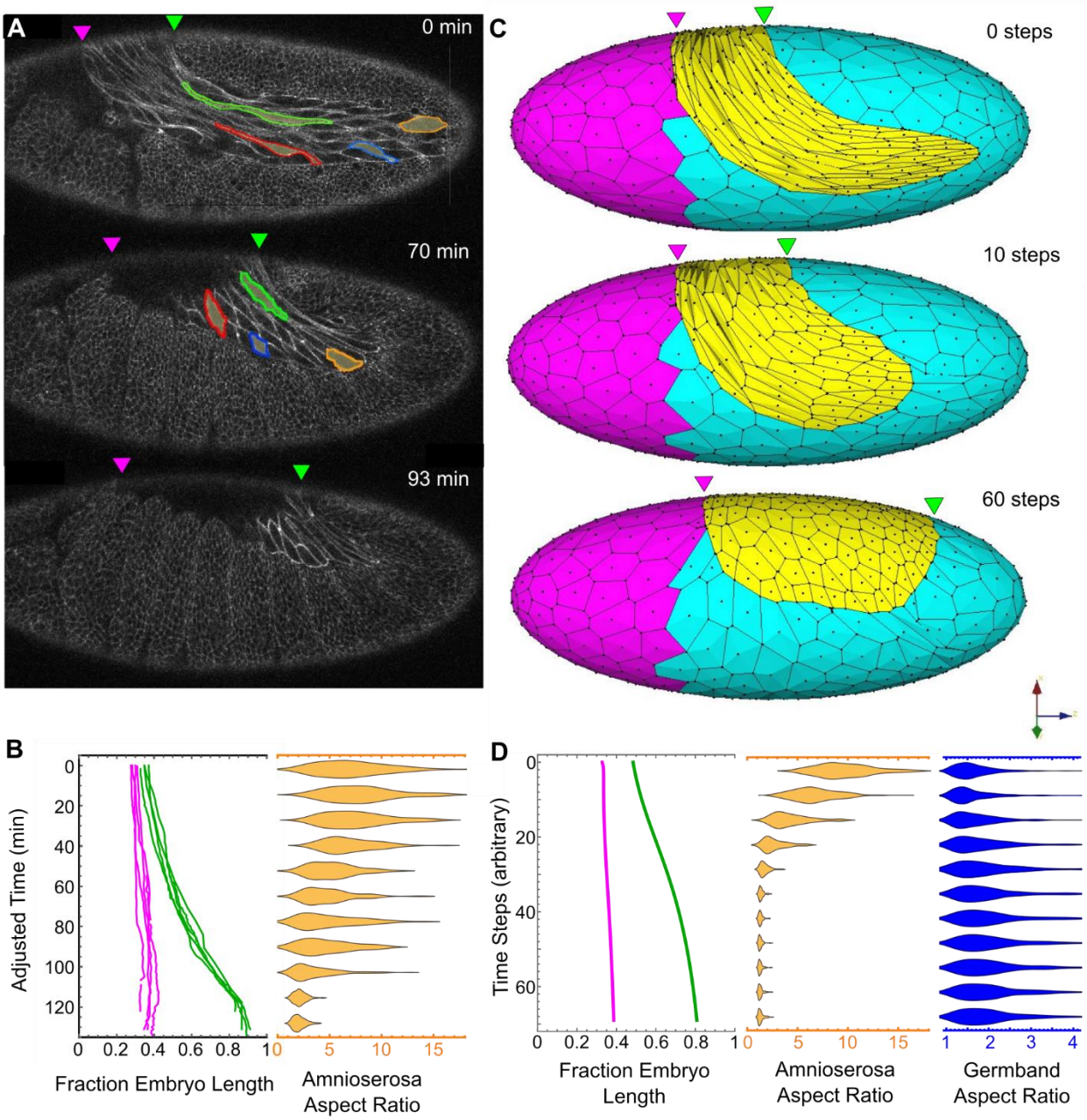

Figure 4.1: Base model replicates *in vivo* germband retraction. (**A**, **B**) *in vivo*. (**A**) Time-lapse images of germband retraction. (**B**) Kinematic analysis of germband retraction. Telson (green) and archicephalon (magenta) positions are traced from five embryos using data previously published in Tomer, Khairy, Amat, and Keller (2012)(n=3; supplemental videos 2, 3, 5), Truong, Supatto, Koos, Choi, and Fraser (2011) (n=1, supplemental video 4), and the embryo shown in (**A**) (n=1). Embryo fraction: 0.0, anterior; 1.0, posterior. Adjusted time (min) accounts for differences in developmental timing due to embryonic and experimental variations. Time for the embryo in Truong et al. (2011) was scaled by a factor of 1.68; for the embryo shown in (**A**), a factor of 0.79. Amnioserosa cell aspect ratios collected and binned in 12 min intervals (n= 49-

104 cells per time bin from 4 embryos). (**C**, **D**) Base model using $\gamma_{GBGB}{:}\,\gamma_{GBAS}{:}\,\gamma_{ASAS} = 10{:}\,20{:}\,10$. (**C**) Selected time steps of base model retraction. (**D**) Kinematics of base model shown in (**C**). Bar charts of aspect ratios do not bin time steps, but rather sample at the indicated time step. In this and subsequent figures: anterior, left; dorsal, up *in vivo* and positive x-axis according to coordinate axes; archicephalon position, magenta pentagon; telson position, green three-pointed star.

archicephalon. Figure 4.1B and D (*in vivo* and *in silico*, respectively) trace the telson and archicephalon positions through time as a fraction of embryo length. In both cases as the germband retracts, the telson progresses toward the posterior until it has reached roughly 85% of the length of the embryo.

Second, germband retraction is accompanied by amnioserosa cell contraction. Initially, the aspect ratio of amnioserosa cells span lengths 2 to 20 times their width (n= 49-104 cells per time bin from 4 embryos) with a median aspect ratio, $\widetilde{AR}$ = 7 *in vivo*, and a $\widetilde{AR}$ = 9.5 *in silico*. Cells highlighted in Figure 4.1A are typical in the amnioserosa in early germband retraction, bulging around their nucleus and often extending long, protruding arms between neighboring cells in the tissue sheet. Since cells in the amnioserosa do not exchange neighbors, distant cells use these protrusions to maintain connectivity. During germband retraction, the amnioserosa tissue contracts from a U-shape into a dorsally-centered ellipse. Correspondingly, the amnioserosa cells contract, decreasing their aspect ratios as germband retraction proceeds (highlighted cells in Figure 4.1A). The yellow bar chart in Figure 4.1B plots the distribution of aspect ratios (50-100 amnioserosa cells from four embryos tracked at about 12-min intervals). These distributions follow the same time scale presented in the telson position plot to the left. By the end of germband retraction, the cells round up significantly to sit on the dorsal surface with a $\widetilde{AR}$ just below 2. The base model replicates both the morphological change of the amnioserosa

tissue and the corresponding cell shape changes (Figure 4.1C). Amnioserosa cells in the base model also reduce their distribution of aspect ratios to a similar $\widetilde{AR} < 2$ (Figure 4.1D).

Third, germband retraction is also accompanied by a slight elongation of germband cells. The aspect ratio of the germband cells is reported to initialize *in vivo* at a mean value of 1.57 ± 0.06 and increase to a mean aspect ratio to 1.72 ± 0.18 (N=200-500 cells from 2 segments in each of 5 embryos with 20–50 cells per segment; Holley E. Lynch et al. (2014)). Cell intercalation does not occur during germband retraction (Schöck & Perrimon, 2002), so our model does not permit neighbor exchange. Additionally, germband and head cells are approximately 10 times larger in the model to speed simulation run times, i.e. 1 modeled cell to 10 *in vivo* cells. *In silico*, we initialize germband cells at a $\widetilde{AR}$ = 1.6. Figure 4.1D shows a plot of germband cell aspect ratios in blue, which increases through time to a $\widetilde{AR}$ = 1.9.

There are differences in the kinematics of this base model compared to *in vivo* data, i.e. the rate of telson displacement does not display an acceleration; however, it is evident that the progression and morphological change of germband retraction is similar. We now adjust this base model to investigate which parameters are necessary to drive retraction. This investigation considers the dependence on certain edge tension ratios and initial amnioserosa cell aspect ratios.

4.2.3 Germband retraction is robust to variation in cell-cell interfacial tension

We investigate how adjusting specific ratios of edge tensions between cell types disrupts germband retraction behavior. Figure 4.2A describes six tests that vary the tension ratios between the germband and the amnioserosa. The chart plots the resulting final archicephalon and telson positions compared to *in vivo* measurements (using data presented in Tomer et al. (2012), Truong et al. (2011), and the present study). Note that the base parameter set is indicated in bold.

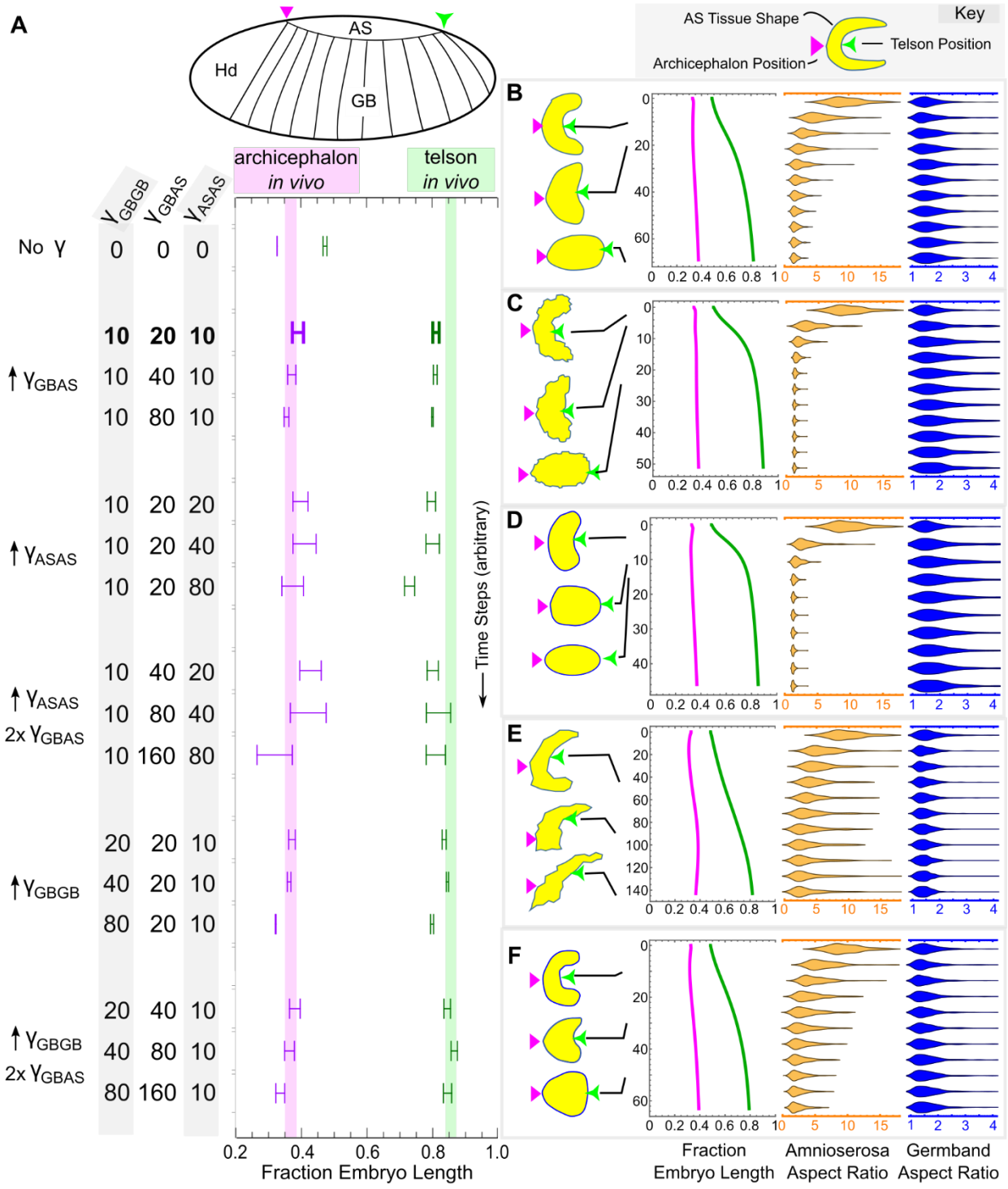

Figure 4.2: Germband retraction is robust to variation in cell-cell interfacial tension although kinematics vary. (**A**) Table of variations in tensions: γ_{GBGB}, γ_{GBAS}, and γ_{ASAS}. Chart shows final archicephalon and telson positions for *in vivo* data (magenta and green shaded bars, respectively) and individual model cases as a fraction of embryo length. Bars report standard error of mean for *in vivo* (n = 5 embryos) and model (n = 3 meshes). Base model is highlighted

in red. (**B-F**) Sketches of projected amnioserosa tissue at indicated time steps in the model (anterior, left). Charts show kinematics of 4-fold increases in tension as specified: (**B**) increased $\boldsymbol{\gamma_{GBAS}}$; (**C**) increased $\boldsymbol{\gamma_{ASAS}}$; (**D**) increased $\boldsymbol{\gamma_{ASAS}}$ with doubled $\boldsymbol{\gamma_{GBAS}}$; (**E**) increased $\boldsymbol{\gamma_{GBGB}}$; (**F**) increased $\boldsymbol{\gamma_{GBGB}}$ with doubled $\boldsymbol{\gamma_{GBAS}}$. Key shows initial amnioserosa tissue shape for all models.

With the single exception of the no tension case, every tension ratio allows germband retraction to proceed. The no tension case remains stationary or frozen, and thus serves as an initial geometry reference. The ability for each mesh to retract despite the differences in edge tension ratios suggests that in general the process of germband retraction is robust to tension differentials between tissues.

4.2.4 Ramped amnioserosa-amnioserosa interfacial tension is required to match in vivo kinematics

Although all of the tension ratios reach a final telson position that is similar to *in vivo* measurements, the manner in which germband retraction proceeds is not uniform. Figure 4.2B-F sketch the amnioserosa tissue shape change, archicephalon and telson positions, as well as the amnioserosa and germband aspect ratios through time for five of the edge tension ratio types. The graphs shown depict the results of parameters with 4-fold increases. All simulations use the same initial geometry as the base mesh, which is sketched in the Key in Figure 4.2B. Increasing γ_{GBAS} (Figure 4.2B) and γ_{ASAS} (Figure 4.2C) both demonstrate a "biphasic" rate of telson displacement.

In the initial phase, the increased tension quickly minimizes the length of the germband-amnioserosa border or the aspect ratio of the amnioserosa cells, respectively. These both move the telson significantly toward the posterior of the embryo, and induce strain in germband cells. The second phase consists of residual contractions of elongated cells until a minimum energy is reached, which corresponds to a slow rate of telson displacement. When γ_{GBAS} doubles an

increased γ_{ASAS} (Figure 4.2D), the kinematics remain similar to Figure 4.2C with the exception that the germband-amnioserosa border remains taut. Increasing γ_{GBGB} (Figure 4.2E) presents a nearly constant rate of telson displacement. In this case, stiff, isodiametric germband cells resist stress from the amnioserosa cells, and the rate of strain in the amnioserosa cells is more linear. Curiously, germband stiffness leads to a chiral instability, resulting in torsion of the embryo posterior and a lateral skew of the telson position. When γ_{GBAS} doubles an increased γ_{GBGB} (Figure 4.2E), the taut germband-amnioserosa border stabilizes the last and the telson remains on the dorsal midline, avoiding torsion. Despite these various parameter choices, it is clear that no distribution of constant active tensions along the cell-cell edges is capable of reproducing the accelerated rate of displacement shown *in vivo* (Figure 4.1B).

In an effort to match the kinematics of *in vivo* development, we also investigate the effects of three special cases in distributions of tension: polarized tension, increased cell density, and ramped tension. Each of these three cases applies tension differently to the last, and expands a simplifying assumption of our model. One assumption is that we only test isotropic tensions along a cell's edges. *In vivo*, germband cells produce intracellular anisotropic stress that is strongest along the axis of retraction (Holley E. Lynch et al., 2014). Figure 4.3A shows the kinematics of adding polarization parallel to the germband-amnioserosa border (see Appendix C for details). Compared to the base model in Figure 4.1D, polarization only serves to exaggerate the "biphasic" behavior in the rate of telson displacement. Next, our model assumes that germband cells can be scaled 10 *in vivo* cells to 1 modeled cell. Increasing the number of cells in the germband, increases the energy density of the tissue. To account for this 10-fold increase in cell density, we scaled γ_{GBGB} by roughly the square root of 10. Figure 4.3B shows the kinematics

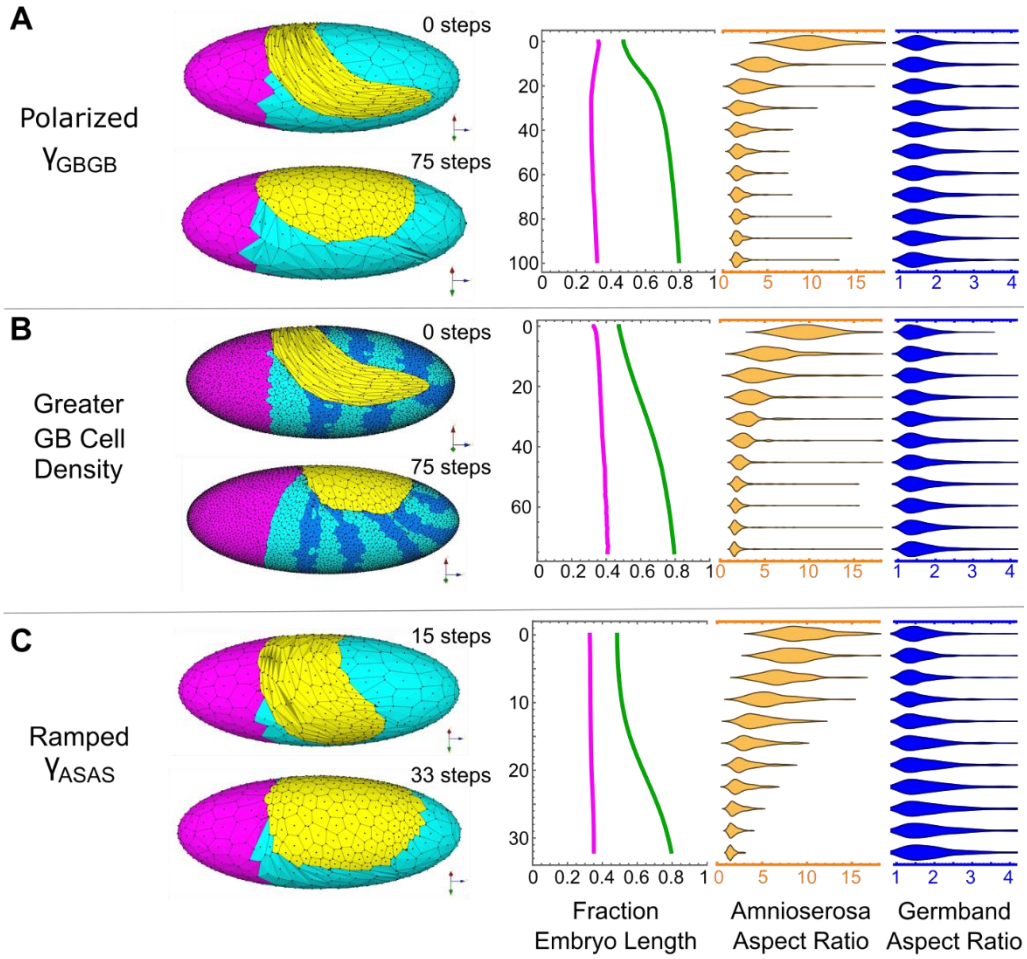

Figure 4.3: Ramped amnioserosa tension replicates *in vivo* kinematics but polarized tissue stress and increased cell density do not. (**A-C**) Mesh and kinematics for each of the following special parameters: (**A**) base mesh with 80% polarization in $\boldsymbol{\gamma_{GBGB}}$ parallel to germband-amnioserosa border; (**B**) base mesh with 10-fold increase in germband cell density, $\boldsymbol{\gamma_{GBGB}}:\boldsymbol{\gamma_{GBAS}}:\boldsymbol{\gamma_{ASAS}} = \mathbf{2}:\mathbf{12}:\mathbf{10}$; (**C**) base mesh with ramped $\boldsymbol{\gamma_{ASAS}}$. See Section 7.2.5C.1 and Appendix B for details on implementation of tensions.

for a denser mesh matches the base model very closely. This validates the reduced mesh but does not account for the *in vivo* kinematics. Finally, we assume cell-cell edge tensions remain constant throughout germband retraction. *In vivo*, amnioserosa cells have been shown to exhibit pulsatile contractions at the end of germband retraction as they transition into the following stage of dorsal closure (Sonia Muliyil, Krishnakumar, & Narasimha, 2011; Sokolow, Toyama, Kiehart, &

Edwards, 2012; Toyama, Peralta, Wells, Kiehart, & Edwards, 2008). Such contractions on average would likely serve to increase the tension among amnioserosa cell edges as germband retraction proceeds. We model this by ramping γ_{ASAS}, such that initially γ_{GBGB} dominates, but γ_{ASAS} becomes greater as germband retraction progresses. (See Figure 4.3C and Appendix B.) With this ramp in tensions applied between amnioserosa cells, the telson position accelerates. Although the pulsed contractions are not likely to provide a uniformly increasing tension, the uniform ramp is sufficient to provide a convincing best match to the *in vivo* data presented in Figure 4.1B. Notably, the germband fully retracts despite the tuned kinematics in all tension parameter cases, including these three special cases. Thus, germband retraction is robust to variations in tensions, suggesting the developing embryo is robust to perturbations in tension-producing mechanisms.

4.2.5 Germband retraction is dependent on cellular topology

Since germband retraction is robust to allocation of tissue-specific tension, we consider the effect of cell topology. To test cell topology, meshes are created with four different median aspect ratios in amnioserosa cells: 9.5, 7.0, 3.6, and 1.3 (Figure 4.1C and Figure 4.4). In each case, the amnioserosa cells completely contract to a final $\widetilde{AR}$ close to 1. In the case where the initial aspect ratio is 1 (Figure 4.4C), there is no change in the aspect ratio of the amnioserosa cells. Each case shows a correlation between the extent of movement of the telson position and the initial median aspect ratio of the amnioserosa cells. Once the amnioserosa cells reach a minimum aspect ratio, the mesh reaches an energy minimum and the process of retraction stalls. In other words, germband retraction is limited by the amnioserosa cells' ability to contract.

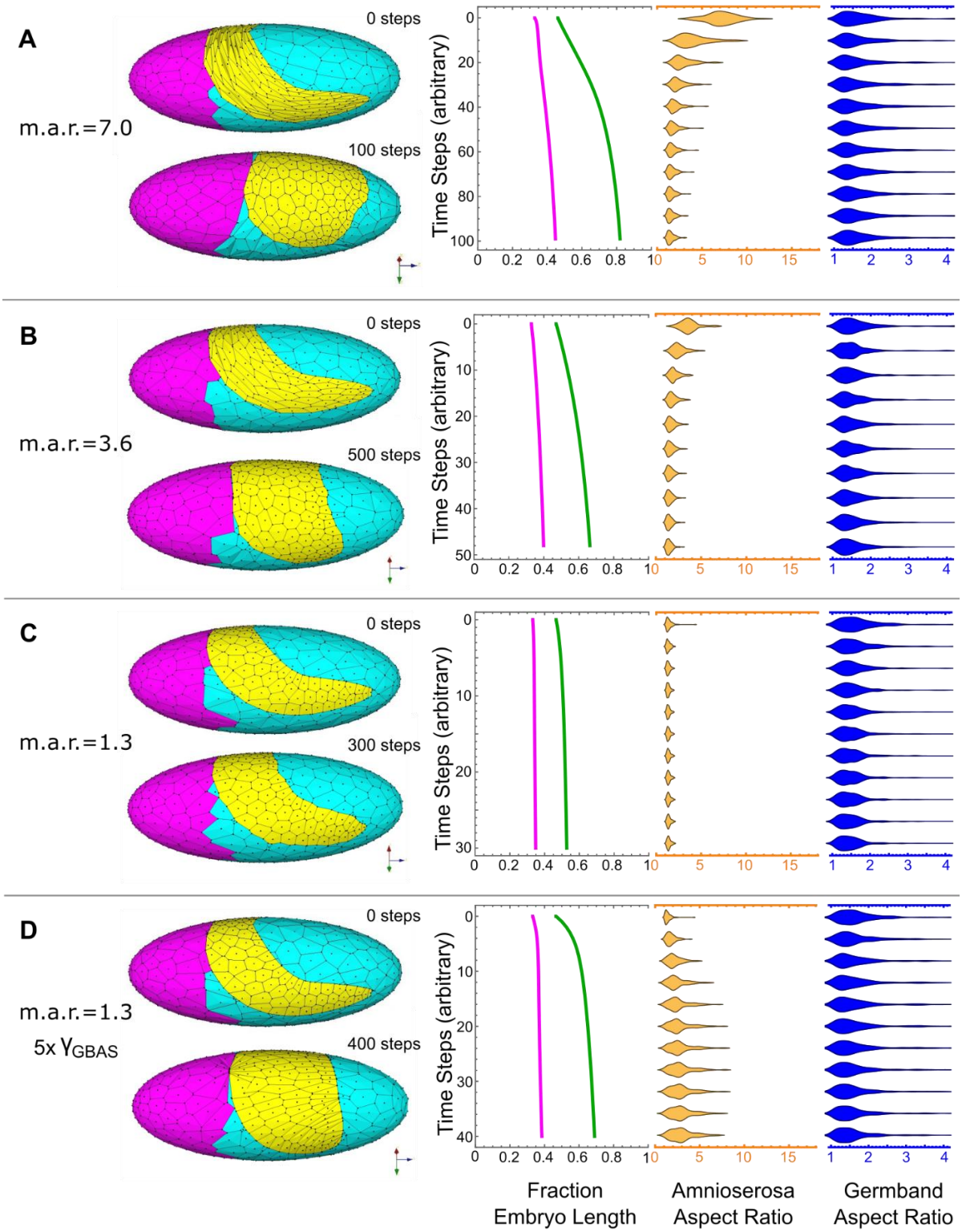

Figure 4.4: Initial cell geometry determines extent of germband retraction. (**A-C**) Mesh and kinematics for initial amnioserosa geometry tests with median aspect ratios ($\widetilde{AR}$): 7.0 (**A**), 3.6 (**B**), 1.3 (**C**). (**D**) Mesh and kinematics for a partial rescue of mesh in (**C**) using tension distribution $\gamma_{GBGB}{:}\,\gamma_{GBAS}{:}\,\gamma_{ASAS} = 10{:}\,100{:}\,10$.

This scenario, poses an interesting situation: despite fully contracting the amnioserosa cells, the amnioserosa tissue remains elongated. Could an elongated amnioserosa tissue with a strong border tension be sufficient to rescue stalled germband retraction? To answer this role for the amnioserosa tissue, we use the mesh with an amnioserosa cell $\widetilde{AR}$ = 1.3 and increase γ_{GBAS} to be 10 times greater than either γ_{ASAS} or γ_{GBAS}. Figure 4.4D shows that increasing this border tension is capable of only partially rescuing germband retraction. Amnioserosa cells grow towards the retracting germband to a $\widetilde{AR}$ = 3, stalling germband retraction. Thus, although tension along the amnioserosa border may assist in germband retraction, these results suggest that the elongated topology of the amnioserosa cells provide the energy necessary to drive germband retraction.

Taken together, it is apparent that proper germband retraction is dependent on the initial geometry of the amnioserosa cells. This geometry is established in the previous developmental stage, germband extension. Although the model does not explicitly simulate germband extension, the result of altering the initial amnioserosa cell aspect ratios predicts that a failure of the embryo to fully elongate cells during germband extension will lead to a failure in germband retraction. Thus, the dependence of germband retraction on the successful completion of previous morphological events implies the progression of embryogenesis is mechanically contingent.

4.3 Discussion

The 2.5D cellular finite element model of epithelial mechanics presented here allows embryogenesis to be studied as a complete, well-connected cell sheet. This cell sheet is wrapped around an ellipsoidal last, which approximates the shape of the developing embryo's epithelial tissues. This model differs from previous finite element models of embryogenesis by defining

each finite element as a cell and capturing the ellipsoidal boundary condition implicitly, permitting a cell-level analysis of whole-embryo tissue interactions (Allena et al., 2010; Allena et al., 2013; Conte et al., 2008; H. E. Lynch et al., 2013). Using this last, we have built a model of germband retraction, a stage midway through the development of the *Drosophila melanogaster* embryo that is characterized by embryo-wide collective cell migration. Through testing various conditions of cellular geometry and stress distribution, our model explains that germband retraction is dependent on initial cell geometry and predicts robustness to perturbations in stress.

The initial tissue morphology of the amnioserosa is the single factor that controls the extent to which the germband will retract. When amnioserosa cells are initialized to be more isodiametric, germband retraction stalls - showing a direct correlation between amnioserosa cell strain and the extent of telson displacement. The dependence of germband retraction on initial amnioserosa cell shape, established during germband extension, can be understood in terms of the surface energy defined in Eq. 4-1. Since energy scales with the length of a cell-cell edge, the long amnioserosa cell edges carry large amounts of energy. As the system minimizes this energy, the stress along these edges affects strain in the tissue, pulling the germband through retraction. It should be clarified that germband retraction is not the reversal of germband extension. During germband extension, germband cells intercalate as the germband extends, but no intercalation is observed during germband retraction (Schöck & Perrimon, 2002). Although amnioserosa cells do actively elongate by microtubule extension and differential adhesion, this process occurs over the course of hours (Goldenberg & Harris, 2013; Pope & Harris, 2008). On this time scale the stresses driving elongation dissipate prior to germband retraction, meaning amnioserosa cells are not storing elastic potential energy (Mao & Baum, 2015). Although they do not store energy,

these highly-elongated cells do preserve information for guiding collective cell migration. Thus, by having morphogenesis depend on cellular geometry, cell migration in the embryo is mechanically robust.

Mechanical robustness is evidenced by the ability of germband retraction to proceed under various stress conditions. Retraction, as measured by telson position, completed for every ratio of tensions applied to the various types of cell-cell interfaces, provided some tension existed along every cell edge. This result predicts that germband retraction is robust to genetic or environmental perturbations in force-producing proteins. Examples of mutations that specifically maintain completion of germband retraction may be difficult to find, but dorsal closure mutations may be of interest. Several mutations alter the expression and activation of key force-producing and force-transmitting proteins, such as myosin II, actin, and adhesion junctions. Rho GTPase, Diaphanous, and Girdin mutants are all reported to complete germband retraction despite failing dorsal closure (Bloor & Kiehart, 2002; Homem & Peifer, 2008; Houssin, Tepass, & Laprise, 2015; Schöck & Perrimon, 2002). Although these reports do not directly measure whether mutant cell-cell interfacial tensions vary from wild-type, the model's results provide compelling evidence that *Drosophila melanogaster* has evolved a robust mechanism to ensure proper development at least in this stage of embryogenesis.

There are several mutations and physical injuries that can cause germband retraction to fail. In the next chapter we describe a series of experiments that investigates a special case of germband retraction failure resulting from exposure to a heat shock. This non-invasive perturbation produces holes in the amnioserosa. We experimentally test the post-heat shock conditions that produce these holes. Then in Chapter 6 we use the model to investigate the mechanical ramifications of an incoherent epithelium that leads to germband retraction failure.

CHAPTER 5

PATHWAY TO A PHENOCOPY: HEAT STRESS EFFECTS IN EARLY EMBRYOGENESIS

Authors of Manuscript
Sarah M. Crews, W. Tyler McCleery, and M. Shane Hutson

This chapter has been published as S.M. Crews, W.T. McCleery and M.S. Hutson (2015) "Pathway to a Phenocopy: Heat Stress Effects in Early Embryogenesis" *Developmental Dynamics* 245: 402-413 https://doi.org/10.1002/dvdy.24360. Authors Crews and McCleery were designated as contributing equally to this work. This chapter presents experimental investigations of a developing *Drosophila* embryo after early heat shock stress. This environmental stress proves to induce holes in the amnioserosa tissue, providing a means to test a perturbed epithelium *in vivo*. The results from these experiments will be analyzed by the 2.5-D cellular finite element model in Chapter 6.

Abstract: *Background:* Heat shocks applied at the onset of gastrulation in early *Drosophila* embryos frequently lead to phenocopies of U-shaped mutants – having characteristic failures in the late morphogenetic processes of germband retraction and dorsal closure. The pathway from non-specific heat stress to phenocopied abnormalities is unknown. *Results: Drosophila* embryos subjected to 30-min, 38-°C heat shocks at gastrulation appear to recover and restart morphogenesis. Post-heat-shock development appears normal, albeit slower, until a large fraction of embryos develop amnioserosa holes (diameters > 100 μm). These holes are positively correlated with terminal U-shaped phenocopies. They initiate between amnioserosa cells and

open over tens of minutes by evading normal wound healing responses. They are not caused by tissue-wide increases in mechanical stress or decreases in cell-cell adhesion, but instead appear to initiate from isolated apoptosis of amnioserosa cells. *Conclusions:* The pathway from heat shock to U-shaped phenocopies involves the opening of one or more large holes in the amnioserosa that compromise its structural integrity and lead to failures in morphogenetic processes that rely on amnioserosa-generated tensile forces. The proposed mechanism by which heat shock leads to hole initiation and expansion is heterochonicity – i.e., disruption of morphogenetic coordination between embryonic and extra-embryonic cell types.

5.1 Introduction

Non-specific environmental stress is known to cause developmental defects in embryogenesis. For example, maternal consumption of alcohol during mammalian pregnancy leads to developmental delays, growth deficiency in the fetus, and a characteristic spectrum of abnormalities – widely recognized as fetal alcohol spectrum disorder (Clarke & Gibbard, 2003; Delpisheh et al., 2008; Ornoy & Ergaz, 2010). Similarly, hyperthermia or heat shock during vertebrate development has been associated with defects of the central nervous system, including neural tube defects (M. J. Edwards, 1998; Kofink, Boks, Timmers, & Kas, 2013; Moretti, Bar-Oz, Fried, & Koren, 2005; Pai et al., 2012). Similar effects have been described in detail for the model system of *Drosophila melanogaster* in which the developmental defects have been termed phenocopies – so named for their ability to mimic the phenotypes of specific genetic mutations (Peterson & Mitchell, 1991). In general, the severity and characteristic spectrum of defects is strongly dependent on the developmental stage at which an environmental insult occurs. This stage dependence appears in *Drosophila* embryogenesis as two classes of environmentally-

induced phenocopies (Eberlein, 1986), differing in whether stress occurs during or after cell fate commitment. The former can obviously interfere with cell fate specification, and have in some instances been traced back to the misregulation of single pair rule genes that control segmentation during specific developmental windows (Dura & Santamaria, 1983; Santamaria, 1979; Welte, Duncan, & Lindquist, 1995). The latter have not yet yielded to the same sort of molecular-level explanation. This is largely because these defects occur in the less-well-studied process of how committed cells drive morphogenesis through cell- and tissue-level biomechanics. Here, we investigate heat shocks applied at the onset of gastrulation that lead to defects in the much later morphogenetic process of germband retraction – phenocopying one of several U-shaped mutants (Frank & Rushlow, 1996; GoldmanLevi, Miller, Greenberg, Gabai, & Zak, 1996; Lamka & Lipshitz, 1999). We trace the pathway that funnels non-specific stress to the altered behavior of a single cell type to disruptions in tissue mechanics and finally to failures in specific morphogenetic processes.

The processes of interest in *Drosophila* embryogenesis involve two simple monolayer epithelia –amnioserosa and germband – that are adjacent on the embryonic surface and undergo coordinated morphogenesis. The tissues are specified by the start of gastrulation (Rusch & Levine, 1996) and occupy the dorsolateral surface over the posterior-most ¾ of the blastoderm (Foe, Odell, & Edgar, 1993). Presumptive amnioserosa cells cover the dorsal-most regions with germband cells adjacent laterally (Foe et al., 1993). The germband will also cover the ventral surface once the presumptive mesoderm invaginates during gastrulation (Rusch & Levine, 1996). Once gastrulation begins, germband cells start intercalating between one another in a convergent extension process that lengthens the germband in the anterior-posterior direction (Blankenship, Backovic, Sanny, Weitz, & Zallen, 2006; Irvine & Wieschaus, 1994; Lecuit & Lenne, 2007).

Since the cells are confined within a semi-rigid vitelline membrane, this extension causes the germband to curl around the posterior end of the embryo and onto the dorsal surface – making a U-shaped tissue when viewed laterally. The adjacent amnioserosa cells maintain attachment to the extending germband and become highly elongated to fill in the space between the arms of the U-shaped germband along both lateral flanks (Pope & Harris, 2008). The amnioserosa thus adopts its own U-shape when viewed dorsally. The tissue-level shape changes are then reversed in germband retraction, but this process is not the reverse of extension when viewed at the cellular level. Instead of being driven by intercalation and cell rearrangements, retraction is only accompanied by cell shape changes – a rounding up of amnioserosa cells and a modest dorsolateral extension of germband cells (Schöck & Perrimon, 2002). By the end of retraction, the amnioserosa again occupies the dorsal surface and the germband covers its ventrolateral aspects. Amnioserosa cells then begin apical constriction (M. S. Hutson et al., 2003; Kiehart, Galbraith, Edwards, Rickoll, & Montague, 2000), as well as stochastic apoptosis and extrusion (Sonia Muliyil et al., 2011; Toyama et al., 2008), to invaginate and pull the adjacent germband dorsally (Sokolow et al., 2012). When this process of dorsal closure is complete, the germband will cover the entire embryonic surface except the anterior-most cephalic regions, and the invaginated amnioserosa cells will undergo apoptosis (Abrams, White, Fessler, & Steller, 1993; Jacinto, Woolner, & Martin, 2002). This coordinated morphogenesis requires active participation by both epithelia, as measured by laser microsurgery experiments (Fernandez-Gonzalez, Simoes Sde, Roper, Eaton, & Zallen, 2009; M. S. Hutson et al., 2003; M. Shane Hutson et al., 2009; Kiehart et al., 2000; H. E. Lynch et al., 2013; Ma, Lynch, Scully, & Hutson, 2009; Peralta et al., 2007; Rauzi, Verant, Lecuit, & Lenne, 2008; Solon et al., 2009), and as clearly evidenced by

failure of germband retraction in mutants of the U-shaped group when the amnioserosa dies prematurely (Frank & Rushlow, 1996).

In light of these prior observations, our initial working hypothesis was that a heat shock applied at the onset of gastrulation leads to U-shaped phenocopies through a loss of amnioserosal mechanical integrity. Here, we show that our working hypothesis is correct and that the loss of structural integrity is due to large holes that open in the amnioserosa 4 to 9 hours after heat shock. These holes do not contain nuclei; they initiate along cell-cell interfaces and slowly, but relentlessly open until reaching diameters > 100 µm. We then synthesize our findings on heat-shock-induced changes in tissue mechanics, morphogenesis and cell behavior to propose and support a model in which heat shock disrupts the temporal coordination of amnioserosa and germband morphogenesis. This heterochronicity leads to premature cell death in the amnioserosa, accompanied by large holes that compromise its mechanical integrity, and ultimately to failures of germband retraction and dorsal closure.

5.2 Results

As a first step toward investigating the specific spectrum of heat-shock-induced developmental defects observed in *Drosophila* (Eberlein, 1986), we conducted live imaging of heat-shocked embryos. The heat shock was applied for 30 min at 38 °C, beginning just as the cephalic furrow formed at the onset of gastrulation. Embryos were then returned to room temperature and subsequent stages of embryonic development were imaged via confocal microscopy of live embryos expressing one of five fluorescent labels: E-Cadherin-GFP (Oda & Tsukita, 2001), moesin-GFP (K. A. Edwards et al., 1997; Kiehart et al., 2000), Gap43-mCherry,

Apoliner (Bardet et al., 2008), and two-color E-cadherin-GFP::sqh-mCherry. Sequential images of a heat-shocked E-cadherin-GFP embryo are shown in Figure 5.1A. Immediately after heat shock, the embryonic ectoderm exhibits an unusual morphology with subsets of cells elongating to form swirling clumps. Within a few hours, the cells revert to a normal morphology as the embryo appears to recover from heat shock and proceeds through the typical stages of development, albeit at a slower rate. Surprisingly, several hours after the shock (~7.5 hrs in the example shown in Figure 5.1A), the embryo's amnioserosa develops a hole. By nine hours after heat shock, the hole has grown to a diameter of 150 μm – the full mediolateral width of the amnioserosa. Similar holes were observed in all five tested strains. Although the amnioserosa is an extra-embryonic tissue, it plays key roles in the morphogenetic processes of germband extension (Goldenberg & Harris, 2013; Pope & Harris, 2008), germband retraction (H. E. Lynch et al., 2013; Reed, Wilk, Schock, & Lipshitz, 2004; Schöck & Perrimon, 2002), and dorsal closure (M. S. Hutson et al., 2003; Kiehart et al., 2000). The presence of holes in this tissue is a clear developmental anomaly and could quite readily lead to aberrant morphogenesis.

We thus quantified when, where and how often such holes appeared. As for where, all observed holes opened in the dorsal or dorso-lateral portion of the amnioserosa; no holes were observed along the amnioserosa's lateral flank (see Figure 5.1B). There were also no holes observed in the adjacent germband. As for when, the timelines in Figure 5.1C compare the developmental timing of heat-shocked and control embryos. Each timeline represents one embryo of the noted strain and shows both the developmental stage identified by tissue morphology – referred to as morphological stage – as well as the actual time elapsed since gastrulation, denoted as hours post-gastrulation (hpg). These embryos were imaged continuously starting at the time indicated by the first colored bar, and the initiation of holes are marked with

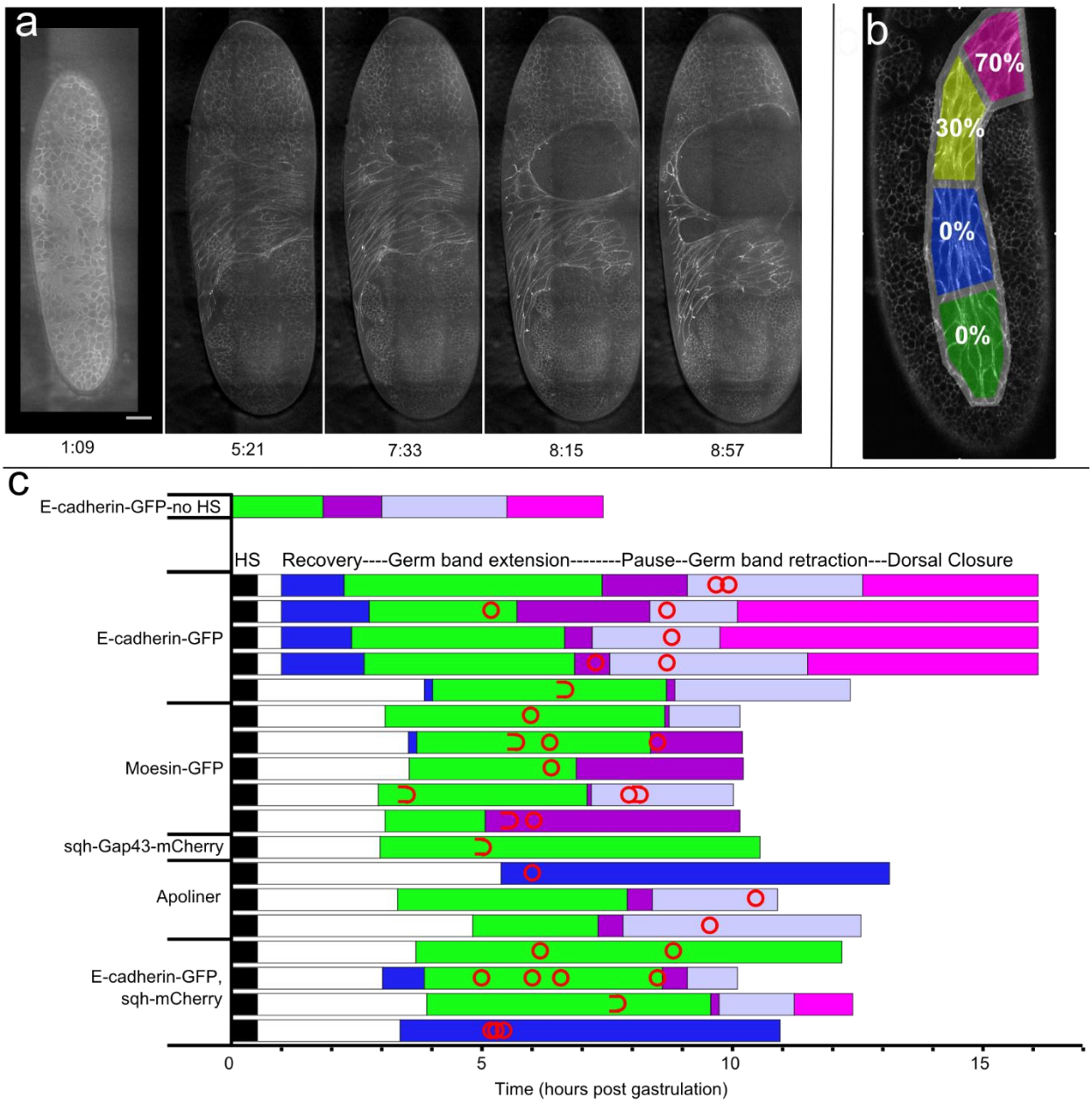

Figure 5.1: Heat-shock-induced holes in the amnioserosa. (**A**) Time-lapse images of a hole as it opens (dorsal views with anterior up). Times listed are hr:min after the start of heat shock; scale bar is 50 µm. The entire time-lapse image set is available as Supplemental Movie S1a. (**B**) Spatial distribution of holes (lateral view with anterior up; N = 16). (**C**) Timelines of morphogenetic progression for a control E-cadherin-GFP embryo maintained at 25 °C (top) and multiple other strains (as labeled at left) that were subjected to gastrulation-stage heat shocks (30 min at 38 °C). Color-coded timelines begin at the onset of gastrulation with the extended heat shock (black), a period of no imaging (white), and subsequent recovery and progression through morphological stages (colors as noted in legend above first heat-shocked E-cadherin-GFP timeline). Each timeline also marks the initiation of holes (full circles) and the earliest observation of holes that moved into the field of view (semi-circles).

red circles (or red semi-circles if the hole moved into view and its time of initiation must have been at some earlier time). Heat-shock-induced holes generally appeared between four and nine hpg, occurring when the embryo appears to be in the morphological stage of germband extension (Bownes stage 8 or 9) or germband retraction (Bownes stage 12). In many cases, multiple holes occurred in a single embryo. In fact, the example embryo shown in Figure 5.1A has a smaller hole below and to the left of the large hole.

As for how often, we observed holes in the amnioserosa for roughly half (18 of 33) of the continuously imaged, heat-shocked embryos; however, we also observed holes and other defects in some continuously imaged control embryos. The holes and defects in control E-cadherin-GFP embryos were only observed if continuous imaging began within 5.5 hpg, implying that holes can also open as a result of phototoxicity in early embryogenesis. To control for phototoxicity, we performed a second set of experiments in which heat-shocked embryos were only imaged at two time points: once at 7-8 hpg to assess the prevalence of amnioserosa holes; and a second time at approximately 20 hpg to score the embryos for developmental defects. These experiments were only conducted on E-cadherin-GFP and moesin-GFP embryos (N = 53 and 31), with amnioserosa holes respectively observed in 65% and 14% of embryos (Table 5-1). Since we only imaged the embryos at two time points and did not have a full view of the amnioserosa in any single embryo, the quoted prevalence values for holes are likely lower limits.

These embryos were also scored for five terminal abnormalities: head defects, segmentation defects, and failures of germband extension, germband retraction, or dorsal closure. Table 5-1 compares the prevalence of these defects in our experiments to values reported by Eberlein (1986). We observe similar rates of failure in germband retraction, but much higher prevalence for head and segmentation defects. The differences may result from our

use of different fly strains and a longer, but less intense heat shock (30 min at 38 °C versus 2.5 min at 43 °C). We also scored defects differently, using confocal imaging of live embryos instead of cuticle staining. Eberlein (1986) did not score cuticles for failures in germband extension nor dorsal closure. Such defects would likely have fallen into Eberlein's "Poor cuticle or holes" category, but this category was not scored following gastrulation-stage heat shocks – leaving us no comparison for our observations of 30-40% prevalence for dorsal closure failures. Note that cuticle "holes" are not necessarily the same as amnioserosa holes observed here. A hole in the cuticle could result from any type of failure for germband retraction or dorsal closure that prevented cuticle-depositing tissues from completely covering the dorsal surface. (Eberlein, 1986; Frank & Rushlow, 1996; Harden, Loh, Chia, & Lim, 1995; Roote & Zusman, 1995).

These holes observed in the amnioserosa are sufficiently common to then ask three pertinent questions: (1) how do the holes initiate? (2) why do they expand so far? and (3) are they part of the causal chain leading to characteristic heat-shock-induced developmental defects? We take on these three questions in reverse order.

	E-Cadherin-GFP		Moesin-GFP		Canton S (Eberlein, 1986)	
Defect	N	Prevalence	N	Prevalence	N	Prevalence
Hole in Amnioserosa	51	65%	28	14%	--	--a
Head Defect	46	61%	30	80%	249	23%
Segmentation Defect	24	17%	19	42%	249	1%
Failure GB Extension	49	8%	28	0%	--	--
Failure GB Retraction	44	32%	29	21%	249	20%
Failure Dorsal Closure	44	43%	29	31%	--	--

Table 5-1: Prevalence of developmental defects observed after gastrulation-stage heat shocks. The number of embryos scored for each defect category varies because not all embryos were scorable for every defect. Scorability depended on embryo orientation. GB = germband. a Dashes imply a category that was not scored in Eberlein (1986).

5.2.1 Do amnioserosa holes cause subsequent development defects?

The opening of holes in the amnioserosa is certainly the most conspicuous anomaly observed in post-heat-shock development, but it is not the only difference from controls. As shown in Figure 5.1C, heat-shock leads to a delay of several hours in subsequent morphological stage progression. This post-heat-shock delay begins with a 2- to 4-hour recovery period before germband extension commences and then proceeds at roughly half-normal rates. By the end of germband extension, heat-shocked embryos are 4- to 9- hours behind the normal pace of development. After this time, the heat-shocked embryos make up some time by nearly skipping the usual 2-hour pause between germband extension and retraction, which thus starts 2- to 7 hours late, but then proceeds at near normal rates.

A closer look at tissue morphology shows that heat-shocked embryos also undergo less germband extension. As shown in Figure 5.2A, the telson, i.e., the most caudal end of the germband, extends as far anteriorly as 37% of embryo length in control embryos, but only reaches 50% of embryo length following heat shock. To test whether this restricted extension was a direct consequence of developmental delay, we also tracked telson position in an embryo developing at a lower temperature, which uniformly slows morphogenesis. Even with its development slowed, this embryo's telson reaches 37% of embryo length, showing that the heat-shocked embryos are undergoing something beyond a uniform developmental delay.

In addition to differences in tissue morphology, heat shock clearly perturbs the morphology of individual cells. First, cells throughout the ectoderm are disfigured immediately after heat shock (Figure 5.1A). This swirling pattern is similar to that seen in arm mutants (Pope & Harris, 2008), in which the germband never extends as a tissue, but adjacent amnioserosa cells still autonomously elongate. The mismatch in morphogenesis constrains the elongating amnioserosa cells so that they form a swirling patch. The swirled pattern after heat shock is

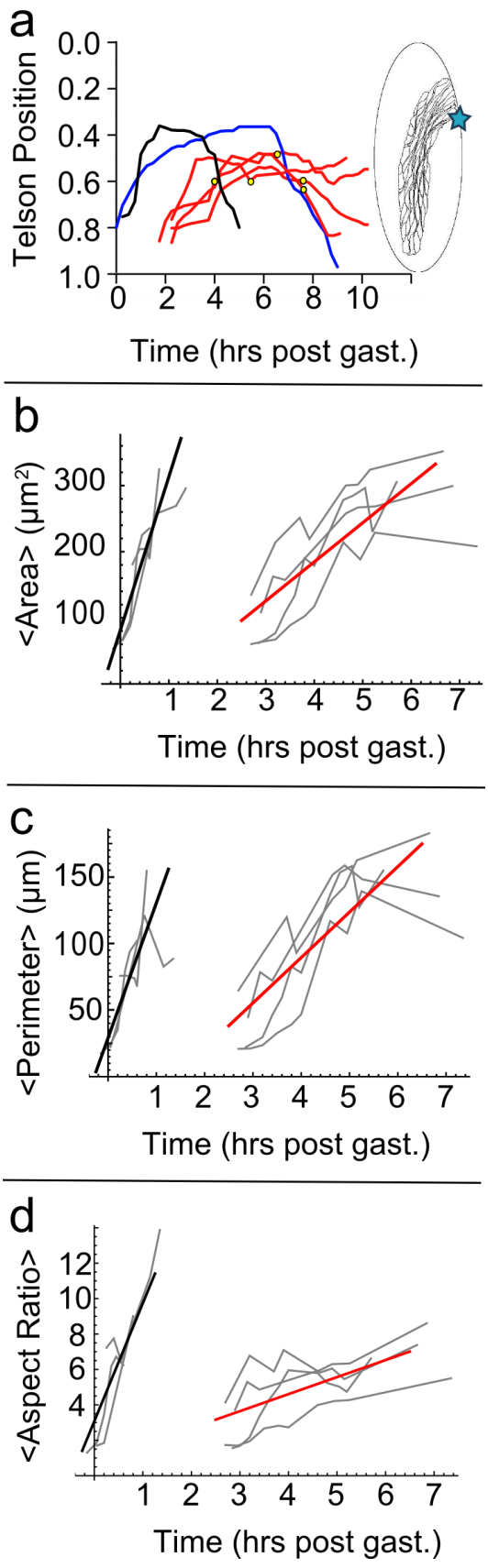

Figure 5.2: Dynamics of morphogenesis after heat shock. (**A**) Telson position (blue star on inset diagram) versus time from gastrulation through germband retraction. Position is reported as a fraction of embryo length (increasing from anterior to posterior). Each curve shows the telson moving anteriorly during germband extension and then back posteriorly during germband retraction: control embryo maintained at 25 °C (black line); heat-shocked embryos (red lines); and a non-shocked embryo whose development was slowed by lowering its temperature to 18-19 °C (blue line). Holes opened in the amnioserosa of heat-shocked embryos at the indicated times (yellow circles). (**B-D**) Morphological dynamics of amnioserosa cells as measured by mean area (**B**), mean perimeter (**C**), and mean aspect ratio (**D**). Curves for individual embryos (gray) are overlain with linear fits for control (black) and heat-shocked embryos (red). Dynamics in heat-shocked embryos (N = 4) are both slowed and delayed compared to controls (N = 3).

however transient. These cells recover normal morphology before beginning germband extension, but during extension, amnioserosa cells again diverge from normal morphology. As shown in Figure 5.2B-D, amnioserosa cells in heat-shocked embryos increase their area, perimeter and aspect ratio at rates that are respectively just 1/3, 1/4 and 1/7 as fast as controls. These differences in morphological rates for individual cells are greater than the 2-fold difference observed at the tissue level. Nonetheless, by the end of germband extension, individual amnioserosa cells in heat-shocked embryos reach final areas and perimeters that match those in control embryos. Their aspect ratios never do reach quite the same degree of elongation.

Heat shock thus causes differences in cell and tissue morphogenesis, the frequent opening of anomalous holes in the amnioserosa, and a spectrum of terminal phenotypes. To determine the impact of amnioserosa holes on subsequent development, we catalogued correlation tables for holes and terminal phenotypes as shown in Figure 5.3. These tables include only E-cadherin-GFP embryos. If an embryo was oriented such that it could not be scored for a given phenotype, that embryo was not included in the prevalence or correlation calculations. Using a Fisher's exact-test, we find that holes are positively and significantly correlated with three of our five scored abnormalities: head defects ($N = 46$, $p = 0.016$), failures of germband retraction ($N = 44$, $p = 0.015$), and failures of dorsal closure ($N = 44$, $p < 0.001$). For the latter two phenotypes, 17 of 19 embryos displaying one of the two defects also had holes at the earlier observation timepoint. Correlation is of course not causation, but previous work on the mechanics of both germband retraction and dorsal closure showed that the amnioserosa makes a critically important contribution to the forces driving those processes (M. S. Hutson et al., 2003; H. E. Lynch et al., 2013; Holley E. Lynch et al., 2014; Solon et al., 2009; Toyama et al., 2008; Wells et al., 2014).

		Head Defect		Seg. Defect		Failure GBE		Failure GBR		Failure DC	
		TRUE	FALSE	TRUE	FALSE	TRUE	FALSE	TRUE	FALSE	TRUE	FALSE
Hole in AS	TRUE	21	7	2	6	4	27	12	14	17	9
	FALSE	7	11	2	14	-	18	2	16	2	16
p-Values		0.016*		0.407		0.148		0.015*		<0.001*	

Figure 5.3: Heat-shock-induced holes are statistically correlated with specific developmental defects. Statistically significant correlations ($p < 0.05$) between holes and defects are denoted by an asterisk (*). See text for explanation of defects. AS = amnioserosa; Seg. = segmentation; GBE = germband extension; GBR = germband retraction; DC = dorsal closure.

These processes can fail if the amnioserosa's structural integrity is compromised via laser ablation (M. S. Hutson et al., 2003; H. E. Lynch et al., 2013) or mutations (Frank & Rushlow, 1996; Reed et al., 2004); heat-shock induced holes could do the same. The remaining correlation with head defects is puzzling. Although concurrent with dorsal closure, little is known about the amnioserosa's role in the mechanics of head involution (VanHook & Letsou, 2008).

5.2.2 Why do the holes expand so far?

When our imaging caught holes in the amnioserosa just as they opened, these holes were initially smaller than a single cell (< 5-µm diameter). Although many researchers have purposely created similar-sized holes in *Drosophila* embryos using laser ablation, these small laser-drilled holes typically open up less than 3x their initial size (Ma et al., 2009). What conditions cause heat-shock induced holes to open up to diameters on the order of 100 µm? The maximum extent of a hole in an elastic sheet depends on the ratio of tensile stress to tissue stiffness. Perhaps the tissue in this particular location and developmental stage is under much more tension or is much less stiff. Perhaps heat shock alters the tension or stiffness.

To test these possibilities, we conducted laser ablation experiments to measure the rate and extent at which laser-drilled holes opened in the amnioserosa during germband extension and retraction (Bownes stages 8 and 12 respectively). For a viscoelastic sheet, the initial hole-opening strain rate should be proportional to the ratio of tensile stress to effective viscosity; and the maximum radial strain at the hole margin should be proportional to the ratio of tensile stress to stiffness (Ma et al., 2009). We estimated these quantities by collecting post-ablation confocal images of the targeted cells and mapping the local deformation fields. As shown in Figure 5.4C, the initial strain rates and maximum radial strains in control embryos do not depend significantly on developmental stage (8D versus 12D) or sub-region within the amnioserosa (12D versus 12L). In all three cases, the strain rates in the first five seconds after ablation were ~ 0.02 s^{-1}, which corresponds to recoil velocities of 0.1-0.2 μm/s. These strain rates and velocities are on

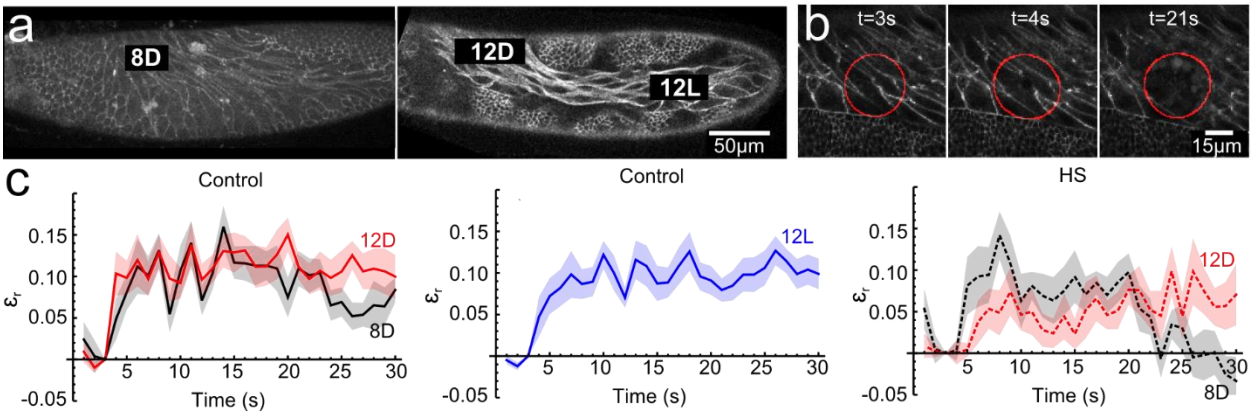

Figure 5.4: Stage, location, and heat-shock dependence of amnioserosa tissue mechanics. (**A**) Confocal images of E-cadherin-GFP embryos noting the amnioserosa locations (D, dorsal; L, lateral) and developmental stages (Bownes stage 8, germband extension; 12, germband retraction) that were probed by laser hole drilling. (**B**) Time-lapse images of an example hole-drilling experiment. Times noted are seconds after laser ablation. The entire time-lapse image set is available as Supplemental Movie S2. Post-ablation radial strain was calculated by applying measured deformation fields to a circle initially centered on the targeted point (red circle). (**C**) Radial strain versus time for laser-drilled holes at the noted amnioserosa locations and stages in control (left, N8D = 9, N12D = 11; and center, N12L = 11) or heat-shocked embryos (right, N8D-HS = 12; N12D-HS = 8). Shaded areas represent standard error of the mean.

the low end of previous measurements in fly embryos (Farhadifar, Röper, Aigouy, Eaton, & Jülicher, 2007; M. S. Hutson et al., 2003; Kumar et al., 2006; Peralta et al., 2007; Rauzi et al., 2008; Toyama et al., 2008) – certainly below the recoil velocities of 1-3 μm/s typically seen over the first few seconds after ablation of amnioserosa cells later in embryogenesis during dorsal closure (M. S. Hutson et al., 2003; Ma et al., 2009; Peralta et al., 2007; Toyama et al., 2008), but comparable to those observed in the extending germband itself (Fernandez-Gonzalez et al., 2009; Rauzi et al., 2008). The maximum radial strain is also quite small at just 0.10-0.15, which corresponds to our 8-μm test circle expanding out to an effective radius of just 9 μm. Assuming that these cells are not dramatically more viscous than others in *Drosophila* embryos, the laser-ablation results suggest that for control embryos as least, there is a small tension in the amnioserosa at these developmental stages. There is certainly no marked increase in tension for the dorso-lateral region or for stage 12 versus 8.

We then made similar measurements in embryos subjected to a gastrulation-stage heat shock, with measurements made in the dorso-lateral region of the amnioserosa at matched morphological stages. As shown in the rightmost panel of Figure 5.4C, the initial strain rates and maximum radial strains were less than or equal to those of control embryos – implying equal or less tensile stress and equal or greater stiffness in the heat-shocked tissues. This evidence shows that there is not increased mechanical stress nor decreased stiffness in the heat-shocked tissues. The explanation for why heat-shock-induced holes open to such large extents must rely on properties beyond passive mechanics.

Interestingly, heat-shock-induced holes open very differently than holes made in heat-shocked embryos using laser ablation. Compare the radial strains versus time shown in Figure 5.4C and Figure 5.5A. Holes created by laser ablation initially expand at strain rates around

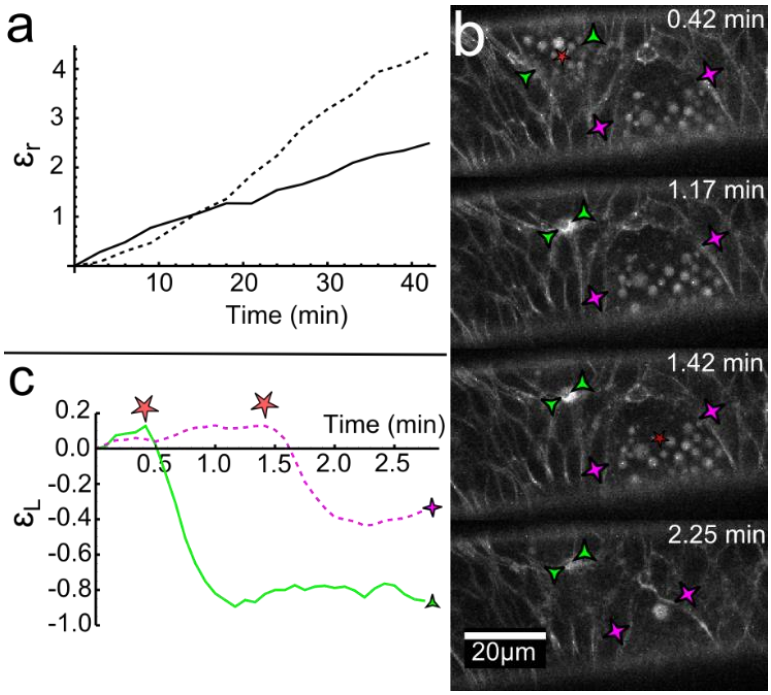

Figure 5.5: Heat-shock-induced holes do not trigger a wound healing response. (**A**) Radial strain versus time for two heat-shock-induced holes, one opening at Bownes stage 8 (dashed line), and another at stage 12 (solid line). Note how different the scales are for radial strain and time compared to laser hole drilling shown in Figure 5.4C. (**B**) Time-lapse images of laser hole drilling that targeted locations inside two pre-existing heat-shock-induced holes. The entire time-lapse image set is available as Supplemental Movie S3. Targeted locations and times marked by red 5-point stars: one in 0.42-min image; one in 1.42-min image. Additional markers (green 3-point stars: magenta 4-point stars) track margins of the heat-shock-induced holes during the response to laser ablation. (**C**) Linear strain versus time across the heat-shock-induced holes. Each curve is labeled with the marker corresponding to the tracked locations in (**B**). Time of laser ablation inside the existing holes is marked with red 5-point stars.

0.02 s^{-1}, but only do so for ~ 5 s before reaching equilibrium and then closing. In contrast, heat-shock-induced holes grow steadily at smaller rates, ~0.001 s^{-1}, but for much longer times, from tens of minutes to hours (compare Figure 5.5A to Figure 5.4C). These behaviors point to a fundamental difference: laser ablation triggers a wound-healing or extrusion response (Kiehart et al., 2000), but most heat-shock-induced holes do not. The few cases in which heat-shock-induced holes reached a modest size and then healed comprised only 17% (N = 43, all strains) and 12% (N=33, E-cadherin-GFP) of heat-shocked embryos respectively exposed or not exposed to

continuous imaging. In embryos that were continuously imaged, only the smallest holes healed, i.e., those that grew to less than the width of a cell, and there were no signs of later developmental defects. The lack of a wound-healing response for the large majority of heat-shock-induced holes suggests that the surrounding cells either do not detect the damage or cannot mount an appropriate response.

The results in Figure 5.4C already demonstrate that heat-shocked tissues are still capable of sensing damaged cells and mounting an extrusion response. To test whether this capability is missing in cells adjacent to heat-shock-induced holes, we used laser ablation to drill holes in these cells or even within the large hole already present. As shown in Figure 5.5B-C, these cells do quickly respond to laser damage. In both cases shown, the laser was targeted to a point inside an already present hole. Within tens of seconds after laser ablation, both slowly opening holes underwent a rapid contraction. This contraction was not sufficient to close the holes entirely, but does clearly show that an extrusion response could be triggered. Heat-shocked tissue is thus capable of a wound healing response, but heat-shock-induced holes do not trigger that response. The lack of a wound-healing or extrusion response allows the heat-shock-induced holes to continue opening on a slow march to large-scale structural failure.

5.2.3 How do heat-shock-induced holes initiate?

We collected time-lapse images of heat-shocked E-cadherin-GFP embryos to investigate the mechanisms by which heat-shock-induced holes initiate. Figure 5.6 shows two separate examples of holes opening in the amnioserosa during germband retraction. As shown in the time-lapse images of Figure 5.6A, some holes open after the apparent dissolution of adherens junctions and local failure of cell-cell adhesion. Over the course of tens of minutes, fluorescence

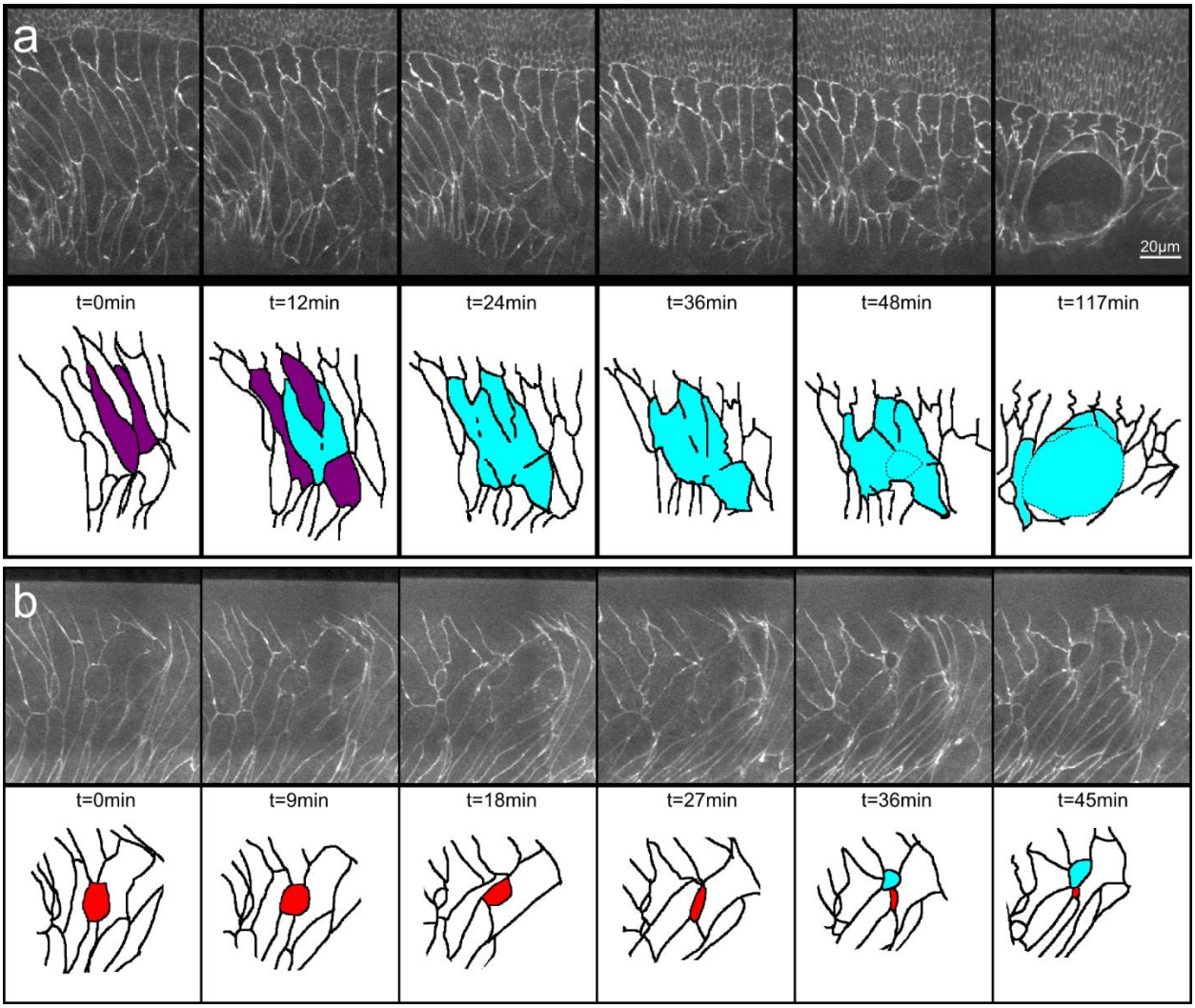

Figure 5.6: Holes initiate at failed cell-cell edges and after delamination events. Time-lapse images (top) and matching simplified traces (bottom) that capture the opening of holes in the amnioserosa after (**A**) dissolution of cell-cell adhesions or (**B**) an attempted cell extrusion. The entire time-lapse image sets are available as Supplemental Movies S4 and S5. (**A**) Simplified traces highlight cells susceptible to hole formation (purple), cells with gaps in their fluorescently labeled adherens junctions (blue), and an outline of the expanding hole (dotted line). (**B**) Simplified traces highlight a rounded cell (red) being extruded from the amnioserosa and the initiation of a nascent adjacent hole (blue).

is lost from one cell-cell boundary and then another until two cells sharing one of the degraded interfaces pull apart and leave a void or hole between the cells. As shown above, this hole then continues to grow without triggering an extrusion response. Other holes appear to open after incomplete extrusion of a cell. The example in Figure 5.6B shows one cell (highlighted in red)

shrinking in apical area over the course of tens of minutes. Just before it is completely extruded from the amnioserosa, which is a simple epithelium, a hole opens between the cell being extruded and two of its neighbors. In both cases, the holes that eventually gape open are not the result of a single cell degrading, but rather a void opening between two cells. We captured similar time-lapse images in moesin-GFP embryos in which holes opened adjacent to an attempted cell extrusions – with some of these actually reaching a stage where the apical surface of the extruded cell reduced to a single bright point before the hole opened.

Since all of these involved apparent failures of cell-cell adhesion, we measured how heat shock affected the later localization of E-cadherin to adherens junctions using immunofluorescence – specifically measuring fluorescence intensity along the interfaces between amnioserosa cells. As shown in Figure 5.7, embryos exposed to a gastrulation-stage heat

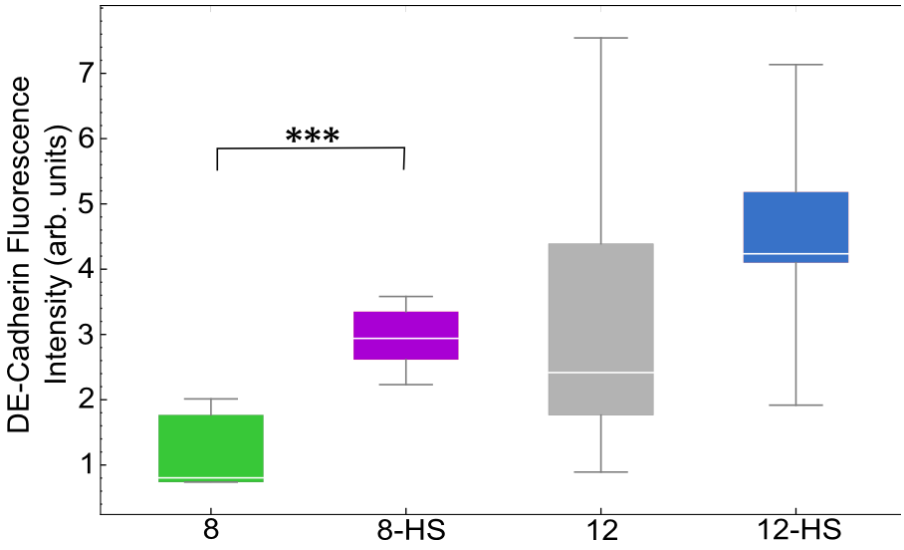

Figure 5.7: Junctional E-cadherin levels increase in the amnioserosa after heat shock. DE-cadherin levels along cell-cell interfaces in the amnioserosa as measured by immunostaining for two different morphological stages (Bownes stage 8, germband extension; 12, germband retraction) in control (N8 = 4, N12 = 8) and heat-shocked embryos (N8-HS = 7, N12-HS = 12). For each immunofluorescence intensity distribution, the box and whiskers mark the median, inter-quartile range, and full range. *** denotes $p < 0.01$.

shock actually have increased junctional E-cadherin staining. In fact, junctional E-cadherin levels in heat-shocked embryos appear to be advanced in morphological age, with levels during post-heat-shock germband extension (stage 8) comparable to those in control embryos during germband retraction (stage 12). The levels increased even further in post-heat-shock stage 12. Similar heat-shock-induced changes were observed for β-catenin immunofluorescence. These findings suggest that the failures of cell-cell adhesion seen above are not due to global decreases in junctional adhesion. The global levels of E-cadherin actually increase after heat shock and suggest that the adhesion failures are due to local misregulation.

To investigate whether this local misregulation involved cell death, we fixed and stained heat-shocked E-cadherin-GFP embryos for alpha-spectrin to outline cells and with DAPI to mark nuclei. Figure 5.8 shows an embryo fixed 7 hours after heat-shock in the morphological stage of germband retraction. Consistent with live imaging reported above, the early heat-shock-induced hole in this embryo contains neither a nucleus nor nuclear fragments, implying that the hole itself is an acellular void. Nuclei are visible in the surrounding amnioserosa cells, but those

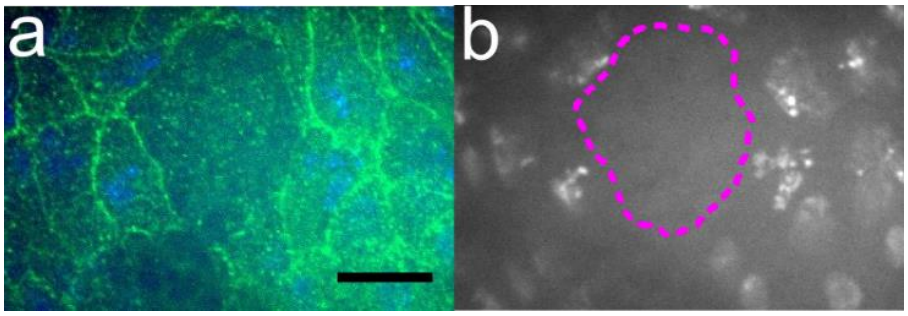

Figure 5.8: Heat-shock-induced holes are anuclear and surrounded by cells with fragmented nuclei. (**A**) Image of a nascent heat-shock-induced hole: DAPI nuclear marker (blue); and α-spectrin immunofluorescence (green). The hole contains no nucleus or nuclear fragments. (**B**) Grayscale image of just the DAPI channel highlights nuclear fragmentation in adjacent cells. Dashed line denotes the hole margins.

immediately adjacent to the hole have undergone nuclear fragmentation – a hallmark of apoptosis. Cells farther removed have maintained normal nuclear structure. We observe similar nuclear fragmentation in cells adjacent to heat-shock-induced holes in other DAPI-stained embryos. We attempted to confirm a role for apoptosis using Apoliner flies that express an mRFP-eGFP reporter of caspase activity (Bardet et al., 2008). We saw no evidence of widespread caspase activity in the amnioserosa of heat-shocked embryos through germband retraction; however, zygotic expression of this reporter is very weak until dorsal closure. The reporter clearly shows the normal apoptosis of amnioserosa cells during dorsal closure (stages 13-15), but it would be very difficult to detect a handful of earlier apoptotic events. Nonetheless, nuclear fragmentation suggests that the initiation of heat-shock-induced holes in the amnioserosa does involve apoptosis of small cell clusters.

5.3 Discussion

Results presented here show that a 30-min heat shock applied at the onset of gastrulation leads to a number of subsequent changes in development. First, characteristic morphological stages are delayed. This delay includes an offset of 2 to 4 hours for recovery from heat shock and a significant slowing of germband extension – accompanied by similarly slow changes in amnioserosa cell morphology. Second, the spatial extent of germband extension is reduced, with the telson not moving as far anteriorly, and the subsequent temporal pause between extension and retraction is shortened. Third, holes open between cells in dorsolateral regions of the amnioserosa (during germband extension and retraction) that slowly and relentlessly expand to diameters exceeding 100 μm. Fourth, large fractions of the embryos eventually develop defects that phenocopy mutants with errors in segmentation, head morphogenesis, germband retraction

and dorsal closure. The latter three defects are positively correlated with the earlier presence of amnioserosa holes.

Closer investigations of the post-heat-shock amnioserosa showed that these cells were not uniformly deficient in the localization of E-cadherin to adherens junctions, nor did they yield large holes after localized destruction of cell-cell junctions via laser ablation. In fact, the results showed that post-heat-shock amnioserosa cells had E-cadherin levels and responses to laser ablation that appeared overly mature: heat-shocked embryos in morphological stage 8 being more similar to control embryos in stage 12. In addition, these studies showed that the slow, but large-scale opening of holes in heat-shocked embryos proceeded by evading the normal mechanisms that maintain or restore epithelial integrity. Laser ablation of regions within or adjacent to heat-shock-induced holes evoked contractions that attempted to close the hole, but the initial slowly opening holes triggered no such response.

With no clear global change in tissue-level tension or cell-cell adhesion, we thus conclude that hole initiation is a local event involving changes in small groups of amnioserosa cells. In several cases, hole initiation was preceded by the disappearance of E-cadherin-GFP fluorescence along one or more cell-cell interfaces. In others, amnioserosa holes were preceded by apparent attempts to extrude cells from this simple epithelium. When cells around nascent holes were examined in fixed and DAPI-stained embryos, many of these cells had segmented nuclei – typically a sign of apoptosis. Attempts to confirm the involvement of apoptosis using heat-shocked Apoliner flies was inconclusive, but zygotic expression of the Apoliner reporter construct is very weak at the time when holes begin to open.

Synthesizing and interpreting these results, we propose the following model for the pathway by which gastrulation-stage heat shocks phenocopy u-shaped mutants. First, we propose

that heat shock leads to intra-embryo heterochronicity – i.e., a disruption of temporal coordination between cell behaviors and morphological changes in adjacent tissues – with amnioserosa cells developing prematurely (or germband cells developing more slowly). This mismatch leads a few cells in the dorsolateral amnioserosa to undergo apoptosis while the germband is still extended. In control embryos, a few amnioserosa cells in this same region apoptose in late germband retraction or early dorsal closure (Sonia Muliyil et al., 2011; S. Muliyil & Narasimha, 2014; Sokolow et al., 2012). These dying cells are normally extruded from the epithelium in a process that contributes to the morphogenetic forces of dorsal closure (Toyama et al., 2008). After a heat shock, the apoptotic events occur when amnioserosa cells are still highly elongated and squamous. Under these conditions, the extrusion process fails, or in some cases cannot even begin, and holes open up between an apoptosing cell and one or more of its neighbors. The late-stage apoptosing cell no longer triggers an extrusion program in its neighbors (Rosenblatt, Raff, & Cramer, 2001) and the hole thus slowly and relentlessly grows. Such large holes disrupt the mechanical integrity of the amnioserosa and prevent it from supplying the tensile forces it normally contributes to germband retraction and dorsal closure. Without these forces, one or both morphogenetic processes fail. This final step is supported by previous experiments in which germband retraction and/or dorsal closure failed because amnioserosa structural integrity was disrupted by either laser ablation (M. S. Hutson et al., 2003; Kiehart et al., 2000; H. E. Lynch et al., 2013; Holley E. Lynch et al., 2014; Solon et al., 2009; Toyama et al., 2008; Wells et al., 2014) or widespread premature apoptosis (U-shaped group mutants; Frank & Rushlow, 1996; GoldmanLevi et al., 1996; Lamka & Lipshitz, 1999).

In support of the heterochronicity aspects of our model, we note that hole initiation in heat-shocked embryos peaked between 5-7 hpg. Of the twenty-nine holes catalogued in Figure

5.1C, fifteen were first observed in this two-hour window (with only one appearing earlier). In control embryos, this window is when germband retraction ends and dorsal closure begins – exactly when amnioserosa cells normally commence apoptosis and extrusion. We hypothesize that the development of non-amnioserosa tissues is delayed by heat shock and amnioserosa development thus appears premature.

Heterochronicity could thus lead to developmental defects through premature apoptosis in the amnioserosa, but heterochronicity could also explain a number of other observations. First, the swirled patterns of ectodermal cells seen during the early recovery from heat shock (Figure 5.1A) could result from premature elongation of amnioserosa cells. These patterns resemble arm mutants in which germband extension is blocked, but amnioserosa cells still elongate (Pope & Harris, 2008). Second, the slower and less complete post-heat-shock extension of the germband could result from amnioserosa cells that prematurely stopped their autonomous elongation. This would increase the force working against the actively extending germband (Blankenship et al., 2006; Irvine & Wieschaus, 1994; Lecuit & Lenne, 2007) – slowing its extension and preventing the telson from reaching its normal anterior-most position. Third, the shortened or even missing pause between germband extension and retraction could be due to the premature transition of amnioserosa cells from elongation to stasis to contraction (H. E. Lynch et al., 2013; Schöck & Perrimon, 2002) – allowing germband retraction to begin as soon as its active extension stopped. Fourth, the high levels of junctional E-cadherin seen in heat-shocked amnioserosa cells (Figure 5.7) could result from a premature occurrence of the increases seen during normal development (Goldenberg & Harris, 2013). These are plausible explanations, but the evidence for heterochronicity is admittedly circumstantial. It will be interesting to see whether future

experiments support the heterochronicity model, especially those measuring tissue-specific gene expression profiles.

In addition, we note four key questions that will require further investigation. First, we must confirm whether the nuclear fragmentation seen in a subset of post-heat-shock amnioserosa cells is due to apoptosis by imaging additional markers such as dUTP nick-end labeling (TUNEL; Denton & Kumar, 2015) or annexin-V binding (van den Eijnde et al., 1998). Second, we must determine whether the signs of premature cell death seen around nascent holes are correlative or causative. Doing so will require the application of gastrulation-stage heat shocks to embryos in which apoptosis is suppressed – either by expression of the baculovirus P35 protein (Hay, Wolff, & Rubin, 1994) or in embryos homozygous for head-involution defective, reaper, grim, or the H99 chromosomal deletion that removes all three of these pro-apoptotic genes (Hay & Guo, 2006; Steller, 2008; White et al., 1994). Third, we need to determine how the normal cell extrusion process fails after heat shock. Such extrusion is carefully orchestrated to squeeze dying or damaged cells out of an epithelium without compromising epithelial integrity (Sonia Muliyil et al., 2011; Rosenblatt et al., 2001; Slattum, McGee, & Rosenblatt, 2009). We will need future imaging studies with other reporters and faster temporal resolution to evaluate whether extrusion failure can be attributed to slower contraction around the cell to be extruded, to an accelerated loss of its adhesive contacts, or to the cells' extremely elongated and squamous nature. Finally, on a closely related note, we need to determine why heat-shock-induced holes in the amnioserosa open unchecked and without triggering a wound-healing response. The triggering signal for wound healing and extrusion in vertebrate cells is the lipid sphingosine-1-phosphate (S1P) (Gu, Forostyan, Sabbadini, & Rosenblatt, 2011), but *Drosophila* has no known S1P receptors (Oskouian & Saba, 2004; Pantoja, Fischer, Ieronimakis, Reyes, & Ruohola-Baker, 2013). Prior

studies in *Drosophila* have shown that contractile rings and extrusion can be triggered by an apoptotic cell, by overcrowding (Marinari et al., 2012), or by mechanical stress via stretch-activated channels (S. Muliyil & Narasimha, 2014). Heat-shock-induced holes may thus evade the normal epithelial damage response either because (1) the holes initiate late in a failed extrusion attempt outside the critical window during which an apoptotic cell provides its unknown signal or (2) expansion of the hole is sufficiently slow that its associated strain rates are less than those needed to open relevant stretch-activated channels. In future studies, heat-shock-induced holes may be a good model system for delineating the contributors to and limitations of the *Drosophila* cell extrusion process.

Future studies will also need to address the curious correlation between amnioserosa holes and heat-shock-induced head defects – a correlation for which direct causation seems unlikely. Head involution is simultaneous with dorsal closure, but involves no known role for the amnioserosa (VanHook & Letsou, 2008). There is however a significant role for apoptosis, as evidenced by the eponymous mutant head involution defective (hid), whose wild-type allele encodes a pro-apoptotic gene (Abbott & Lengyel, 1991; Grether, Abrams, Agapite, White, & Steller, 1995). If heat shock induces premature apoptosis and holes in the amnioserosa, it may also do so in the head region. Future experiments with targeted and improved imaging of the head region may allow delineation of the pathway to hid phenocopies.

The pathway we have delineated for ush phenocopies highlights the way a non-specific environmental stress can impact two common developmental mechanisms: (1) the temporal coordination of complementary morphogenesis in adjacent tissues; and (2) the regulated use of programmed cell death. Both mechanisms are important not only in *Drosophila*, but also in C. elegans – where heterochronicity in cell fate specification is a known mechanism of

developmental defects (Reinhart et al., 2000) – and in vertebrate and human development. It will be interesting to see whether heterochronicity and/or premature apoptosis play a role in the neural tube defects linked to hyperthermia in vertebrate models (M. J. Edwards, 1986) and in human populations (Kline, Stein, Susser, & Warburton, 1985; Milunsky et al., 1992) or in the broader spectrum of developmental abnormalities caused by other environmental stresses – e.g., hypoxia, oxidative damage or inflammation. The results presented here highlight the importance of considering the cell- and tissue-level mechanics of development alongside its genetic and molecular mechanisms. A complete description of stress-induced phenocopies will require both complementary approaches.

5.4 Materials and Methods

See Appendix D. Supplemental Movies are provided in the Online Materials of Crews, McCleery, and Hutson (2016).

CHAPTER 6

HOLES IN NORMAL AND ABERRANT TISSUE ARE A MECHANICAL FAILURE

In Chapter 5, we found that a non-specific heat shock applied to the embryo can produce holes in the amnioserosa tissue. Although the mechanical properties of the post-heat shock tissue are found to be largely unchanged, these holes lead to embryo-wide failure of germband retraction. In Chapter 4, we found germband retraction is robust to the specific allocation of cell-cell interfacial tensions, but dependent on initial cell geometry. In light of these findings, we expand the model to study the impact of an incoherent tissue on germband retraction. We recapitulate mutant phenotypes to determine the strictly mechanical processes that cause germband retraction to fail. We find a coherent sheet of cells is necessary for germband retraction to proceed.

6.1 Germband retraction requires a coherent epithelial sheet

We consider the embryo's mechanical robustness to absent or weakened amnioserosa tissue as a result of mutation or surgical manipulation. To remove all or a portion of the amnioserosa cells *in silico*, selected homogeneous cell edges are assigned a cell-cell interfacial tension, $\gamma_{ASAS} = 0$. For selected amnioserosa cells bordering the germband, the border edges are assigned a value of $\frac{1}{2}\gamma_{GBAS}$ to remove only the contribution of amnioserosa cells. We test three cases with various amounts of amnioserosa cells left intact.

First, we cut a small set of cells near the germband-amnioserosa border to determine if a small discontinuity in the epithelium is sufficient to prevent germband retraction. The cells,

shown in Figure 6.1A, were chosen since they lie in the crook of the germband, where the amnioserosa cells apply the greatest concentration of stress to germband tissue. Despite the absence of tension between these cells, germband retraction does complete with little deviation from the kinematics of the base model. H. E. Lynch et al. (2013) also finds that germband retraction progresses unhindered *in vivo* (Figure 4F reprinted in Figure 6.1A).

Second, we remove tension from one lateral flank of the amnioserosa to consider the possibility that half of the amnioserosa could drive retraction. Figure 6.1B shows that although the intact amnioserosa cells do reduce their aspect ratio, the unbalanced distribution of stress in the mesh causes the posterior end to twist. Thus, the telson rotates toward the 'wounded' lateral side, and germband retraction fails. Interestingly, a similar result is shown *in vivo* when laser microsurgery is used to cut one lateral side of the amnioserosa tissue (H. E. Lynch et al., 2013). Close inspection of H. E. Lynch et al. (2013) Figure 4A, reprinted in Figure 6.1B, shows the telson (marked with a green arrowhead) has shifted towards the wounded lateral side.

Third, we completely remove the amnioserosa, leaving no tension between any amnioserosa cells. The resulting mesh, shown in Figure 6.1C, fails to retract, allowing only residual movement of the telson and germband. These results recapitulate U-shape group mutants, shown in Figure 6.1C', which genetically eliminate the amnioserosa by inducing premature apoptosis (Frank & Rushlow, 1996). Together, these *in silico* results, validated by *in vivo* experimentation, show that proper germband retraction is robust to small wounds in the epithelium but largely requires one coherent epithelial sheet.

To further test this requirement, we attempt an *in silico* rescue of the U-shape group mutant by adding polarization to the germband cells. Polarization redistributes the net tension along a cell's edges to be parallel to the germband-amnioserosa border, such that the edges with

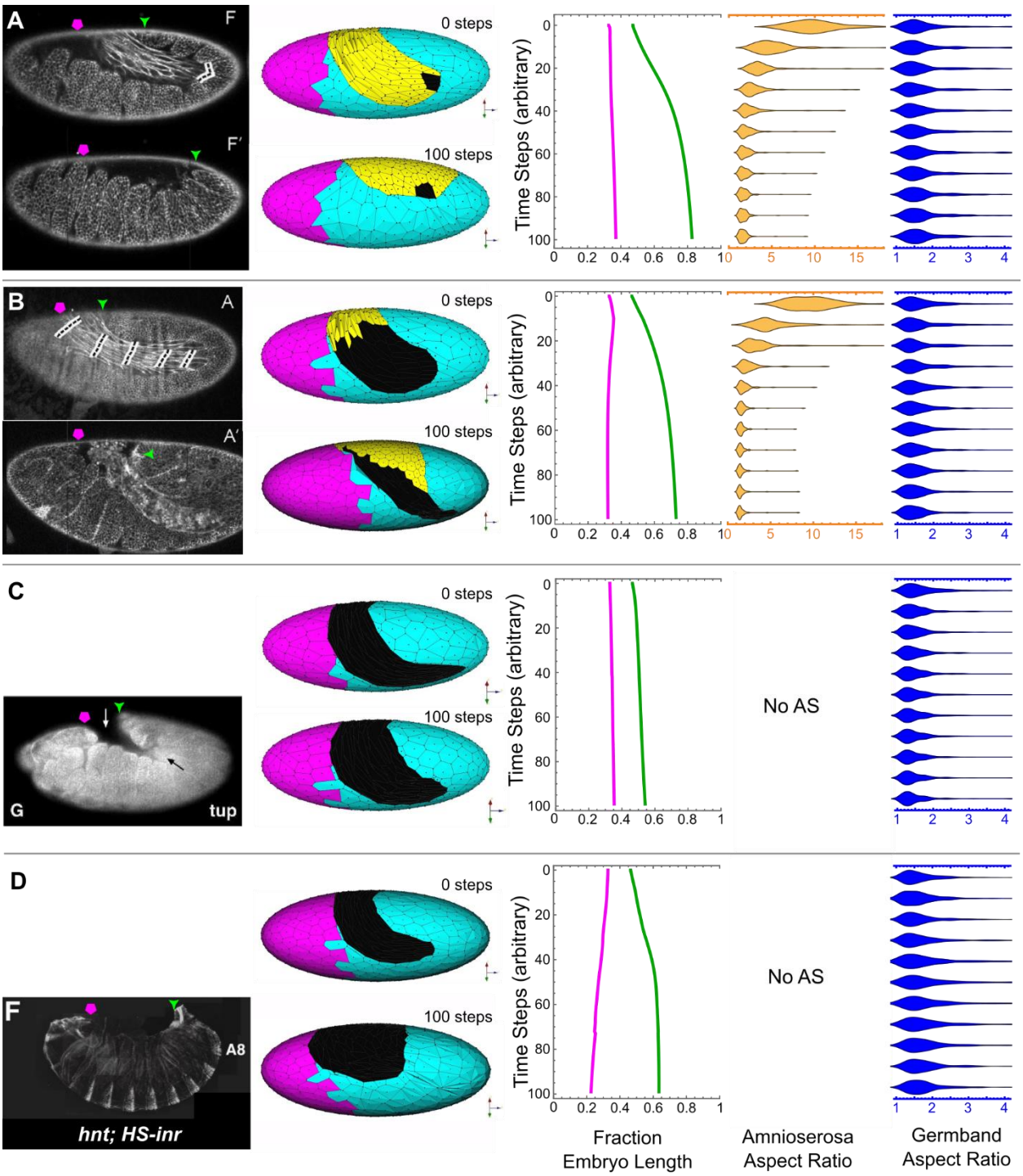

Figure 6.1: Model can replicate mutant and partial rescue *in vivo* phenotypes. (**A-B**) Laser microsurgery experiments cutting portions of the amnioserosa (dashed lines; modified from H. E. Lynch et al. (2013)). Base model replicates these cuts by assigning $\gamma_{ASAS} = 0$ in black cells. Amnioserosa cell aspect ratio chart only measures unaltered amnioserosa cells (yellow cells in mesh). (**C**) U-shp group mutant after failure of germband retraction (modified from Frank and Rushlow (1996)). Amnioserosa cells are removed in model by assigning $\gamma_{ASAS} = 0$ (black cells). No amnioserosa aspect ratios are measured. (**D**) Partial rescue of U-shp group mutant by

overexpressing insulin receptor in the germband (modified from Lamka and Lipshitz (1999)). Model replicates *in vivo* rescue by assigning $\gamma_{ASAS} = 0$ (yellow cells) and 80% polarization in γ_{GBGB} parallel to germband-amnioserosa border (cyan cells, see Appendix B for details). No amnioserosa aspect ratios are measured.

the greatest tension lie along the axis of retraction. In the absence of a stressed amnioserosa tissue, the polarized germband cells are able to provide a partial rescue of germband retraction. This partial rescue *in silico* replicates a rescue *in vivo* that overexpresses the insulin receptor in a U-shape mutant (Lamka and Lipshitz (1999), Figure 7F shown in Figure 6.1D). The qualitative similarity between the *in vivo* and *in silico* rescues justifies a hypothesis that overexpression of the insulin receptor leads to hyper-polarization of the germband. Although a polarized germband does appear capable of producing a partial rescue, this *in silico* partial rescue argues strongly for the mechanical necessity of an intact amnioserosa for proper, full germband retraction.

6.2 Discussion

Germband retraction fails when the epithelium is no longer mechanically coherent either by loss of tissue or by loss of tension between one or more cell-cell edge types. *In silico* experiments that remove γ_{ASAS}, are able to replicate germband retraction failure due to loss of amnioserosa tissue in the U-Shape group mutants and laser microsurgery shown in Figure 6.1. This requirement for epithelial integrity provides an explanation for germband retraction failure in other mutants. For example, genetic mutations such as Scarface and Myospheroid (Reed et al., 2004; Sorrosal, Perez, Herranz, & Milan, 2010) or environmental perturbations such as gastrulation-stage heat shocks (Chapter 5) have been shown to induce holes in the amnioserosa tissue, which fail to complete germband retraction. Complete loss of tension in the amnioserosa also causes a loss of epithelial mechanical integrity. In the trivial case *in silico*, when $\gamma_{ASAS} = \gamma_{GBAS} = \gamma_{GBGB} = 0$, there is no energy in the mesh, so no cell deformation occurs. A more

realistic case is simulated when $\gamma_{GBGB}:\gamma_{GBAS}:\gamma_{ASAS} = 10:10:0$. This condition recapitulates U-Shape group mutants (Frank & Rushlow, 1996) as well as describing a knockdown mutant of amnioserosa specific RhoA (dominant negative UAS-rho1N17:c381-Gal4) (Schöck & Perrimon, 2002). Since RhoA is an upstream regulator of myosin II, dominant negative expression of RhoA prevents tension production via myosin II between amnioserosa cells. In this mutant, germband retraction also fails. We extend this result to predict that germband retraction may fail in any genetic or environmental background that disrupts the cohesive integrity of the epithelium.

The model emphasizes the mechanical necessity of the amnioserosa in driving germband retraction, and provides an architecture on which *in silico* experiments of embryogenesis may be performed. Mutant phenotypes are readily replicated, providing evidence for the explanatory and predictive power of this model. Researchers interested in the mechanics of epithelia that are constrained to an eggshell geometry may find this modeling framework useful; however, this model does not provide the tools to analyze any form of biochemical signaling or communication. Thus, an appropriate use of this tool is to investigate the collective cell migration in a mechanically coupled epithelium constrained to an ellipsoid.

CHAPTER 7

CONCLUSIONS AND FUTURE DIRECTIONS

7.1 Conclusions

Historically, biomechanical analysis of *Drosophila* embryogenesis has focused on identification of the cells which are responsible for morphological change (Allena et al., 2010; Allena et al., 2013; Conte et al., 2009; Conte et al., 2008; Conte et al., 2012; Hocevar Brezavscek et al., 2012; Jose J. Munoz et al., 2007; J. J. Munoz et al., 2010; Odell et al., 1981; Polyakov et al., 2014; Solon et al., 2009; Vroomans, Hogeweg, & ten Tusscher, 2015). This search has prompted modelers to classify cells as active or passive; however, this classification can lead to contradictory results, i.e. compare Conte et al. (2009) with Polyakov et al. (2014). A deeper analysis of these contradictory models reveals that embryos may be mechanically redundant, which can provide embryos with robustness to mechanical perturbations. Moreover, it is clear that deformations in a small group of cells are capable of causing embryo-wide morphogenesis, i.e. germband extension (Allena et al., 2010; Allena et al., 2013). If an embryo is composed of redundant patches of mechanically potent cells, a question arises as to how the embryo ensures these cells coordinate to accomplish morphogenesis. In order to address this question we choose to model a characteristic stage of development, germband retraction.

Our 2.5-dimensional cellular finite element model reveals two features of germband retraction. First, it is mechanically robust to perturbations in cell-specific tensions. This result predicts that the embryo can withstand minor injuries and possibly even mutations that limit production of force-generating proteins such as adhesion junctions and myosin motors. Indeed, the model reveals that germband retraction completes in any configuration that maintains tension

along every cell edge. It also completes when a small number of cells are assigned no cell-cell interfacial tension. Second, germband retraction is shown to be contingent on initial cell geometry. Although embryonic cells do not store elastic potential energy (G. Brodland et al., 2006), the highly elongated shape of the amnioserosa guides the deformation of cells and the flow of tissues. In this manner, we argue that the embryo ensures coordination between multiple active patches of cells through initial cell geometry. By setting up high aspect ratio cells during germband extension, morphogenesis is guided by these cells during germband retraction.

Since cell geometry plays an important role in morphogenesis, we investigate the effect of an injured epithelium. Experimentally, we find a hole forms in the amnioserosa tissue after application of a non-specific heat shock stress to the embryo. Prior to the formation of the hole, the amnioserosa is not less stiff as one might expect from a compromised, unhealthy tissue. Rather the hole appears to be the result of premature apoptosis. This set of conditions, i.e., a hole appearing in an otherwise normal tissue, provides an excellent experimental setting to investigate germband retraction's dependence on a coherent epithelium. *In vivo*, germband retraction halts after the formation of the hole. The 2.5-D model suggests that although germband retraction is robust to specific cell-cell interfacial tension allocation, it remains dependent on a coherent epithelium. This finding is confirmed by other environmental injuries and mutations such as laser wounding of the amnioserosa and widespread amnioserosa cell apoptosis (Lamka & Lipshitz, 1999; H. E. Lynch et al., 2013).

Our biomechanical analysis provides insight into the important aspects of embryogenesis. Multiple stages of embryogenesis are mechanically robust, exploiting redundancy among several active tissues rather than relying on one optimal tissue. This distribution of work is coordinated by cell geometry, which acts as a persistent memory through stages of development by setting up

the initial configurations for each subsequent stage. Since cell geometry is found to play a critical role in morphogenesis, it is not surprising that a coherent epithelium is necessary. In the case of germband retraction, a hole-forming perturbation to the amnioserosa halts progression. Future studies of embryogenesis should consider the impact of the continuous, coherent epithelium. The 2.5-D cellular finite element model is ideal for such biomechanical analyses.

7.2 Future Directions

In the previous chapters, several questions remain unanswered regarding the biomechanics of embryogenesis. Many of these questions provide testable hypotheses that may be addressed in the near future. I present a few of these hypotheses and sketch a design for experiments to test them as relating to the chapters in reverse order.

7.2.1 Hypothesis 1: The amnioserosa alone is sufficient to drive germband retraction.

It has been experimentally shown that the amnioserosa plays an assistive role in germband retraction (H. E. Lynch et al., 2013). Although there are no mutants that induce cell death in the germband, the 2.5-D finite element model presented in Chapter 4 is capable of testing the mechanical contribution of the amnioserosa independent of the germband. By removing the tensions along germband-germband interfaces (γ_{GBGB}), it is possible to mechanically isolate the amnioserosa and determine if the kinematics of this *in silico* germband mutant match *in vivo* data.

7.2.2 Hypothesis 2: Germband retraction is independent of the ellipsoidal geometry of the embryo.

Drosophila embryos vary in egg dimensions naturally, and myospheroid mutants can produce spherical eggs (personal observations and communication with Xiaoxi Wang). Considering the contingency of germband retraction on cell geometry, the effect of the ellipsoidal geometry of the embryo may produce unexpected kinematics. Using the 2.5-D model, the mesh could be rescaled to be constrained to a spherical last. Given that embryos seem to develop normally under these conditions *in vivo*, it is unlikely that there would be an effect on the final phenotype. The trajectory of this morphogenetic process may change though.

7.2.3 Hypothesis 3: Germband extension is driven by active cell intercalation that results from anisotropic stress in germband cells.

The 2.5-D model can easily be re-meshed to explore germband extension. A reasonable initial cell geometry for this mesh would be a continuous epithelium of isodiametric cells, with future considerations of the cell shapes due to gastrulation. The germband extension section of Chapter 2 questioned whether convergent extension of the germband was driven by active cell intercalation of germband cells, or by active elongation of amnioserosa cells. These two plausible mechanisms could be applied in the following way: Anisotropic tension could be applied to germband cells by adding a polarization term to the model, which would promote intercalation (Honda et al., 2008). Alternatively, “microtubule-like” structures could be added to amnioserosa cells to promote elongation (Pope & Harris, 2008). Amnioserosa cell elongation has also been found to exhibit anisotropic expression of adherens junctions, which may also assist in the elongation process (Goldenberg & Harris, 2013). This differential adhesion can be applied to the model by anisotropic tension. Comparing these two sets of parameter should distinguish between plausible mechanisms for germband elongation. In the case of active amnioserosa cell

elongation, it will be interesting to see how amnioserosa cells are reoriented to elongate onto the lateral sides and toward the posterior end of the embryo.

7.2.4 Hypothesis 4: Mutants that do not fail germband retraction take different "trajectories" through morphogenesis.

Chapter 2 concludes with a rationale for the morphogenetic robustness claimed by modelers. Morphogenesis is described to take one of several possible trajectories through an epigenetic landscape as embryos develop under genetic and environmental perturbations (Jaeger & Monk, 2014). Chapter 6 suggests several mutants that may alter the mechanical integrity of the epithelial tissues, yet still produce a phenotype that is qualitatively similar to wild-type embryos at the end of germband retraction. Detailed kinematic analysis of these mutants can confirm that these mutants take different trajectories if the kinematics differ significantly from wild-type development. Additional studies would then follow to address the alternative mechanisms that are used by the embryo to achieve the same final phenotype.

7.2.5 Hypothesis 5: Stochastic amnioserosa cell apoptosis during dorsal closure is regulated by mechanical coupling to caspase signaling pathways.

As described in Chapter 2, amnioserosa cells have been shown to stochastically undergo apoptosis during dorsal closure (Sonia Muliyil et al., 2011). Recently, it has been shown that the upregulation of the apoptotic signaling pathway, which is caspase dependent, is responsible for reducing amnioserosa cell volume and producing the amnioserosa force component that drives dorsal closure (Saias et al., 2015). What remains unclear is how the apical oscillations of these cells are regulated, and to what extent do they play a role in dorsal closure. I propose an experimental set-up that can investigate the possibility of mechanical feedback from cell oscillations into the signaling pathway that initiates apoptosis. This experiment will require a combination of optical tools to probe this dynamic mechanical and chemical process, including

time-lapse fluorescence microscopy, laser microsurgery, and opto-genetics. First, since the oscillatory dynamics of this process are sensitive to external stresses, the embryo will need to be mounted in a controlled space. Yan et al. (2014) present a microcompressor mounting apparatus that can be adjusted to minimize the external stress applied. Second, a careful selection of fluorescent tags will need to be chosen to provide data needed to analyze the dynamics of this system. This selection will likely include fluorescent labels for the regulatory light chain of myosin II (sqh) to mark oscillatory dynamics and myosin II expression, as well as apoliner to mark caspase activity. Third, direct control of myosin II contractions are possible through opto-genetic controls of Rac and Rho. Fourth, a laser ablation system will be needed to remove the tension along cell-cell interfaces. Considering that the fluorescent tags and opto-genetics will require four distinct excitation wavelengths, it will be necessary to find a confocal microscope that can meet the imaging and ablating capabilities required. The initial experiment will be to observe the relationship between oscillatory dynamics and caspase activity. This involves time-lapse imaging of embryos expressing sqh and apoliner. If it is validated that there is a correlation between these two events, the next experiment will perturb the oscillations by laser ablation in order to reduce the equilibrium tension of the amnioserosa. If cell contractions are the cause of caspase activity, this perturbation should reduce the number of stochastic apoptotic events. Finally, mapping the mechanical feedback into the signaling network will require inducing contractions through photoactivatable rho/rac proteins. Pulsed laser exposure to these photoactivatable proteins should drive the cells to oscillate faster than their natural frequency, which potentially could increase the rate of stochastic caspase activity. This experiment will require significantly more planning, but ideally the results of this work could provide the data necessary to construct a complete model of amnioserosa contractions in dorsal closure.

These proposed experiments would push the field of biomechanics in two ways: First, they would contribute to the effort to build a complete model of *Drosophila* embryogenesis. Second, they would provide a much-needed bridge between signaling pathways and mechanical structures. The future is brimming with possibilities. It is my intent to pursue them.

APPENDIX A

A PRIMER ON BRODLAND'S CELLULAR FINITE ELEMENT MODEL

Under the cellular Finite Element modeling formalism, an epithelial tissue is broken into finite elements that each approximate a cell (G. W. Brodland et al., 2007). As shown in Figure 3.7B, the cells or finite elements are individual polygons where the edges act as tension rods which connect at the vertices, called nodes. Each node is the triple point junction of three cells, which each apply an equivalent force onto the node. These equivalent forces displace the node, which in turn deforms the cell. The collection of all displaced nodes results in the deformation of the tissue at each time step. This process follows standard finite element procedures outlined in several resources (Belegundu & Chandrupatla, 2002; Zienkiewicz & Taylor, 2005). Here, I outline the steps taken by the finite element engine to solve the deformations induced by applying cell-level forces.

A.1 Define Finite Elements

A continuum representing the tissue is divided into discrete sub-surfaces, called finite elements. In order to create a biologically-significant model, G. W. Brodland et al. (2007) uses polygonal finite elements, which each define a cell. The edges of each polygon define the border of the cell, and consequently the cell-cell interfaces. In this way, the interface created by two adjacent plasma membranes is approximated as a single edge in the model. Each node is a triple-point junction of three edges. It should be emphasized that the finite element engine only considers forces applied to the nodes. In our model of the entire embryo, we will create a continuous mesh of cells to construct a two-dimensional shell. The nodes and centroids of each cell will be constrained to lie on the surface of an ellipsoid, such that the coherent cell mesh will

form a model of the continuous epithelial tissues. For now, let's consider a single isolated cell for simplicity, ignoring boundary conditions as our 2.5-D model will be continuously connected.

A.2 Formalize Nodal Displacement

Local deformations occur in the continuum by displacement of the nodes. The model is built to analyze the deformation of tissue based on individual cell shape change. Cells change shape by displacement of the nodes. Since all nodes are triple-point junctions, each node is subject to forces from the three corresponding cells. As the model runs, node displacement is the unknown variable that is solved at each time step. A displacement vector, u', is defined for each node at each time step in local coordinates, as shown in Figure A.1. This local vector is transformed to global coordinates, u, as shown in (Belegundu & Chandrupatla, 2002):

$$\begin{aligned} u_1{}' &= u_{1,x}{}' + u_{1,y}{}' \\ &= u_1 \cos\theta + u_1 sin\theta \\ &= u_1 cos\theta + u_1 cos\phi \\ &= u_1\, l + u_1\, m \end{aligned} \qquad \text{Eq. A-1}$$

where ϕ is the complement of θ, and l and m are direction cosines.

Displacement of nodes is uniquely defined by a set of displacement functions within each finite element. This set of functions takes the form of a vector matrix in local and in global coordinates,

$$\begin{aligned} u' &= \begin{bmatrix} u_{1,x}{}' \\ u_{1,y}{}' \\ u_{2,x}{}' \\ \vdots \end{bmatrix} \\ &= \begin{bmatrix} l & m & 0 & 0 & \dots \\ 0 & 0 & l & m & \dots \\ \vdots & \vdots & \vdots & \vdots & \ddots \end{bmatrix} \begin{bmatrix} u_1 \\ u_1 \\ u_2 \\ \vdots \end{bmatrix} \end{aligned} \qquad \text{Eq. A-2}$$

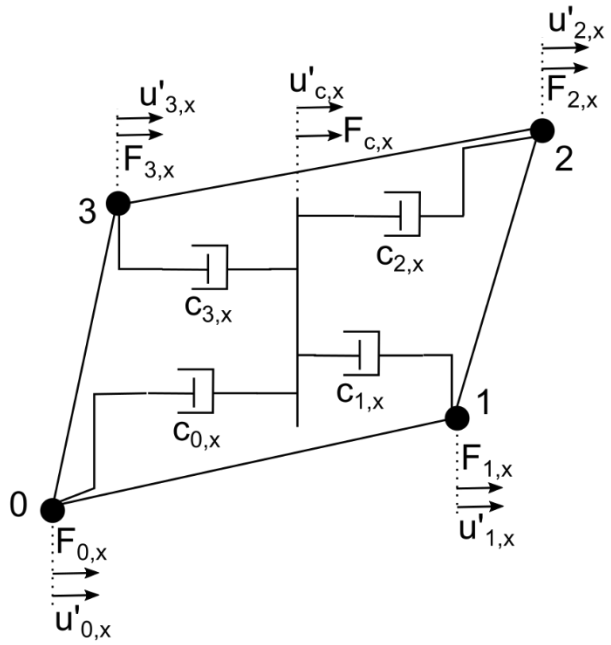

Figure A.1: Single Cellular Finite Element. Four nodes are labeled in local coordinates, 0 to 3. A system of orthogonal dashpots connect each node along both the x and y-axes. (Only x-axis network shown.) Dashpots are each connected to one node and a central floating bar. The bar is a mechanical construct used to define the system, but it will be removed mathematically prior to solving the finite element system of equations. Each dashpot has an associated damping coefficient, $c_{i,x}$. Each node and the floating bar has a displacement, $u_{i,x}{}'$, and an applied force, $F_{i,x}$.

By collecting the displacement matrices for each node, it is possible to determine the strain for each element. For now, let's consider the strain of one element in local coordinates.

A.3 Calculate Stress due to Strain

Stress due to strain is calculated for each element by considering nodal displacements and material properties. Each cell is given viscous damping, which is applied through two orthogonal networks of dashpots, as shown in Figure A.1. A dashpot is a mechanical element with force proportional to the node's velocitiy, v, and potential energy proportional to the square of velocity:

$$F_{dashpot} = -cv \qquad \text{Eq. A-3}$$

$$U_{dashpot} = \frac{1}{2}cv^2 \qquad \text{Eq. A-4}$$

where c is the viscous coefficient with units of $\frac{Ns}{m}$. G. W. Brodland et al. (2007) derive the viscous coefficient for a theoretical cell approximated as a regular hexagon undergoing isochoric deformation (stretching without changing volume). The viscous coefficient in the x-direction is

$$c_x = 4\pi\xi\frac{\mu B}{nA} \quad \text{Eq. A-5}$$

where ξ is a form factor determined empirically, μ is the viscosity of the cell, and A and B are the semi-major and minor axes of a best-fit ellipse. The coefficient is thus dependent on the shape of the cell. The y-direction coefficient, c_y, mimics the above equation, but it has an inverse dependence on A and B. Note that the viscous coefficient is inversely proportional to the number of nodes, n, in the cell. Although each node is attached to its own dashpot (one in each direction), the orthogonal array connects all n nodes as shown in Figure A.1. When a single node is displaced, the resistive force is distributed across the array, reducing the compression of any single dashpot. This distribution of damping force is best understood in the damping matrix. The damping matrix assigns the appropriate damping coefficient to each node. To calculate this matrix, we refer to principle of virtual work for the system.

Principle of Virtual Work*: A body is in equilibrium if the internal virtual work equals the external virtual work for every kinematically admissible displacement field (δ, $\epsilon(\delta)$) (Belegundu & Chandrupatla, 2002).*

Consider the virtual work that can be done on the system in terms of potential energy. We expect the potential energy, Π, to come in two forms, strain energy due to deformation, U, and work potential energy due to applied stress, WP.

$$\Pi = U + WP \quad \text{Eq. A-6}$$

In this system, strain energy is the result of work done on the dashpot network.

$$U = \frac{1}{2}\sum_i c_i v_i^2 \qquad \text{Eq. A-7}$$

where c_i is the damping coefficient associated with node i, and v_i is the differential velocity between node associated with node i and an imaginary floating bar that connects each dashpot within its network as shown in Figure A.1. The work potential energy applied to the nodes will be discussed in more detail in the next section. At this point, let's consider a cumulative point force acting at each node.

$$WP = -\sum_i F_i \delta_i \qquad \text{Eq. A-8}$$

In order to determine form of the damping matrix, let us consider a simple cell composed of four nodes as shown in Figure A.1. This system has one dashpot for each node in each direction. Only considering dashpots lying along the local x-axis, we find the total potential energy to be

$$\Pi = \frac{1}{2}\mathrm{c}_0 v_0^2 + \frac{1}{2}\mathrm{c}_1 v_1^2 + \frac{1}{2}\mathrm{c}_2 v_2^2 + \frac{1}{2}\mathrm{c}_3 v_3^2 - F_{0,x}x_0 - F_{1,x}x_1 - F_{2,x}x_2 - F_{3,x}x_3 \qquad \text{Eq. A-9}$$

If we expand the differential velocity term for each dashpot, it is clear that the effective velocity is the difference of the node velocity, $\dot{x}_i$, and the central bar velocity, $\dot{x}_C$.

$$\Pi = \frac{1}{2}\mathrm{c}_0(\dot{x}_0 - \dot{x}_C)^2 + \frac{1}{2}\mathrm{c}_1(\dot{x}_C - \dot{x}_1)^2 + \frac{1}{2}\mathrm{c}_2(\dot{x}_C - \dot{x}_2)^2 + \frac{1}{2}\mathrm{c}_3(\dot{x}_3 - \dot{x}_C)^2 - F_{0,x}x_0 - F_{1,x}x_1 - F_{2,x}x_2 - F_{3,x}x_3 \qquad \text{Eq. A-10}$$

Since our final goal is to find the displacement of each node that solves this equation, we can discretize this continuous statement of potential energy into sufficiently small time steps. The differential velocity is approximated as the difference in node and central bar displacements per time step.

$$\Pi = \frac{1}{\Delta t}\left[\frac{1}{2}c_0(x_0 - x_C)^2 + \frac{1}{2}c_1(x_C - x_1)^2 + \frac{1}{2}c_2(x_C - x_2)^2 + \frac{1}{2}c_3(x_3 - x_C)^2\right] - F_{0,x}x_0 - F_{1,x}x_1 - F_{2,x}x_2 - F_{3,x}x_3 \quad \text{Eq. A-11}$$

In this form, the system is considered to be conservative, meaning work is path independent. This assumption is only valid for time steps that are sufficiently small to neglect the rate of displaced nodes. If this condition holds, we can use the principle of minimum potential energy.

Principle of Minimum Potential Energy*: For a conservative system, the displacement field corresponding to the equilibrium will extremize the total potential energy (Belegundu & Chandrupatla, 2002).*

To apply this principle, we set $\nabla\Pi = 0$, which provides the system of equations:

$$\begin{aligned}
\frac{\delta\Pi}{\delta x_0} &= 0 = \frac{c_0}{\Delta t}(x_0 - x_C) - F_{0,x} \\
\frac{\delta\Pi}{\delta x_1} &= 0 = -\frac{c_1}{\Delta t}(x_C - x_1) - F_{1,x} \\
\frac{\delta\Pi}{\delta x_2} &= 0 = -\frac{c_2}{\Delta t}(x_C - x_2) - F_{2,x} \\
\frac{\delta\Pi}{\delta x_3} &= 0 = \frac{c_3}{\Delta t}(x_3 - x_C) - F_{3,x} \\
\frac{\delta\Pi}{\delta x_C} &= 0 = -\frac{c_0}{\Delta t}(x_0 - x_C) + \frac{c_1}{\Delta t}(x_C - x_1) + \frac{c_2}{\Delta t}(x_C - x_2) - \frac{c_3}{\Delta t}(x_3 - x_C)
\end{aligned} \quad \text{Eq. A-12}$$

Considering the last equation only, we can reduce the system of equations by rewriting x_C in terms of the nodal displacements. This simplification reduces the number of equations that must be solved as well as eliminating a trivial displacement that has no biological meaning.

$$x_C = \frac{c_0x_0 + c_1x_1 + c_2x_2 + c_3x_3}{c_0 + c_1 + c_2 + c_3} \quad \text{Eq. A-13}$$

Substituting for x_C, the system of equations reduces to four equations that can be rewritten to seqarate the strain terms from the applied stress terms.

$$F_{0,x} = \frac{1}{\Delta t}\left(c_0 x_0 - c_0\left(\frac{c_0x_0+c_1x_1+c_2x_2+c_3x_3}{c_0+c_1+c_2+c_3}\right)\right) F_{1,x} =$$
$$-\frac{1}{\Delta t}\left(c_1\left(\frac{c_0x_0+c_1x_1+c_2x_2+c_3x_3}{c_0+c_1+c_2+c_3}\right) - c_1x_1\right)$$
$$F_{2,x} = -\frac{1}{\Delta t}\left(c_2\left(\frac{c_0x_0 + c_1x_1 + c_2x_2 + c_3x_3}{c_0 + c_1 + c_2 + c_3}\right) - c_2x_2\right) \qquad \text{Eq. A-14}$$
$$F_{3,x} = \frac{1}{\Delta t}\left(c_3x_3 - c_3\left(\frac{c_0x_0 + c_1x_1 + c_2x_2 + c_3x_3}{c_0 + c_1 + c_2 + c_3}\right)\right)$$

So far, we have left the damping coefficients in general terms, allowing each dashpot to have a unique viscous damping. Recall in our earlier discussion, the coefficients of every dashpot that is oriented in the same direction within a cell are equal. They are also dependent on the number of nodes in the cell. If we consider that there are four nodes and each node's dashpot will be opposed by three other dashpots, we can explicitly remove a factor of $\frac{4}{3}$ from the coefficient.

$$c_0 = c_1 = c_2 = c_3 = \frac{4}{3}p_x \qquad \text{Eq. A-15}$$

With these substitutions, the system of equations simplifies, and can be written in a convenient matrix notation similar in form to Eq. 3-2:

$$\frac{1}{\Delta t} C \cdot u' = f \qquad \text{Eq. A-16}$$

$$\frac{1}{\Delta t}\begin{bmatrix} p_x & -p_x/3 & -p_x/3 & -p_x/3 \\ -p_x/3 & p_x & -p_x/3 & -p_x/3 \\ -p_x/3 & -p_x/3 & p_x & -p_x/3 \\ -p_x/3 & -p_x/3 & -p_x/3 & p_x \end{bmatrix}\begin{Bmatrix} x_0 \\ x_1 \\ x_2 \\ x_3 \end{Bmatrix} = \begin{Bmatrix} F_{0,x} \\ F_{1,x} \\ F_{2,x} \\ F_{3,x} \end{Bmatrix} \qquad \text{Eq. A-17}$$

The damping matrix, C, has several properties worth mentioning. First, every row sums to zero. In the event that the entire cell is translated, meaning all displacements are equal, then no work due to strain would be produced. Second, every column sums to zero. If one node is displaced, but the remaining nodes are stationary, then the network of dashpots must distribute the load. A single column shows the damping contribution of each dashpot on a single node.

Since every dashpot has the same damping properties, the coefficient of a node's primary dashpot is equal and opposite the sum of the remaining dashpots. Intuitively, the remaining dashpot coefficients are divided by 3, corresponding to the 3 other nodes in the system. In general, the off-diagonal coefficients will be divided by $n-1$ for an n-node polygon. Third, these coefficients are also dependent on the cell shape, specifically the aspect ratio of the cell. If the aspect ratio is 2, A is multiplied by $\frac{1}{2}$. In this case, the corresponding y-axis coefficients would be multiplied by 2, which is four times greater than those on the x-axis. This factor allows the cell to to maintain its isotropic material properties under stretched conditions. It should be noted that because of the damping coefficients are dependent on the cell's shape, the value of p_x will be recalculated at every time step. Fourth, this damping matrix only accounts for the dashpot network that lies along the x-axis in one cell. To account for the damping of the entire cell, we need to superimpose the y-axis coefficients.

$$\frac{1}{\Delta t}\begin{bmatrix} \boldsymbol{n_{0,x}} & \boldsymbol{n_{0,y}} & \boldsymbol{n_{1,x}} & \boldsymbol{n_{1,y}} & \boldsymbol{n_{2,x}} & \boldsymbol{n_{2,y}} & \boldsymbol{n_{3,x}} & \boldsymbol{n_{3,y}} \\ p_x & 0 & -p_x/3 & 0 & -p_x/3 & 0 & -p_x/3 & 0 \\ 0 & p_y & 0 & -p_y/3 & 0 & -p_y/3 & 0 & -p_y/3 \\ -p_x/3 & 0 & p_x & 0 & -p_x/3 & 0 & -p_x/3 & 0 \\ 0 & -p_y/3 & 0 & p_y & 0 & -p_y/3 & 0 & -p_y/3 \\ -p_x/3 & 0 & -p_x/3 & 0 & p_x & 0 & -p_x/3 & 0 \\ 0 & -p_y/3 & 0 & -p_y/3 & 0 & p_y & 0 & -p_y/3 \\ -p_x/3 & 0 & -p_x/3 & 0 & -p_x/3 & 0 & p_x & 0 \\ 0 & -p_y/3 & 0 & -p_y/3 & 0 & -p_y/3 & 0 & p_y \end{bmatrix} \begin{Bmatrix} u_{0,x}' \\ u_{0,y}' \\ u_{1,x}' \\ u_{1,y}' \\ u_{2,x}' \\ u_{2,y}' \\ u_{3,x}' \\ u_{3,y}' \end{Bmatrix} = \begin{Bmatrix} F_{0,x} \\ F_{0,y} \\ F_{1,x} \\ F_{1,y} \\ F_{2,x} \\ F_{2,y} \\ F_{3,x} \\ F_{3,y} \end{Bmatrix}$$

Eq. A-18

In this expanded form, each pair of columns corresponds to a particular dashpot, alternating the x and y-components. It can be seen that the matrix does not contain any crossterms. This is due to the fact that we have written the damping matrix in local x and y-coordinates. When this cell is superimposed into the global system of equations, the matrix will have to be mapped into global

coordinates as described earlier. The matrix elements containing zeroes will fill in with the appropriate values containing direction cosines.

In practice, the local coordinates are used to build a local damping matrix, but a global damping matrix is assembled to solve the entire system. This global matrix simply sums the damping contributions of each dashpot on the corresponding node. To better understand this, let us reconsider the damping matrix corresponding to the dashpot network lying along the x-axis in one cell.

$$c_{cell\ P}: \quad \begin{array}{cc} \textbf{local} & \\ & \textbf{global} \\ \boldsymbol{n_0} & \boldsymbol{g_5} \\ \boldsymbol{n_1} & \boldsymbol{g_2} \\ \boldsymbol{n_2} & \boldsymbol{g_1} \\ \boldsymbol{n_3} & \boldsymbol{g_6} \end{array} \begin{array}{c} \begin{array}{cccc} \boldsymbol{n_0} & \boldsymbol{n_1} & \boldsymbol{n_2} & \boldsymbol{n_3} \\ \boldsymbol{g_5} & \boldsymbol{g_2} & \boldsymbol{g_1} & \boldsymbol{g_6} \end{array} \\ \begin{bmatrix} p_x & -p_x/3 & -p_x/3 & -p_x/3 \\ -p_x/3 & p_x & -p_x/3 & -p_x/3 \\ -p_x/3 & -p_x/3 & p_x & -p_x/3 \\ -p_x/3 & -p_x/3 & -p_x/3 & p_x \end{bmatrix} \end{array} \qquad \text{Eq. A-19}$$

We renumber the nodes from their local numbering scheme to their global numbering scheme, referring to Figure A.2. A damping matrix for an identical cell, Q, can also be created and renumbered.

$$c_{cell\ Q}: \quad \begin{array}{cc} \textbf{local} & \\ & \textbf{global} \\ \boldsymbol{n_0} & \boldsymbol{g_4} \\ \boldsymbol{n_1} & \boldsymbol{g_3} \\ \boldsymbol{n_2} & \boldsymbol{g_2} \\ \boldsymbol{n_3} & \boldsymbol{g_5} \end{array} \begin{array}{c} \begin{array}{cccc} \boldsymbol{n_0} & \boldsymbol{n_1} & \boldsymbol{n_2} & \boldsymbol{n_3} \\ \boldsymbol{g_4} & \boldsymbol{g_3} & \boldsymbol{g_2} & \boldsymbol{g_5} \end{array} \\ \begin{bmatrix} q_x & -q_x/3 & -q_x/3 & -q_x/3 \\ -q_x/3 & q_x & -q_x/3 & -q_x/3 \\ -q_x/3 & -q_x/3 & q_x & -q_x/3 \\ -q_x/3 & -q_x/3 & -q_x/3 & q_x \end{bmatrix} \end{array} \qquad \text{Eq. A-20}$$

To assemble the global matrix, we reassign the matrix elements to their global matrix positions, summing any overlapping terms.

$$C_{global}:\quad \begin{array}{c} \\ \boldsymbol{g_0} \\ \boldsymbol{g_1} \\ \boldsymbol{g_2} \\ \boldsymbol{g_3} \\ \boldsymbol{g_4} \\ \boldsymbol{g_5} \\ \boldsymbol{g_6} \\ \boldsymbol{g_7} \end{array} \begin{array}{c} \begin{array}{cccccccc} \boldsymbol{g_0} & \boldsymbol{g_1} & \boldsymbol{g_2} & \boldsymbol{g_3} & \boldsymbol{g_4} & \boldsymbol{g_5} & \boldsymbol{g_6} & \boldsymbol{g_7} \end{array} \\ \begin{bmatrix} 0 & 0 & 0 & 0 & 0 & 0 & 0 & 0 \\ 0 & p_x & -\frac{p_x}{3} & 0 & 0 & -\frac{p_x}{3} & -\frac{p_x}{3} & 0 \\ 0 & -\frac{p_x}{3} & p_x + q_x & -\frac{q_x}{3} & -\frac{q_x}{3} & -\frac{p_x}{3} - \frac{q_x}{3} & -\frac{p_x}{3} & 0 \\ 0 & 0 & -\frac{q_x}{3} & q_x & -\frac{q_x}{3} & -\frac{q_x}{3} & 0 & 0 \\ 0 & 0 & -\frac{q_x}{3} & -\frac{q_x}{3} & q_x & -\frac{q_x}{3} & 0 & 0 \\ 0 & -\frac{p_x}{3} & -\frac{p_x}{3} - \frac{q_x}{3} & -\frac{q_x}{3} & -\frac{q_x}{3} & p_x + q_x & -\frac{p_x}{3} & 0 \\ 0 & -\frac{p_x}{3} & -\frac{p_x}{3} & 0 & 0 & -\frac{p_x}{3} & p_x & 0 \\ 0 & 0 & 0 & 0 & 0 & 0 & 0 & 0 \end{bmatrix} \end{array}$$

Eq. A-21

This example would need to include the y-component elements and each local damping matrix would be subject to rotation; nevertheless, the example above conveys the general process behind assembling a global damping matrix from local ones.

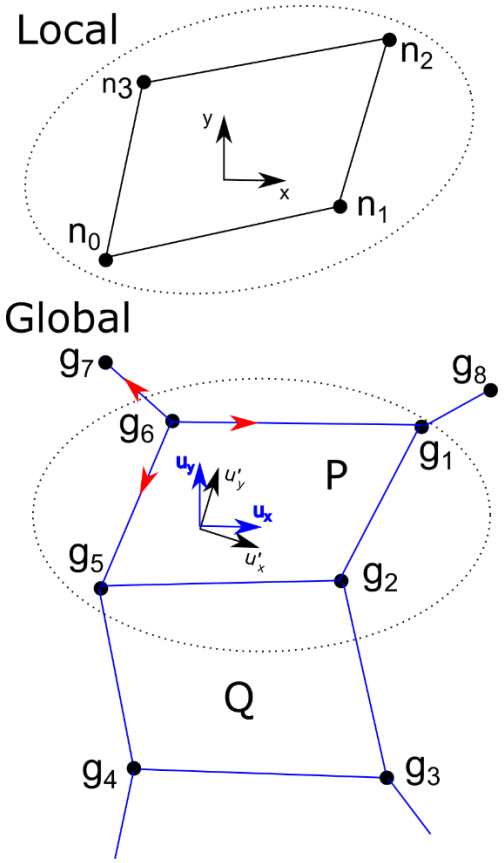

Figure A.2: Transformation of Coordinates. The local coordinates of cell P are mapped onto the global coordinates of the finite element system. Cell Q is adjacent to P. Red arrowhead indicate the cell-cell interfacial tensions: $\gamma_{61}, \gamma_{65}, \gamma_{67}$.

A.4 Apply Stress to Nodes

Applied stress is concentrated at the nodes to form a system of "equivalent forces," which is determined using the *principle of virtual work.* In the derivation in the previous section, we applied the principle of virtual work to a four-node system. The equation for potential energy was broken into two main components: potential energy due to strain, and work potential energy due to applied stress. Let us consider the second term in more detail. In a cellular finite element model, stress is applied to each cell as a constant tension acting along cell-cell interfaces. These tensions typically do not vary with time, and are assigned based on the interface type. The interface type is determined by the cell types of the two adjacent cells separated by the interface. Each node is assigned a net equivalent force, which is composed of the component forces from the three cell-cell interfaces that meet at the node. In the system of equations above, these equivalent forces were designated as, f.

$$f = \begin{Bmatrix} F_0 \\ F_1 \\ F_2 \\ F_3 \end{Bmatrix} \qquad \text{Eq. A-22}$$

Each equivalent force is the sum of the tension applied to the node. Since each node is a triple-point junction, there are three component forces for each equivalent force. The cell-cell interfacial tension, γ_{ij}, is designated to act between nodes i and j.

$$F_i = \sum_j \gamma_{ij} \qquad \text{Eq. A-23}$$

Rewriting Eq. A-17 with global node labels to include the specific tensions as shown in Figure A.2, we find the following system of equations for the x-components of cell P.

$$\frac{1}{\Delta t}\begin{bmatrix} p_x & -p_x/3 & -p_x/3 & -p_x/3 \\ -p_x/3 & p_x & -p_x/3 & -p_x/3 \\ -p_x/3 & -p_x/3 & p_x & -p_x/3 \\ -p_x/3 & -p_x/3 & -p_x/3 & p_x \end{bmatrix}\begin{Bmatrix} x_5 \\ x_2 \\ x_1 \\ x_6 \end{Bmatrix} = \begin{Bmatrix} \gamma_{52,x} + \gamma_{56,x} + \gamma_{54,x} \\ \gamma_{21,x} + \gamma_{25,x} + \gamma_{23,x} \\ \gamma_{18,x} + \gamma_{16,x} + \gamma_{12,x} \\ \gamma_{61,x} + \gamma_{67,x} + \gamma_{65,x} \end{Bmatrix} \quad \text{Eq. A-24}$$

Once the system of equations have been set up in local coordinates for each cell, including both x and y-components, the full local system is rotated and assembled into a global system of equations. This final form is then read to be solved for the unknown displacements at each timestep.

A.5 Solve the System of Equations with Area Constraints

To determine the displacement of each node, the system of equations is solved using Lagrange multipliers. Initially, we used the principle of virtual work to build a statement of the potential energy for the system. We then used the principle of minimal potential energy to extremize the potential energy and assemble a system of equations describing the forces at play. We now appeal to methods from variational calculus to apply a constraint on the system (Felippa, C. A., 2004; Jensen, S., 2015). In general, the viscous properties of the cell elements are not enough to maintain constant cell size. We must impose an area constraint to ensure the cells do not grow or shrink, but rather simply change shape. In our system of two dimensional polygonal cell elements, the change in area is determined by the node positions (Weisstein, Eric W.).

$$\begin{aligned} g(\boldsymbol{x_i}, t) &= Area_f - Area_i \\ &= \frac{1}{2}\left(\begin{vmatrix} x_0 & x_1 \\ y_0 & y_1 \end{vmatrix} + \begin{vmatrix} x_1 & x_2 \\ y_1 & y_2 \end{vmatrix} + \cdots + \begin{vmatrix} x_n & x_0 \\ y_n & y_0 \end{vmatrix}\right)_f \\ &\quad -\frac{1}{2}\left(\begin{vmatrix} x_0 & x_1 \\ y_0 & y_1 \end{vmatrix} + \begin{vmatrix} x_1 & x_2 \\ y_1 & y_2 \end{vmatrix} + \cdots + \begin{vmatrix} x_n & x_0 \\ y_n & y_0 \end{vmatrix}\right)_i \end{aligned} \quad \text{Eq. A-25}$$

We set $g(\boldsymbol{x_i}, t) = 0$. This area constraint is imposed on the system using Lagrange multipliers. Consider the potential energy form of our system described in Eq. A-9. We can

consider this energy to be a Lagrangian as described in classical mechanics, and we append the constraint by adding zero (Jensen, S., 2015).

$$L(\boldsymbol{x_i}, \dot{\boldsymbol{x}}_{\boldsymbol{i}}, t) = \Pi \quad \text{Eq. A-26}$$

$$L_\lambda(\boldsymbol{x_i}, \dot{\boldsymbol{x}}_{\boldsymbol{i}}, \lambda, t) = L(\boldsymbol{x_i}, \dot{\boldsymbol{x}}_{\boldsymbol{i}}, t) + \lambda(t) g(\boldsymbol{x_i}, t) \quad \text{Eq. A-27}$$

We can now extremize the constrained energy terms using the Euler-Lagrange equations (Jensen, S., 2015).

$$0 = \frac{\delta L_\lambda}{\delta x_i} - \frac{d}{dt}\frac{\delta L_\lambda}{\delta \dot{x}_i} \quad \text{Eq. A-28}$$

When we discretize the time steps in the system, the dependence of L_λ on $\dot{\boldsymbol{x}}_{\boldsymbol{i}}$ vanishes, removing the second term of this Euler-Lagrange equations. Thus discretization reduces our system of equations to the first term.

$$0 = \frac{\delta \Pi}{\delta x_i} + \lambda(t)\frac{\delta g}{\delta x_i} \quad \text{Eq. A-29}$$

Taking the partial derivatives of the Lagrangian with respect to each displacement in the x and y-directions, we resolve an expanded version of the System of Eq. A-14, i.e.

$$F_{0,x} = \frac{1}{\Delta t}\left[\left(p_x x_0 - \frac{p_x}{3}x_1 - \frac{p_x}{3}x_2 - \frac{p_x}{3}x_3\right) + \lambda\left(\frac{1}{2}y_1 + \frac{1}{2}y_3\right)\right] \quad \text{Eq. A-30}$$

$$F_{0,y} = \ \ldots$$

$$\vdots$$

We can express this system of equations in matrix form. By adding the terms for the Lagrange multipliers, we build a multiplier-augmented system (Felippa, C. A., 2004). We append the vector, $\boldsymbol{\lambda}$, to the vector of unknown displacements through a process called adjunction.

$$\frac{1}{\Delta t}\begin{bmatrix} \boldsymbol{C} & \boldsymbol{A} \\ \boldsymbol{A^T} & \boldsymbol{0} \end{bmatrix} \begin{Bmatrix} u'_{0,x} \\ u'_{0,y} \\ u'_{1,x} \\ u'_{1,y} \\ u'_{2,x} \\ u'_{2,y} \\ u'_{3,x} \\ u'_{3,y} \\ \boldsymbol{\lambda} \end{Bmatrix} = \begin{Bmatrix} F_{0,x} \\ F_{0,y} \\ F_{1,x} \\ F_{1,y} \\ F_{2,x} \\ F_{2,y} \\ F_{3,x} \\ F_{3,y} \\ \boldsymbol{0} \end{Bmatrix} \qquad \text{Eq. A-31}$$

where $\boldsymbol{\lambda} = \left[\lambda_{0,x},\ \lambda_{0,y},\ \lambda_{1,x},\ \lambda_{1,y},\ \lambda_{2,x},\ \lambda_{2,y},\ \lambda_{3,x},\ \lambda_{3,y}\right]^T$. The components of $\boldsymbol{\lambda}$ are functions of the corresponding displacement, i.e. $\lambda_{0,x} = \lambda(u'_{0,x})$. The force vector has also been appended by the null vector, $\boldsymbol{0}$. Finally, the damping matrix has been augmented by the vector, $\boldsymbol{A}$, which contains the coefficients of the Lagrangian terms, as shown in the fully-expanded augmented damping matrix below. Here, the blue shading marks $\boldsymbol{A}$ and $\boldsymbol{A^T}$.

$$\begin{bmatrix} \boldsymbol{C} & \boldsymbol{A} \\ \boldsymbol{A^T} & \boldsymbol{0} \end{bmatrix} =$$ Eq. A-32

$\boldsymbol{n_{0,x}}$	$\boldsymbol{n_{0,y}}$	$\boldsymbol{n_{1,x}}$	$\boldsymbol{n_{1,y}}$	$\boldsymbol{n_{2,x}}$	$\boldsymbol{n_{2,y}}$	$\boldsymbol{n_{3,x}}$	$\boldsymbol{n_{3,y}}$	$\boldsymbol{n_{0,x}}$	$\boldsymbol{n_{0,y}}$	$\boldsymbol{n_{1,x}}$	$\boldsymbol{n_{1,y}}$	$\boldsymbol{n_{2,x}}$	$\boldsymbol{n_{2,y}}$	$\boldsymbol{n_{3,x}}$	$\boldsymbol{n_{3,y}}$
p_x	0	$-\frac{p_x}{3}$	0	$-\frac{p_x}{3}$	0	$-\frac{p_x}{3}$	0	0	0	0	$\frac{1}{2}$	0	0	0	$-\frac{1}{2}$
0	p_y	0	$-\frac{p_y}{3}$	0	$-\frac{p_y}{3}$	0	$-\frac{p_y}{3}$	0	0	$-\frac{1}{2}$	0	0	0	$\frac{1}{2}$	0
$\frac{-p_x}{3}$	0	p_x	0	$-\frac{p_x}{3}$	0	$-\frac{p_x}{3}$	0	0	$-\frac{1}{2}$	0	0	0	$\frac{1}{2}$	0	0
0	$\frac{-p_y}{3}$	0	p_y	0	$-\frac{p_y}{3}$	0	$-\frac{p_y}{3}$	$\frac{1}{2}$	0	0	0	$-\frac{1}{2}$	0	0	0
$\frac{-p_x}{3}$	0	$-\frac{p_x}{3}$	0	p_x	0	$-\frac{p_x}{3}$	0	0	0	0	$-\frac{1}{2}$	0	0	0	$\frac{1}{2}$
0	$-\frac{p_y}{3}$	0	$-\frac{p_y}{3}$	0	p_y	0	$-\frac{p_y}{3}$	0	0	$\frac{1}{2}$	0	0	0	$-\frac{1}{2}$	0
$\frac{-p_x}{3}$	0	$-\frac{p_x}{3}$	0	$-\frac{p_x}{3}$	0	p_x	0	0	$\frac{1}{2}$	0	0	0	$-\frac{1}{2}$	0	0
0	$\frac{-p_y}{3}$	0	$-\frac{p_y}{3}$	0	$-\frac{p_y}{3}$	0	p_y	$-\frac{1}{2}$	0	0	0	$\frac{1}{2}$	0	0	0
0	0	0	$\frac{1}{2}$	0	0	0	$-\frac{1}{2}$	0	0	0	0	0	0	0	0
0	0	$-\frac{1}{2}$	0	0	0	$\frac{1}{2}$	0	0	0	0	0	0	0	0	0
0	$-\frac{1}{2}$	0	0	0	$\frac{1}{2}$	0	0	0	0	0	0	0	0	0	0
$\frac{1}{2}$	0	0	0	$-\frac{1}{2}$	0	0	0	0	0	0	0	0	0	0	0
0	0	0	$-\frac{1}{2}$	0	0	0	$\frac{1}{2}$	0	0	0	0	0	0	0	0
0	0	$\frac{1}{2}$	0	0	0	$-\frac{1}{2}$	0	0	0	0	0	0	0	0	0
0	$\frac{1}{2}$	0	0	0	$-\frac{1}{2}$	0	0	0	0	0	0	0	0	0	0
$-\frac{1}{2}$	0	0	0	$\frac{1}{2}$	0	0	0	0	0	0	0	0	0	0	0

We can quickly resolve the physical constraints applied to each node by considering the bottom left blue section of the multiplier-augmented system, $\frac{1}{\Delta t}\boldsymbol{A^T u} = \boldsymbol{0}$. These eight equations reduce to four identities by symmetry.

$$u'_{0,x} = u'_{2,x} \qquad u'_{0,y} = u'_{2,y}$$
$$u'_{1,x} = u'_{3,x} \qquad u'_{1,y} = u'_{3,y}$$ Eq. A-33

In this case, where we are testing a quadrilateral cell element, the area constraint has effectively connected nodes 0 to 2 and 1 to 3 with a rigid link. Solving the top half of the multiplier-augmented system, we find

$$u'_{0,x} = \frac{\Delta t}{2p_x}\left(F_{0,x} - F_{1,x} + F_{2,x} - F_{3,x}\right) + u'_{1,x}$$
$$u'_{2,x} = \frac{\Delta t}{2p_x}\left(F_{0,x} - F_{1,x} + F_{2,x} - F_{3,x}\right) + u'_{1,x}$$
$$u'_{3,x} = u'_{1,x}$$

Eq. A-34

and a similar system of equations for the y-components. This solves the quadrilateral cell system for nodal displacements given the applied cell-cell interfacial tensions and the damping network. One remaining question is what do the Lagrange multipliers physically mean? They can be considered constraint forces. The extra force applied to the nodes in order for the constraints to be enforced on the nodes. Since, they ensure the cell maintains a constant area, these extra nodal forces act as local components of the cell's internal pressure. Brodland considers this internal pressure to represent the incompressibility of the cytoplasm and the in-plane isotropic internal stress of the cortical cytoskeleton (M. Shane Hutson et al., 2009).

APPENDIX B

TABLE OF CELL-CELL INTERFACIAL TENSIONS

	γ_{GBGB}	γ_{GBAS}	γ_{ASAS}	γ_{HdGB}	γ_{HdAS}	γ_{HdHd}	γ_{CutGB}	γ_{CutAS}	γ_{CutHd}	γ_{CutCut}	Figure
No Tension	0	0	0	0	0	0					2A
Equal Tension	10	10	10	10	10	10					2A
Base Model	10	20	10	10	40	20					1C, 2A
Increasing GBAS x4	10	40	10	10	80	20					2A,B
Increasing GBAS x8	10	80	10	10	160	20					2A
Increasing ASAS x2	10	20	20	10	40	20					2A
Increasing ASAS x4	10	20	40	10	40	20					2A,C
Increasing ASAS x8	10	20	80	10	40	20					2A
Increasing ASAS x2, Double GBAS	10	40	20	10	80	20					2A
Increasing ASAS x4, Double GBAS	10	80	40	10	160	20					2A,D
Increasing ASAS x8, Double GBAS	10	160	80	10	320	20					2A
Increasing GBGB x2	20	20	10	20	40	40					2A
Increasing GBGB x4	40	20	10	40	40	80					2A,E
Increasing GBGB x8	80	20	10	80	40	160					2A
Increasing GBGB x2, Double GBAS	20	40	10	20	80	40					2A
Increasing GBGB x4, Double GBAS	40	80	10	40	160	80					2A,F
Increasing GBGB x8, Double GBAS	80	160	10	80	320	160					2A
Polarized GBGB	2 Perp, 8 Para	20	10	10	40	20					3A
3100 Cell Mesh	2	12	10	8	12	2					3B
Ramped ASAS	10	20	0 - 4.4	10	40	20					3C
Aspect ratio tests (m.a.r. =7.0, 3.6, 1.3)	10	20	10	10	40	20					4A-C
Aspect ratio rescue (m.a.r. =1.3)	10	100	10	10	200	20					4D
Mutants with AS removed	10	20	10	10	40	20	10	5	20	0	5A-C
Rescue of AS Mutant with Polarized GB	2 Perp, 8 Para	20	10	10	40	20	10	5	20	0	5D

APPENDIX C

MATERIALS AND METHODS FOR CHAPTERS CHAPTER 4 AND CHAPTER 6

C.1 The Model - Assigning Cell-Cell Interfacial Tensions

We choose the cell-cell edge tensions as described in Chapters 4 and 6. Appendix B expands the tension chart in Figure 4.2A to include the three types of head tension: γ_{HdGB}, γ_{HdAS}, γ_{HdHd}. Additionally, we include special cases of tension assigment. Polarization is added to γ_{GBGB} based on the orientation of a cell edge with respect to the germband-amnioserosa border:

$$\gamma_{GBGB,Pol} = \gamma_{GBGB}\,(1 - x\cos(2\theta)) \qquad \text{Eq. C-1}$$

where x scales the tension along the edges according to the angle θ, i.e. $x = 0.8$ and $\theta = 90°$ redistribute the edge tension, γ_{GBGB}, around the cell so that 80% more tension lies along edges that are parallel to the border and 80% less tension lies along perpendicular edges. The 3100 cell mesh is assigned tensions as described in the text. The ramped γ_{ASAS} increases linearly with time steps, τ:

$$\gamma_{ASAS,\tau} = \gamma_{ASAS,\tau=0} + r\tau \qquad \text{Eq. C-2}$$

where r is the scaling factor for the ramp. We find $r = 0.1333$, such that $0 \leq \gamma_{ASAS} \leq 4.4$ over 33 time steps, gives the most similar kinematics to *in vivo* data. Mutants and rescues are assigned an extra cell type to simulate the apoptotic or cut amnioserosa cells. This additional cell type adds four cell-cell edge types for tension assignments. These are listed as γ_{CutGB}, γ_{CutAS}, γ_{CutHd}, and γ_{CutCut} in Appendix B. In every simulation, all cells are given equal viscosity and their

volume constraint is consistent with the initial geometry of the mesh. With these parameters defined, the finite element engine is allowed to run, maintaining a constant active tension on each cell-cell edge for the duration of the simulation.

C.2 The Model - Software

Initial geometric configurations for each mesh are designed and produced using Mathematica 10 (*Mathematica*, 2015) as described in previous sections. The finite element engine is custom-built to handle an ellipsoid last based on previous finite element engines published by (G. W. Brodland & Chen, 2000; G. W. Brodland et al., 2007). Visualization of the cellular finite element simulations is performed by a custom-built simulation viewer, ChiChi3D.

C.3 Experimental Methods – Time-lapse Imaging and Image Analysis

To track the progression of germband retraction in *Drosophila melanogaster*, we use flies with fluorescent labeling, ubi-DE-Cad-GFP (*Drosophila* Genetic Research Center, Kyoto, Japan), which ubiquitously expresses E-Cadherin-GFP to label adherens junctions between cells (Oda & Tsukita, 2001). Time-lapse confocal imaging of E-cadherin-GFP is performed using 40x, 1.3NA oil-immersion objectives on a laser scanning confocal microscope (Axiovert-135TV/LSM-410; Carl Zeiss, Thornwood, NY). Additional whole-embryo Selective Plane Illumination Microscopy (SPIM) data is used from the following sources: Tomer et al. (2012) (supplementary videos 2, 3, and 5) and Truong et al. (2011) (supplementary video 4). To account for differences in developmental timing due to variations in embryos and experimental conditions, the raw time for the Truong et al. (2011) data set and our time-lapse images (shown in Figure 4.1A) are scaled by factors of 1.68 and 0.79, respectively. Measurements of

archicephalon and telson positions are found by comparing the corresponding fiducial markers (position of apical contact between the amnioserosa and the head or telson) to the length of the embryo. This analysis is performed using Fiji (Schindelin et al., 2012). For measurements of amnioserosa cell morphology, we segment images of E-cadherin-GFP labeled amnioserosa cells (n= 49-104 cells per time bin from 4 embryos) using a watershed-based segmentation software, Seedwater Segmenter (Mashburn, Lynch, Ma, & Hutson, 2012), from which we extract information on aspect ratio. Here, time is scaled such that developmental progression as measured by telson position is matched across all embryos. Aspect ratio data is then binned into 12 min intervals, such that 12 bins span the adjusted 130 min developmental time.

APPENDIX D

EXPERIMENTAL PROCEDURES FOR CHAPTER CHAPTER 5

D.1 Fly strains

We used several transgenic strains of *Drosophila melanogaster* expressing fluorescent reporters: ubi-DE-Cad-GFP (*Drosophila* Genetic Research Center, Kyoto, Japan), which ubiquitously expresses E-Cadherin-GFP to label epithelial cell junctions (Oda & Tsukita, 2001); sGMCA-3.1 or moesin-GFP (3rd chromosome insertion; gift from DP Kiehart), which ubiquitously expresses a fusion of GFP and the actin-binding domain of moesin to visualize actin filaments (K. A. Edwards et al., 1997; Kiehart et al., 2000); E-Cad:GFP; sqh:mCherry (gift from A. Jacinto, Instituto de Medicina Molecular, Lisbon, Portugal) for visualization of epithelial cell junctions and myosin localization; Gap43-mCherry (gift from Adam Martin, Massachusetts Institute of Technology) to label cell membranes (Martin, Gelbart, Fernandez-Gonzalez, Kaschube, & Wieschaus, 2010); and UAS-Apoliner (Bardet et al., 2008; Bloomington Drosophila Stock Center, Bloomington, Indiana) crossed with UH1-GAL4 (Wodarz, Hinz, Engelbert, & Knust, 1995; Bloomington Drosophila Stock Center) to ubiquitously express an mRFP-eGFP reporter of apoptosis-associated caspase activity.

D.2 Sample preparation, heat shock and live imaging

Embryos were collected on grape agar plates with yeast paste. Collections were for one hour, after which embryos were left to develop at room temperature for two hours, dechorionated using a 50% bleach solution, and mounted on a coverslip using embryo glue. Mounted embryos were surrounded with wet strips of Whatman filter paper (GE Healthcare, Little Chalfont,

Buckinghamshire, UK) and covered with an oxygen-permeable membrane (YSI, Yellow Spring, OH) to prevent dehydration while allowing sufficient O2 exchange.

Embryos to be heat shocked were monitored under a bright-field microscope (Axiovert-135TV, Carl Zeiss, Thornwood, NY). As soon as the embryo's cephalic furrow formed, the slide was floated on top of a 38 °C water bath. After 30 minutes, the slide was removed from the bath and allowed to cool at room temperature.

Fluorescent imaging was performed using 40x, 1.3NA oil-immersion objectives on either a laser scanning confocal microscope (Axiovert-135TV/LSM-410; Carl Zeiss, Thornwood, NY) or a spinning disk confocal microscope (WaveFX-X1, Quorum Technologies, Ontario, Canada built onto an Eclipse Ti, Nikon Instruments, Melville, NY).

For measurements of cell morphology, we segmented images of E-cadherin-GFP amnioserosa cells using a watershed-based segmentation software, Seedwater Segmenter (Mashburn et al., 2012). From the segmentation we extracted information on area, perimeter, and aspect ratio.

D.3 DAPI and Immunostaining

Embryos were fixed for 4 minutes or 20 minutes in a 1:1 mixture of heptane and either 16% or 3.7% formaldehyde in phosphate buffered saline (PBS) for assessment of nuclear morphology or E-cadherin levels, respectively. The formaldehyde solution was removed, and embryos were then devitellinized in a 1:1 methanol:heptane solution by vigorous shaking for 30 seconds. Embryos were washed and stored overnight in methanol at 4 °C.

Experiments measuring cell and nuclear morphology around heat-shock-induced holes followed methods similar to Sullivan, Ashburner, and Hawley (2000). Fixed embryos were

rehydrated for 15 minutes in PBTA (mixture of PBS, bovine serum albumin, sodium azide, and Triton-X 100); and doubly immunostained: a primary antibody for α-spectrin (3A9 α-spectrin antibody solution, Developmental Studies Hybridoma Bank (DHSB), University of Iowa) with a secondary donkey anti-mouse conjugated with AlexaFluor 488 (Molecular Probes, Life Technologies, Grand Island, NY); and a primary antibody for β-integrin (CF.6G11 integrin antibody solution, DSHB) with a secondary goat anti-mouse IgG2b conjugated with AlexaFluor 568 (Molecular Probes). Immunostained embryos were washed in PBTA before adding 100X DAPI solution for five minutes. Embryos were then washed extensively in PBTA, followed by several washes in PBS and mounting in a glycerol-based medium for imaging.

Experiments assessing junctional E-cadherin levels followed methods similar to Goldenberg and Harris (2013). These embryos were rehydrated for 1.5 hours in NGS block solution (PBS with 0.1% Triton-X100 (PBT) plus 1% normal goat serum (NGS)) and doubly immunostained: a primary antibody for β-catenin (mouse anti-armadillo, #N27A1, DSHB) with a secondary goat anti-mouse IgG2A conjugated to Cy3 (Jackson ImmunoResearch, West Grove, PA); and a primary antibody for DE-cadherin (rat anti-DE-cadherin, #DCAD2, DSHB) with a secondary donkey anti-rat conjugated to FITC (Jackson ImmunoResearch). Immunostained embryos were washed in PBT (three 10-min washes), incubated in Vectashield with DAPI (Vector Laboratories, Inc., Burlingame, CA), and mounted on slides for imaging.

D.4 Laser ablation and analysis

Laser hole drilling was conducted on a custom laser-microsurgery system combining the above-mentioned laser scanning confocal microscope and a Q-switched Nd:YAG laser (Continuum Minilite II, Santa Clara, CA). All holes were created using a single pulse (5 ns

pulsewidth) of the laser's 3rd harmonic (355 nm wavelength) at 2-3× threshold. For hole drilling in intact tissues (control and heat-shocked embryos), pre- and post-ablation images were collected at a spatial scale of 0.649 μm/pixel and a temporal rate of 1 frame per second. The post-ablation deformation fields were estimated in ImageJ (NIH, Bethesda, MD) using the plugin bUnwarpJ (Arganda-Carreras et al., 2006). These deformation fields were applied to a circle centered on each wound having an initial radius of 8 μm. The time-dependent area of each deformed circle (A) was used to calculate the post-ablation radial strain as $\varepsilon_r(t) = \sqrt{A(t)/A(t_0)} - 1$. For hole drilling inside heat-shock-induced holes, pre- and post-ablation images were collected at a spatial scale of 0.325 μm/pixel using an exposure time of 4 s per frame and a 1-s delay between frames. A line was drawn across the width of the heat-shock-induced hole so that it intersected the laser hole drilling target. The time-dependent length (L) of each line was used to calculate the post-ablation linear strain as $\varepsilon_L(t) = L(t)/L(t_0) - 1$.

REFERENCES

Abbott, M. K., & Lengyel, J. A. (1991). Embryonic head involution and rotation of male terminalia require the Drosophila locus head involution defective. *Genetics, 129*(3), 783-789.

Abrams, J. M., White, K., Fessler, L. I., & Steller, H. (1993). Programmed cell death during *Drosophila* embryogenesis. *Development, 117*, 29-43.

Allena, R., Mouronval, A. S., & Aubry, D. (2010). Simulation of multiple morphogenetic movements in the Drosophila embryo by a single 3D finite element model. *J Mech Behav Biomed Mater, 3*(4), 313-323. doi:10.1016/j.jmbbm.2010.01.001

Allena, R., Munoz, J. J., & Aubry, D. (2013). Diffusion-reaction model for Drosophila embryo development. *Computer Methods in Biomechanics and Biomedical Engineering, 16*(3), 235-248. doi:10.1080/10255842.2011.616944

Almeida, L., Bagnerini, P., Habbal, A., Noselli, S., & Serman, F. (2011). A mathematical model for dorsal closure. *Journal of Theoretical Biology, 268*(1), 105-119. doi:10.1016/j.jtbi.2010.09.029

Arganda-Carreras, I., Sorzano, C. O. S., Marabini, R., Carazo, J.-M., Ortiz-de Solorzano, C., & Kybic, J. (2006). *Consistent and Elastic Registration of Histological Sections using Vector-Spline Regularization.* Paper presented at the CVAMIA: Computer Vision Approaches to Medical Image Analysis.

Bardet, P. L., Kolahgar, G., Mynett, A., Miguel-Aliaga, I., Briscoe, J., Meier, P., & Vincent, J. P. (2008). A fluorescent reporter of caspase activity for live imaging. *Proceedings of the National Academy of Sciences of the United States of America, 105*(37), 13901-13905. doi:10.1073/pnas.0806983105

Belegundu, A. D., & Chandrupatla, T. R. (2002). Introduction to finite elements in engineering: Prentice-Hall, Upper Saddle River, NJ.

Blanchard, G. B., Kabla, A. J., Schultz, N. L., Butler, L. C., Sanson, B., Gorfinkiel, N., . . . Adams, R. J. (2009). Tissue tectonics: morphogenetic strain rates, cell shape change and intercalation. *Nat Methods, 6*(6), 458-464. doi:10.1038/nmeth.1327

Blankenship, J. T., Backovic, S. T., Sanny, J. S. P., Weitz, O., & Zallen, J. A. (2006). Multicellular rosette formation links planar cell polarity to tissue morphogenesis. *Developmental Cell, 11*(4), 459-470. Retrieved from <Go to ISI>://000241123300008

Bloor, J. W., & Kiehart, D. P. (2002). Drosophila RhoA regulates the cytoskeleton and cell-cell adhesion in the developing epidermis. *Development, 129*(13), 3173-3183. Retrieved from <Go to ISI>://WOS:000176965400014

Brodland, G., Chen, D., & Veldhuis, J. (2006). A cell-based constitutive model for embryonic epithelia and other planar aggregates of biological cells. *International Journal of Plasticity, 22*(6), 965-995. doi:10.1016/j.ijplas.2005.05.002

Brodland, G. W. (2002). The differential interfacial tension hypothesis (DITH): a comprehensive theory for the self-rearrangement of embryonic cells and tissues. *Journal of Biomechanical Engineering-Transactions of the Asme, 124*(2), 188-197. doi:10.1115/1.1449491

Brodland, G. W. (2004). Computational modeling of cell sorting, tissue engulfment, and related phenomena: A review. *Applied Mechanics Reviews, 57*(1), 47. doi:10.1115/1.1583758

Brodland, G. W., & Chen, H. H. (2000). The mechanics of cell sorting and envelopment. *Journal of Biomechanics, 33*(7), 845-851. Retrieved from <Go to ISI>://WOS:000087392900007

Brodland, G. W., & Veldhuis, J. H. (2012). Assessing the mechanical energy costs of various tissue reshaping mechanisms. *Biomechanics and Modeling in Mechanobiology, 11*(8), 1137-1147. doi:10.1007/s10237-012-0411-x

Brodland, G. W., Viens, D., & Veldhuis, J. H. (2007). A new cell-based FE model for the mechanics of embryonic epithelia. *Computer Methods in Biomechanics and Biomedical Engineering, 10*(2), 121-128. doi:10.1080/10255840601124704

Brody, T. (1999). The Interactive Fly: gene networks, development and the Internet. *Trends Genet, 15*(8), 333-334.

Chen, H. H., & Brodland, G. W. (2000). Cell-level finite element studies of viscous cells in planar aggregates. *Journal of Biomechanical Engineering-Transactions of the Asme, 122*(4), 394-401. doi:10.1115/1.1286563

Clarke, M. E., & Gibbard, W. B. (2003). Overview of fetal alcohol spectrum disorders for mental health professionals. *Can Child Adolesc Psychiatr Rev, 12*(3), 57-63.

Conte, V., Munoz, J. J., Baum, B., & Miodownik, M. (2009). Robust mechanisms of ventral furrow invagination require the combination of cellular shape changes. *Phys Biol, 6*(1), 016010. doi:10.1088/1478-3975/6/1/016010

Conte, V., Munoz, J. J., & Miodownik, M. (2008). A 3D finite element model of ventral furrow invagination in the Drosophila melanogaster embryo. *J Mech Behav Biomed Mater, 1*(2), 188-198. doi:10.1016/j.jmbbm.2007.10.002

Conte, V., Ulrich, F., Baum, B., Munoz, J., Veldhuis, J., Brodland, W., & Miodownik, M. (2012). A biomechanical analysis of ventral furrow formation in the Drosophila melanogaster embryo. *PLoS One, 7*(4), e34473. doi:10.1371/journal.pone.0034473

Crews, S. M., McCleery, W. T., & Hutson, M. S. (2016). Pathway to a phenocopy: Heat stress effects in early embryogenesis. *Developmental Dynamics, 245*(3), 402-413. doi:10.1002/dvdy.24360

Delpisheh, A., Topping, J., Reyad, M., Tang, A., & Brabin, B. J. (2008). Prenatal alcohol exposure, CYP17 gene polymorphisms and fetal growth restriction. *European Journal of Obstetrics, Gynecology, and Reproductive Biology, 138*(1), 49-53. doi:10.1016/j.ejogrb.2007.08.006

Denton, D., & Kumar, S. (2015). Terminal Deoxynucleotidyl Transferase (TdT)-Mediated dUTP Nick-End Labeling (TUNEL) for Detection of Apoptotic Cells in Drosophila. *Cold Spring Harb Protoc, 2015*(6), pdb prot086199. doi:10.1101/pdb.prot086199

Dunn, A. R., & Price, A. (2015). Energetics and forces in living cells. *Physics Today, 68*(2), 27-32. doi:10.1063/pt.3.2686

Dura, J.-M., & Santamaria, P. (1983). Heat Shock-Induced Phenocopies: Cis-Regulation of the Bithorax Complex in *Drosophila melanogaster*. *Molecular Genetics and Genomics, 189*, 235-239.

Eberlein, S. (1986). Stage Specific Embryonic Defects Following Heat Shock in *Drosophila*. *Developmental Genetics, 6*(179-197).

Edwards, K. A., Demsky, M., Montague, R. A., Weymouth, N., & Kiehart, D. P. (1997). GFP-moesin illuminates actin cytoskeleton dynamics in living tissue and demonstrates cell shape changes during morphogenesis in Drosophila. *Developmental Biology, 191*(1), 103-117. Retrieved from <Go to ISI>://A1997YG86600009

Edwards, M. J. (1986). Hyperthermia as a teratogen: a review of experimental studies and their clinical significance. *Teratogenesis, Carcinogenesis, and Mutagenesis, 6*(6), 563-582. Retrieved from http://www.ncbi.nlm.nih.gov/pubmed/2881371

Edwards, M. J. (1998). Apoptosis, the heat shock response, hyperthermia, birth defects, disease and cancer. Where are the common links? *Cell Stress and Chaperones, 3*(4), 213-220.

Farhadifar, R., Röper, J.-C., Aigouy, B., Eaton, S., & Jülicher, F. (2007). The Influence of Cell Mechanics, Cell-Cell Interactions, and Proliferation on Epithelial Packing. *Current Biology, 17*, 2095-2104.

Felippa, C. A. (2004). "Chapter 9: MultiFreedom Constraints II." *Introduction to finite element methods.* Course Notes, Department of Aerospace Engineering Sciences, University of Colorado at Boulder. Retrieved from http://www.colorado.edu/engineering/CAS/courses.d/IFEM.d/IFEM.Ch09.d/IFEM.Ch09.pdf

Fernandez-Gonzalez, R., Simoes Sde, M., Roper, J. C., Eaton, S., & Zallen, J. A. (2009). Myosin II dynamics are regulated by tension in intercalating cells. *Developmental Cell, 17*(5), 736-743. doi:10.1016/j.devcel.2009.09.003

Foe, V. E., Odell, G. M., & Edgar, B. A. (1993). Mitosis and Morphogenesis in the Drosophila embryo. In M. Bate & A. Martinez-Arias (Eds.), *The Development of Drosophila melanogaster* (pp. 149-300). Long Island, NY: Cold Spring Harbor Press.

Frank, L. H., & Rushlow, C. (1996). A group of genes required for maintenance of the amnioserosa tissue in Drosophila. *Development, 122*(5), 1343-1352. Retrieved from <Go to ISI>://WOS:A1996UM55800001

Goldenberg, G., & Harris, T. J. (2013). Adherens junction distribution mechanisms during cell-cell contact elongation in Drosophila. *PLoS One, 8*(11), e79613. doi:10.1371/journal.pone.0079613

GoldmanLevi, R., Miller, C., Greenberg, G., Gabai, E., & Zak, N. B. (1996). Cellular pathways acting along the germband and in the amnioserosa may participate in germband retraction of the Drosophila melanogaster embryo. *International Journal of Developmental Biology, 40*(5), 1043-1051. Retrieved from <Go to ISI>://WOS:A1996VR17500012

Grether, M. E., Abrams, J. M., Agapite, J., White, K., & Steller, H. (1995). The head involution defective gene of Drosophila melanogaster functions in programmed cell death. *Genes & Development, 9*(14), 1694-1708.

Grumbling, G., & Strelets, V. (2006). FlyBase: anatomical data, images and queries. *Nucleic Acids Res, 34*(Database issue), D484-488. doi:10.1093/nar/gkj068

Gu, Y., Forostyan, T., Sabbadini, R., & Rosenblatt, J. (2011). Epithelial cell extrusion requires the sphingosine-1-phosphate receptor 2 pathway. *Journal of Cell Biology, 193*(4), 667-676. doi:10.1083/jcb.201010075

Harden, N., Loh, H. Y., Chia, W., & Lim, L. (1995). DOMINANT INHIBITORY VERSION OF THE SMALL GTP-BINDING PROTEIN RAC DISRUPTS CYTOSKELETAL STRUCTURES AND INHIBITS DEVELOPMENTAL CELL-SHAPE CHANGES IN DROSOPHILA. *Development, 121*(3), 903-914. Retrieved from <Go to ISI>://WOS:A1995QN06700025

Hartenstein, V., & Hartenstein, V. (1993). *Atlas of Drosophila development*.

Hay, B. A., & Guo, M. (2006). Caspase-dependent cell death in Drosophila. *Annual Review of Cell and Developmental Biology, 22*, 623-650. doi:10.1146/annurev.cellbio.21.012804.093845

Hay, B. A., Wolff, T., & Rubin, G. M. (1994). Expression of baculovirus P35 prevents cell death in Drosophila. *Development, 120*(8), 2121-2129.

Hocevar Brezavscek, A., Rauzi, M., Leptin, M., & Ziherl, P. (2012). A model of epithelial invagination driven by collective mechanics of identical cells. *Biophys J, 103*(5), 1069-1077. doi:10.1016/j.bpj.2012.07.018

Homem, C. C., & Peifer, M. (2008). Diaphanous regulates myosin and adherens junctions to control cell contractility and protrusive behavior during morphogenesis. *Development, 135*(6), 1005-1018. doi:10.1242/dev.016337

Honda, H., Nagai, T., & Tanemura, M. (2008). Two different mechanisms of planar cell intercalation leading to tissue elongation. *Developmental Dynamics, 237*(7), 1826-1836. doi:10.1002/dvdy.21609

Houssin, E., Tepass, U., & Laprise, P. (2015). Girdin-mediated interactions between cadherin and the actin cytoskeleton are required for epithelial morphogenesis in Drosophila. *Development, 142*(10), 1777-1784. doi:10.1242/dev.122002

Hutson, M. S., Tokutake, Y., Chang, M. S., Bloor, J. W., Venakides, S., Kiehart, D. P., & Edwards, G. S. (2003). Forces for morphogenesis investigated with laser microsurgery and quantitative modeling. *Science, 300*(5616), 145-149. Retrieved from <Go to ISI>://000181988900053

Hutson, M. S., Veldhuis, J., Ma, X., Lynch, H. E., Cranston, P. G., & Brodland, G. W. (2009). Combining Laser Microsurgery and Finite Element Modeling to Assess Cell-Level Epithelial Mechanics. *Biophysical Journal, 97*(12), 3075-3085. doi:10.1016/j.bpj.2009.09.034

Irvine, K. D., & Wieschaus, E. (1994). CELL INTERCALATION DURING DROSOPHILA GERMBAND EXTENSION AND ITS REGULATION BY PAIR-RULE SEGMENTATION GENES. *Development, 120*(4), 827-841. Retrieved from <Go to ISI>://WOS:A1994NF92000010

Jacinto, A., Woolner, S., & Martin, P. (2002). Dynamic analysis of dorsal closure in Drosophila: From genetics to cell biology. *Developmental Cell, 3*(1), 9-19. Retrieved from <Go to ISI>://000176769500005

Jaeger, J., & Monk, N. (2014). Bioattractors: dynamical systems theory and the evolution of regulatory processes. *J Physiol, 592*(Pt 11), 2267-2281. doi:10.1113/jphysiol.2014.272385

Jensen, S. (2015). An Introduction to Lagrange Multiplier. Retrieved from http://www.slimy.com/~steuard/teaching/tutorials/Lagrange.html

Kiehart, D. P., Galbraith, C. G., Edwards, K. A., Rickoll, W. L., & Montague, R. A. (2000). Multiple forces contribute to cell sheet morphogenesis for dorsal closure in *Drosophila*. *Journal of Cell Biology, 149*(2), 471-490. Retrieved from <Go to ISI>://000086598600021

Kline, J., Stein, Z., Susser, M., & Warburton, D. (1985). Fever during pregnancy and spontaneous abortion. *American Journal of Epidemiology, 121*(6), 832-842. Retrieved from http://www.ncbi.nlm.nih.gov/pubmed/4014176

Kofink, D., Boks, M. P., Timmers, H. T., & Kas, M. J. (2013). Epigenetic dynamics in psychiatric disorders: environmental programming of neurodevelopmental processes. *Neuroscience and Biobehavioral Reviews, 37*(5), 831-845. doi:10.1016/j.neubiorev.2013.03.020

Kumar, S., Maxwell, I. Z., Heisterkamp, A., Polte, T. R., Lele, T. P., Salanga, M., . . . Ingber, D. E. (2006). Viscoelastic Retraction of Single Living Stress Fibers and Its Impact on Cell Shape, Cytoskeletal Organization, and Extracellular Matrix Mechanics. *Biophysical Journal, 90*, 3762-3773.

Lamka, M. L., & Lipshitz, H. D. (1999). Role of the amnioserosa in germ band retraction of the Drosophila melanogaster embryo. *Developmental Biology, 214*(1), 102-112. doi:10.1006/dbio.1999.9409

Layton, A. T., Toyama, Y., Yang, G.-Q., Edwards, G. S., Kiehart, D. P., & Venakides, S. (2009). Drosophila morphogenesis: tissue force laws and the modeling of dorsal closure. *Hfsp Journal, 3*(6), 441-460. doi:10.2976/1.3266062

Lecuit, T., & Lenne, P. F. (2007). Cell surface mechanics and the control of cell shape, tissue patterns and morphogenesis. *Nature Reviews Molecular Cell Biology, 8*(8), 633-644. Retrieved from <Go to ISI>://000248302300013

Leptin, M. (1999). Gastrulation in Drosophila: the logic and the cellular mechanisms. *Embo j, 18*(12), 3187-3192. doi:10.1093/emboj/18.12.3187

Lynch, H. E., Crews, S. M., Rosenthal, B., Kim, E., Gish, R., Echiverri, K., & Hutson, M. S. (2013). Cellular mechanics of germ band retraction in Drosophila. *Dev Biol, 384*(2), 205-213. doi:10.1016/j.ydbio.2013.10.005

Lynch, H. E., Veldhuis, J., Brodland, G. W., & Hutson, M. S. (2014). Modeling cell elongation during germ band retraction: cell autonomy versus applied anisotropic stress. *New Journal of Physics, 16*. doi:10.1088/1367-2630/16/5/055003

Ma, X., Lynch, H. E., Scully, P. C., & Hutson, M. S. (2009). Probing embryonic tissue mechanics with laser hole-drilling. *Physical Biology, 6*, 036004.

Mao, Y., & Baum, B. (2015). Tug of war--the influence of opposing physical forces on epithelial cell morphology. *Dev Biol, 401*(1), 92-102. doi:10.1016/j.ydbio.2014.12.030

Marinari, E., Mehonic, A., Curran, S., Gale, J., Duke, T., & Baum, B. (2012). Live-cell delamination counterbalances epithelial growth to limit tissue overcrowding. *Nature, 484*(7395), 542-545. doi:10.1038/nature10984

Martin, A. C., Gelbart, M., Fernandez-Gonzalez, R., Kaschube, M., & Wieschaus, E. F. (2010). Integration of contractile forces during tissue invagination. *Journal of Cell Biology, 188*(5), 735-749.

Mashburn, D. N., Lynch, H. E., Ma, X., & Hutson, M. S. (2012). Enabling user-guided segmentation and tracking of surface-labeled cells in time-lapse image sets of living tissues. *Cytometry Part A, 81A*(5), 409-418. doi:10.1002/cyto.a.22034

Mathematica. (2015). (Version 10.1 ed.). Champaign, Illinois: Wolfram Research, Inc.

Mehes, E., & Vicsek, T. (2014). Collective motion of cells: from experiments to models. *Integr Biol (Camb), 6*(9), 831-854. doi:10.1039/c4ib00115j

Merks, R. M. H., & Glazier, J. A. (2005). A cell-centered approach to developmental biology. *Physica A: Statistical Mechanics and its Applications, 352*(1), 113-130. doi:10.1016/j.physa.2004.12.028

Milunsky, A., Ulcickas, M., Rothman, K. J., Willett, W., Jick, S. S., & Jick, H. (1992). Maternal heat exposure and neural tube defects. *JAMA, 268*(7), 882-885.

Moretti, M. E., Bar-Oz, B., Fried, S., & Koren, G. (2005). Maternal hyperthermia and the risk for neural tube defects. *Epidemiology, 16*(2), 216-219.

Muliyil, S., Krishnakumar, P., & Narasimha, M. (2011). Spatial, temporal and molecular hierarchies in the link between death, delamination and dorsal closure. *Development, 138*(14), 3043-3054. doi:10.1242/dev.060731

Muliyil, S., & Narasimha, M. (2014). Mitochondrial ROS regulates cytoskeletal and mitochondrial remodeling to tune cell and tissue dynamics in a model for wound healing. *Dev Cell, 28*(3), 239-252. doi:10.1016/j.devcel.2013.12.019

Munoz, J. J., Barrett, K., & Miodownik, M. (2007). A deformation gradient decomposition method for the analysis of the mechanics of morphogenesis. *Journal of Biomechanics, 40*(6), 1372-1380. doi:10.1016/j.jbiomech.2006.05.006

Munoz, J. J., Conte, V., & Miodownik, M. (2010). Stress-dependent morphogenesis: continuum mechanics and truss systems. *Biomech Model Mechanobiol, 9*(4), 451-467. doi:10.1007/s10237-009-0187-9

Oda, H., & Tsukita, S. (2001). Real-time imaging of cell-cell adherens junctions reveals that Drosophila mesoderm invagination begins with two phases of apical constriction of cells. *Journal of Cell Science, 114*(3), 493-501. Retrieved from <Go to ISI>://WOS:000167084400005

Odell, G. M., Oster, G., Alberch, P., & Burnside, B. (1981). THE MECHANICAL BASIS OF MORPHOGENESIS .1. EPITHELIAL FOLDING AND INVAGINATION. *Developmental Biology, 85*(2), 446-462. doi:10.1016/0012-1606(81)90276-1

Ornoy, A., & Ergaz, Z. (2010). Alcohol abuse in pregnant women: effects on the fetus and newborn, mode of action and maternal treatment. *Int J Environ Res Public Health, 7*(2), 364-379. doi:10.3390/ijerph7020364

Oskouian, B., & Saba, J. D. (2004). Death and taxis: what non-mammalian models tell us about sphingosine-1-phosphate. *Seminars in Cell and Developmental Biology, 15*(5), 529-540. doi:10.1016/j.semcdb.2004.05.009

Pai, Y. J., Abdullah, N. L., Mohd-Zin, S. W., Mohammed, R. S., Rolo, A., Greene, N. D., . . . Copp, A. J. (2012). Epithelial fusion during neural tube morphogenesis. *Birth Defects Res A Clin Mol Teratol, 94*(10), 817-823. doi:10.1002/bdra.23072

Pantoja, M., Fischer, K. A., Ieronimakis, N., Reyes, M., & Ruohola-Baker, H. (2013). Genetic elevation of sphingosine 1-phosphate suppresses dystrophic muscle phenotypes in Drosophila. *Development, 140*(1), 136-146. doi:10.1242/dev.087791

Peralta, X. G., Toyama, Y., Tokutake, Y., Hutson, M. S., Venakides, S., Kiehart, D. P., & Edwards, G. S. (2007). Upregulation of forces and morphogenic asymmetries in dorsal closure during *Drosophila* development. *Biophysical Journal, 92*, 2583-2596.

Peterson, N. S., & Mitchell, H. K. (1991). Environmentally Induced Developmental Defects in Drosophila. In L. Hightower & L. Nover (Eds.), *Heat Shock and Development* (pp. 29-43). New York: Springer-Verlag.

Polyakov, O., He, B., Swan, M., Shaevitz, J. W., Kaschube, M., & Wieschaus, E. (2014). Passive mechanical forces control cell-shape change during Drosophila ventral furrow formation. *Biophys J, 107*(4), 998-1010. doi:10.1016/j.bpj.2014.07.013

Pope, K. L., & Harris, T. J. (2008). Control of cell flattening and junctional remodeling during squamous epithelial morphogenesis in Drosophila. *Development, 135*(13), 2227-2238. doi:10.1242/dev.019802

Purcell, E. M. (1977). Life at low Reynolds number. *American Journal of Physics, 45*(1), 3. doi:10.1119/1.10903

Rauzi, M., Verant, P., Lecuit, T., & Lenne, P. F. (2008). Nature and anisotropy of cortical forces orienting Drosophila tissue morphogenesis. *Nat Cell Biol, 10*(12), 1401-1410. doi:10.1038/ncb1798

Ray, H. J., & Niswander, L. (2012). Mechanisms of tissue fusion during development. *Development, 139*(10), 1701-1711. doi:10.1242/dev.068338

Reed, B. H., Wilk, R., Schock, F., & Lipshitz, H. D. (2004). Integrin-dependent apposition of Drosophila extraembryonic membranes promotes morphogenesis and prevents anoikis. *Curr Biol, 14*(5), 372-380. doi:10.1016/j.cub.2004.02.029

Reinhart, B. J., Slack, F. J., Basson, M., Pasquinelli, A. E., Bettinger, J. C., Rougvie, A. E., . . . Ruvkun, G. (2000). The 21-nucleotide let-7 RNA regulates developmental timing in Caenorhabditis elegans. *Nature, 403*(6772), 901-906. doi:10.1038/35002607

Roote, C. E., & Zusman, S. (1995). Functions for Ps Integrins in Tissue Adhesion, Migration, and Shape Changes During Early Embryonic-Development in Drosophila. *Developmental Biology, 169*(1), 322-336. Retrieved from <Go to ISI>://A1995QY79400027

Rosenblatt, J., Raff, M. C., & Cramer, L. P. (2001). An epithelial cell destined for apoptosis signals its neighbors to extrude it by an actin- and myosin-dependent mechanism. *Current Biology, 11*(23), 1847-1857.

Rusch, J., & Levine, M. (1996). Threshold responses to the dorsal regulatory gradient and the subdivision of primary tissue territories in the Drosophila embryo. *Current Opinion in Genetics and Development, 6*(4), 416-423.

Saias, L., Swoger, J., D'Angelo, A., Hayes, P., Colombelli, J., Sharpe, J., . . . Solon, J. (2015). Decrease in Cell Volume Generates Contractile Forces Driving Dorsal Closure. *Developmental Cell, 33*(5), 611-621. doi:10.1016/j.devcel.2015.03.016

Santamaria, P. (1979). Heat Shock Induced Phenocopies of Dominant Mutants of the Bithorax Complex in *Drosophila melanogaster*. *Molecular Genetics and Genomics, 172*, 161-163.

Schindelin, J., Arganda-Carreras, I., Frise, E., Kaynig, V., Longair, M., Pietzsch, T., . . . Cardona, A. (2012). Fiji: an open-source platform for biological-image analysis. *Nat Methods, 9*(7), 676-682. doi:10.1038/nmeth.2019

Schöck, F., & Perrimon, N. (2002). Cellular processes associated with germ band retraction in Drosophila. *Developmental Biology, 248*(1), 29-39. Retrieved from <Go to ISI>://000177259200003

Slattum, G., McGee, K. M., & Rosenblatt, J. (2009). P115 RhoGEF and microtubules decide the direction apoptotic cells extrude from an epithelium. *Journal of Cell Biology, 186*(5), 693-702. doi:10.1083/jcb.200903079

Sokolow, A., Toyama, Y., Kiehart, D. P., & Edwards, G. S. (2012). Cell Ingression and Apical Shape Oscillations during Dorsal Closure in Drosophila. *Biophysical Journal, 102*(5), 969-979. doi:10.1016/j.bpj.2012.01.027

Solon, J., Kaya-Copur, A., Colombelli, J., & Brunner, D. (2009). Pulsed forces timed by a ratchet-like mechanism drive directed tissue movement during dorsal closure. *Cell, 137*(7), 1331-1342. doi:10.1016/j.cell.2009.03.050

Sorrosal, G., Perez, L., Herranz, H., & Milan, M. (2010). Scarface, a secreted serine protease-like protein, regulates polarized localization of laminin A at the basement membrane of the Drosophila embryo. *EMBO Rep, 11*(5), 373-379. doi:10.1038/embor.2010.43

Spahn, P., & Reuter, R. (2013). A vertex model of Drosophila ventral furrow formation. *PLoS One, 8*(9), e75051. doi:10.1371/journal.pone.0075051

Steinberg, M. S. (1963). Reconstruction of tissues by dissociated cells. Some morphogenetic tissue movements and the sorting out of embryonic cells may have a common explanation. *Science, 141*(3579), 401-408.

Steller, H. (2008). Regulation of apoptosis in Drosophila. *Cell Death and Differentiation, 15*(7), 1132-1138. doi:10.1038/cdd.2008.50

Sullivan, W., Ashburner, M., & Hawley, R. S. (2000). *Drosophila protocols*: Cold Spring Harbor Laboratory Press.

Supatto, W., Debarre, D., Moulia, B., Brouzes, E., Martin, J. L., Farge, E., & Beaurepaire, E. (2005). In vivo modulation of morphogenetic movements in Drosophila embryos with femtosecond laser pulses. *Proc Natl Acad Sci U S A, 102*(4), 1047-1052. doi:10.1073/pnas.0405316102

Taber, L. A., Lin, I. E., & Clark, E. B. (1995). MECHANICS OF CARDIAC LOOPING. *Developmental Dynamics, 203*(1), 42-50. Retrieved from <Go to ISI>://WOS:A1995QY56900004

Tomer, R., Khairy, K., Amat, F., & Keller, P. J. (2012). Quantitative high-speed imaging of entire developing embryos with simultaneous multiview light-sheet microscopy. *Nat Methods, 9*(7), 755-763. doi:10.1038/nmeth.2062

Toyama, Y., Peralta, X. G., Wells, A. R., Kiehart, D. P., & Edwards, G. S. (2008). Apoptotic Force and Tissue Dynamics During *Drosophila* Embryogenesis. *Science, 321*(5896), 1683-1686.

Truong, T. V., Supatto, W., Koos, D. S., Choi, J. M., & Fraser, S. E. (2011). Deep and fast live imaging with two-photon scanned light-sheet microscopy. *Nat Methods, 8*(9), 757-760. doi:10.1038/nmeth.1652

van den Eijnde, S. M., Boshart, L., Baehrecke, E. H., De Zeeuw, C. I., Reutelingsperger, C. P., & Vermeij-Keers, C. (1998). Cell surface exposure of phosphatidylserine during apoptosis is phylogenetically conserved. *Apoptosis, 3*(1), 9-16.

VanHook, A., & Letsou, A. (2008). Head involution in Drosophila: genetic and morphogenetic connections to dorsal closure. *Developmental Dynamics, 237*(1), 28-38. doi:10.1002/dvdy.21405

Vroomans, R. M., Hogeweg, P., & ten Tusscher, K. H. (2015). Segment-specific adhesion as a driver of convergent extension. *PLoS Comput Biol, 11*(2), e1004092. doi:10.1371/journal.pcbi.1004092

Wells, A. R., Zou, R. S., Tulu, U. S., Sokolow, A. C., Crawford, J. M., Edwards, G. S., & Kiehart, D. P. (2014). Complete canthi removal reveals that forces from the amnioserosa alone are sufficient to drive dorsal closure in Drosophila. *Molecular Biology of the Cell, 25*(22), 3552-3568. doi:10.1091/mbc.E14-07-1190

Weisstein, Eric W. "Polygon Area." From MathWorld--A Wolfram Web Resource. Retrieved from http://mathworld.wolfram.com/PolygonArea.html.

Welte, M. A., Duncan, I., & Lindquist, S. (1995). The basis for a heat-induced developmental defect: defining crucial lesions. *Genes & Development, 9*, 2240-2250.

White, K., Grether, M. E., Abrams, J. M., Young, L., Farrell, K., & Steller, H. (1994). Genetic control of programmed cell death in Drosophila. *Science, 264*(5159), 677-683.

Wodarz, A., Hinz, U., Engelbert, M., & Knust, E. (1995). Expression of crumbs confers apical character on plasma membrane domains of ectodermal epithelia of Drosophila. *Cell, 82*(1), 67-76. Retrieved from http://www.ncbi.nlm.nih.gov/pubmed/7606787

Wyczalkowski, M. A., Chen, Z., Filas, B. A., Varner, V. D., & Taber, L. A. (2012). Computational models for mechanics of morphogenesis. *Birth Defects Res C Embryo Today, 96*(2), 132-152. doi:10.1002/bdrc.21013

Yan, Y., Jiang, L., Aufderheide, K. J., Wright, G. A., Terekhov, A., Costa, L., . . . Janetopoulos, C. (2014). A Microfluidic- Enabled Mechanical Microcompressor for the Immobilization of Live Single- and Multi- Cellular Specimens. *Microscopy and Microanalysis, 20*(1), 141-151. doi:10.1017/s1431927613014037

Zajac, M., Jones, G. L., & Glazier, J. A. (2000). Model of convergent extension in animal morphogenesis. *Physical Review Letters, 85*(9), 2022-2025. doi:10.1103/PhysRevLett.85.2022

Zienkiewicz, O. C., & Taylor, R. L. (2005). The finite element method for solid and structural mechanics: Butterworth-heinemann.